Humanising robot fingers

Design, prototyping, and validation of an anthropomorphic robot finger with humanoid joint-ligament systems, tendon configurations and supporting ligaments

Jacob van Ooijen

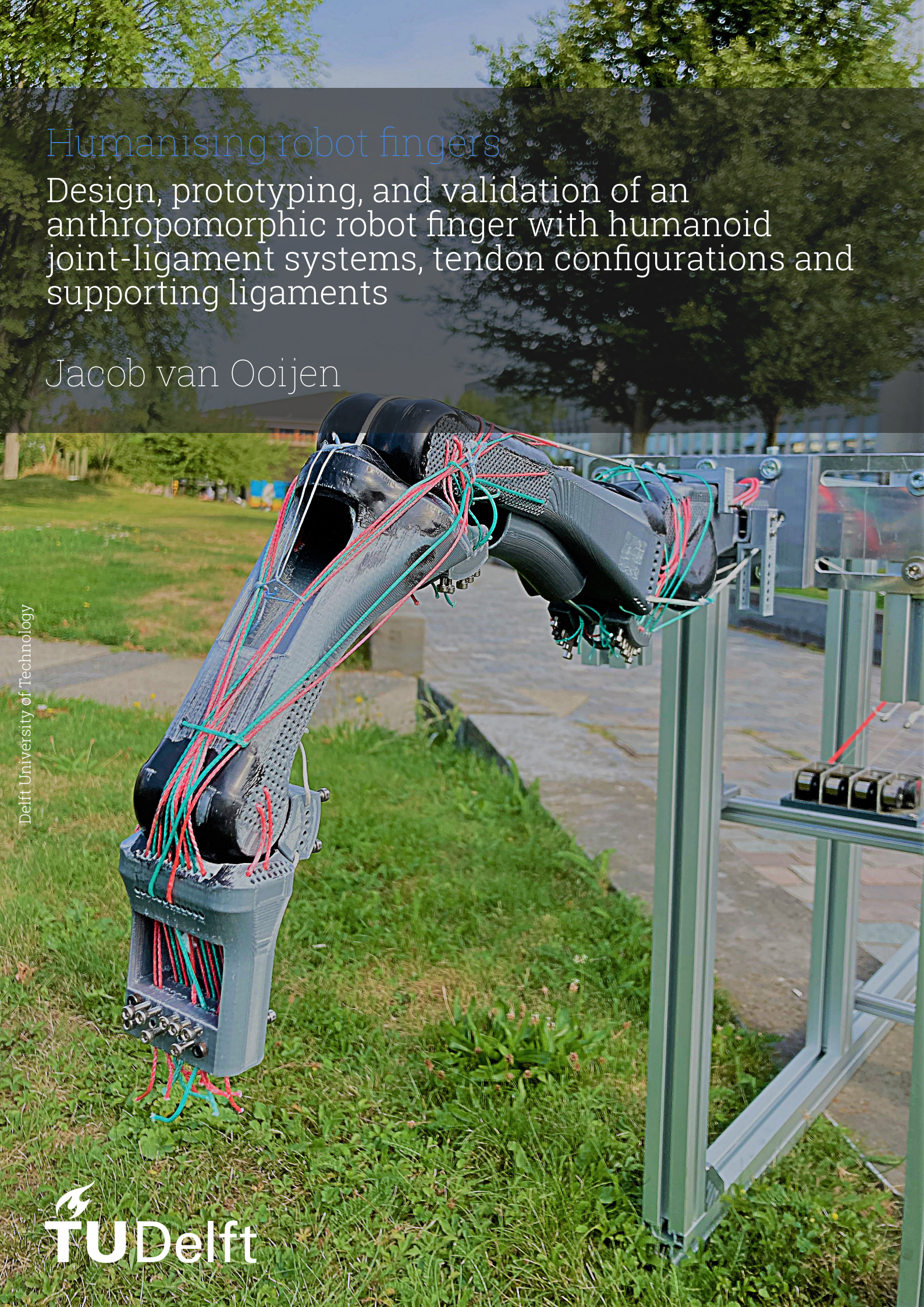

Delft University of Technology

TU Delft

Humanising robot fingers

Design, prototyping, and validation of an anthropomorphic robot finger with humanoid joint-ligament systems, tendon configurations and supporting ligaments

by

Jacob van Ooijen

Student Number: 4229614

to obtain the degree of Master of Science

in Biomedical Engineering

at the Delft University of Technology

Supervisors: Dr. ir. G. Smit (TU Delft)
Dr. J.N.A.L. Leijnse (TU Delft)

Faculty of Mechanical, Maritime, and Materials Engineering, Delft

TU Delft

Preface

Throughout my life, I have been interested in both engineering and mechanics. Tinkering with machines and devices was a daily practice. As a child, one of my greatest gifts was a toolbox with a hammer and some wrenches, of which the hammer still remains in use. Later when growing up and being active in sports, the human body and physiology became a great interest to me as to how we can functionally move our bodies and later grew even further interested in the development of prosthesis.
As a muay thai practinioner, speed skater, and recreational musician, the mechanics of the muscles and tendons in the human body remain a fascinating topic as to how this machine which is our body is able to perform incredibly powerful movements, while at the same time perform delicate motions like playing an instrument. This fascination was the main reason for me to accept this thesis subject when it was proposed to me.
I would like to firstly thank my daily supervisor dr. Joris Leijnse, an interdisciplinary anatomist and hand biomechanics specialist, initiator of this project. I most acknowledge his time and effort to transfer his knowledge of not only the biomechanics of the finger needed for the completion of this project, but the human body in general. His thorough guidance throughout this project, his eye for detail in my designs, and in the writing of this thesis, have helped enormously in the achievements made in this project and in my development as a future engineer. Without his extensive knowledge, experience, and prior research, the realisation of the end product would not have been possible.
Secondly, I want to thank my supervisor dr. ir. Gerwin Smit, for the opportunity to conduct research in in the field of biomechanics. Even while initially, he did not have the time to supervise me during the height of the COVID Pandemic, he still accepted me as his tutor. His encouraging words and founded criticism during the project, as well as in the writing of this thesis, helped me to stay critical about my work, but also to other research. Working on a big project such as this can sometimes be lonely, but his bi-weekly meetings together with his other tutors, greatly aided me in finding new perspectives from other students, as well as feeling that I was not alone in the struggles that come with a Master thesis project.
I also want to thank ing. Jan van Frankenhuyzen for the usage of the robotics lab and making the 3D printers and other tools in this lab available to me. He introduced me to the vast possibilities of 3D printing, as well as the usage of water-soluble support materials in 3D printing, described in Table 4.2.
Special gratitude goes to dr. ir. Dick Plettenburg. As coordinator of the minor Biomedical Engineering at the time, he was able to allow me into the course at the last minute, even though the admission was already closed. Without this action, I would not have been able to witness the field of biomedical engineering, and I might not have entered the field.
Finally, I want to thank my family and my girlfriend for the continuous support, not only during this project, but for the past years of my studies. They gave me the confidence and distraction when I needed it the most. Their listening ears to my work helped me process the different technical challenges during this project, even when they did not completely understand what I was saying. In particularly, I want to thank my mother, dr. Rachel Kurian, for proofreading this work, as well as for her time and effort in actively motivating me in writing this thesis.

Jacob van Ooijen
Delft, October 2022

Summary

Background: Current challenges in the design of anthropomorphic robot fingers is the implementing of anatomically accurate tendon-ligament structures, specifically for the collateral ligaments, volar plates, and the extensor apparatus. The development of robot fingers with these structures could aid in the further understanding of the functional anatomy and biomechanics of the human finger. It has been suggested that these fibrous structures can be emulated as a set of individual, non-elastic strings. The configuration of these tendon-ligament structures result in the specific motions of the finger.
Aims: The aims of this thesis were to develop and manufacture an anthropomorphic finger prototype with fully anthropomorphic tendon-ligament systems. So the prototype could be functionally actuated as a human finger, and would perform humanoid motion mechanisms, such as the Interphalangeal joint coupling, an ab-adduction/axial rotation coupling.
Methods: A parametric finger model was derived from CT images of human finger bones, with a focus on the soft tissue connection the joints and the tendon pulley system attached to the phalanges. The finger segments were designed as a shell structures with functionally anthropomorphic shapes. The finger contained the metacarpal bone, the proximal, middle and distal phalanx and included humanoid joints, tendons, and ligaments. These finger bone shells had fine rosters of perforations for the attachment of joint ligaments and supporting ligaments, implemented as a collection of individually attached dyneema strings, allowing for the precise and iterative attachment of these strings. The strings had adjustment possibilities to accurately determine their functional lengths. This model was then produces by FDM additive manufacturing on a scale of 5:1 with PLA as a material. To reduce the friction around the joints, friction experiments were performed, where graphite in an epoxy resin was found to be an appropriate coating for the joint surfaces. The tendons and ligaments systems were developed as a collection of non-elastic Dyneema strings, where the string lengths and positioning were identified according to biomechanical finger models.
Results: The result was the creation of a finger prototype with anthropomorphically realistic pulley systems for the tendons with joint surfaces of minimal friction, so that the finger could be actuated by the tendons to simulate realistic humanoid behaviour. The humanoid motion, and coupling mechanisms were verified with 2D motion tracking software and manual measurements by performing possible movements done by actuating the muscle tendons of the finger prototype and by comparing the resulting motion with that of a human finger. Where the finger prototype performed similar motions as a human finger.
Conclusions: This research project successfully developed an anthropomorphic finger with humanoid joint-ligament systems connecting the finger segments, and tendon configurations. It showed the possibility of constructing these systems and configurations as a set of individual strings that could emulate the structures found in the human body. The resulting anthropomorphic finger can form a basis for further research in the complex mechanics, relation, and dependencies of the human hand and in doing so, aid in the study of a wide range of pathologies in the finger and the hand, as well as support surgeons in reconstructive surgery and rehabilitation.

Contents

Nomenclature

Abbreviations

Abbreviation	Definition
AA	Abduction-Adduction
AR	Axial Rotation
AA/AR	Abduction-Adduction/Axial Rotation
BEP	Bachelor End Project
CAD	Computer Aided Design
CL	Collateral Ligamanets
CLL	Concentric Layer Lines
CT	Computational Tomography
DA	Dorsal Aponeurosis
DIP	Distal Interphalangeal
DIPJ	Distal Interphalangeal joint
DOF	Degrees of Freedom
DP	Distal Phalanx
EA	Extensor apparatus
ED	Extensor Digitorum
FDP	Flexor Digitorum Profundus
FDS	Flexor Digitorum Superficialis
fps	Frames per second
IO	Interosseus/Interossei
IP	Interphalangeal
IPJ	Interphalangeal joint
LU	Lumbrical
MC	Metacarpal
MCP	Metacarpophalangeal
MCPJ	Metacarpophalangeal joint
MP	Middle Phalanx
ORL	Oblique Retinacular Ligament
PIP	Proximal Interphalangeal
PIPJ	Proximal Interphalangeal joint
PP	Proximal phalanx
RIO	Radial Interosseus
TL	Triangular Ligament
TRL	Transverse Retinacular Ligament
TUD	Technical University Delft
UIO	Ulnar Interosseus
WS2	Tungsten disulphide

1 Introduction

1.1. Background

The hand is one of the most functional limbs of the human body, used in a wide variety of daily tasks, ranging from high load carrying activities such as rock climbing and boxing to delicate movements such as writing or playing an instrument. There have been significant advances in the 21st century in developing an anthropomorphic robotic hand that undertake the complex functions of the human hand.[17] Currently, the human hand is still unsurpassed in functional versatility as compared to robot hands. Most humanoid robot fingers use mechanical pins or bearings for the smooth and stable motion of the joints.[4] In contrast, human finger joints have cartilaginous surfaces lubricated by synovial fluid contained in a joint capsule and are mechanically stabilised by joint ligaments. Such joints not only have very low friction, but the ligaments also allow for limited elastic-passive deformations under load that enhance grasp efficiency. Robot fingers, which did have ligamentous finger joint connections, relied on elastic materials to ensure joint stability and had comparatively higher friction in the joints[32] Furthermore, the tendon configurations in robot fingers were generally not entirely anthropomorphic. This held particularly for the extensor apparatus of the interphalangeal joints. This complex apparatus anatomically consists of the confluence of the end-tendon fibres of four muscles: the extensor, the radial and ulnar interossei and the lumbrical. In humanoid robot fingers, this apparatus is generally simplified or replaced by non-anatomical structures.
This thesis project describes the process of the development of an anthropomorphic finger with anthropomorphically realistic joints, ligaments, and tendon configurations.
The applications would be (i) to improve understanding of the functional morphology of the finger's load bearing soft tissues, (ii) to create a demonstration model for simulation, study, and teaching of finger biomechanics for engineers, and clinicians such as hand surgeons and hand therapists, and (iii) to produce a functionally comprehensive truly anthropomorphic robot finger model that could possibly be the basis of a new generation of prosthesis and robotic hands.

1.2. Anatomy and biomechanics of the human finger

1.2.1. Skeletal structure, joints, and ligaments

The skeletal structure of the hand consists of the carpals (wrist bones), metacarpals (MC) (mid-hand bones), and the phalanges (finger bones).[34] The fingers have three phalanges: the proximal, middle and distal phalanges (PP, MP, DP, respectively). The thumb, which is not further considered in this thesis, has only two phalanges.
The joint chain of the human finger consists of the MC, PP, MP, and DP, which create three joints: the metacarpophalangeal joint, the Proximal Interphalangeal (PIP) joint, and the Distal Interphalangeal (DIP) joint.
The PIP and DIP joints are highly congruent bicondylar joints, of which the surfaces approximate revolute shapes. The bicondylar shape provides lateral and some axial-rotational stability, even without ligaments. These joints can therefore be seen as anatomical hinge joints with one degree of freedom (DOF): flexion-extension.

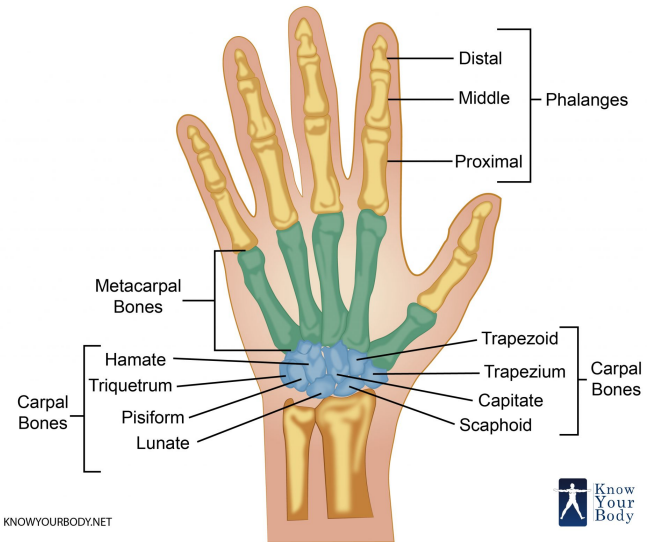

Figure 1.1: Schematic of the bones of the hand.[1] *Retrieved from* `https://www.knowyourbody.net/hand-bones.html`

The MCP joint is more complex, being partly a ball and socket joint and partly a bicondylar joint. The distal joint surface of the MC head contacts the PP joint surface by a single contact area as a ball and socket joint with 3 DOF: Flexion-extension, abduction/adduction (AA), and rotation of the PP around its longitudinal axis called axial rotation (AR). The palmar surface of the MC head is flat, and has a prominent horse-shoe shaped rim that forms a bicondylar joint surface. When the MCP joint is fully flexed, the PP contacts the palmar MC joint surface at the respective legs of the horse-shoe at two collateral contact points, as a bicondylar joint.[38] This provides lateral joint stability when the MCP joint is flexed. The horse-shoe shape of the palmar MC joint surface allows for a smooth surface transition from the ball-shaped distal surface of the MC head in extension to its bicondylar palmar face in the flexion end-position. At full flexion, the MCP joint motions while maintaining the collateral contact points are only flexion-extension and axial PP rotation, meaning that the MCP joint has 2 DOF in full flexion[1].
The finger joints are synovial joints, which have the following properties.

- The joints are covered by cartilage
- The joint space is filled with synovial fluid, which nourishes and lubricates the cartilage
- The synovial fluid is prevented from leaking from the joint by the synovial membrane, which envelops the joint.

The cartilage surfaces lubricated by synovial fluid have extremely low friction.[19] This ensures a smooth motion in the joints, and enables the functioning of the joints without significant wear in healthy humans.

1.2.2. Finger joint ligaments and constraining structures

The finger joints obtain mechanical robustness by ligaments, positioned superficial to the synovial membrane. Functionally, there are two distinct ligament sets in the finger joints:
Collateral ligaments(CL): These ligaments allow the full range of motion of the joints while providing lateral stability to the joints.[13] The CL (or proper collateral ligaments) are anatomically situated symmetrically at both lateral sides of the joint, hence the name 'collateral'. The CL consist of grossly parallel arrangements of loosely interconnected collagen fibres aligned along the directions of the out-of-plane forces. The collateral ligaments originate dorsal to the flexion axis of rotation on the proximal head of the joint, and insert volarly on the socket of the joint, crossing diagonally the axis of rotation. To allow the kinematics of the joints over the full joint range, the ligament fibres have precise

[1]Correspondence with Joris Leijnse on the anatomical structures in the human hand and finger

lengths and attachment points at the bones they interconnect. Because of their loose interconnectivity, the CL can be emulated as a set of independent strings.
Volar plates: Volar plates are complex, partly fibro-cartilaginous ligaments at the palmar side of the finger joints. They have multiple purposes. Especially at the interphalangeal (IP) joints, they function as 'stopper ligaments' that become taut at joint hyperextension to prevent further joint extension. They are also thick external menisci that increase joint congruence and increase the flexor tendon moment arms at the joints. The volar plates attach to the palmar bone surfaces, but are also suspended from broad expansions of the collateral ligaments, called the accessory collateral ligaments.
Oblique retinacular ligament The Oblique retinacular ligament (ORL), or Landsmeer's ligament, is suggested to function as a restraining, and thus stabilising force for the flexed distal phalanx when the DIPJ is flexed while the PIPJ is forced into extension.[5] Classically, it is described to originate volar at the lateral face of the PP, runs towards the volar aspect of the PIPJ, after which it travels dorsally to insert into the terminal tendon at the conjuction of the lateral bands on the MP.[21]
In the MCP joint, the arrangement of the fibres of the proper collateral ligaments, accessory collateral ligaments, and the form of the volar plate, not only allow for full range of the flexion-extension motion of the joint, but also cause a coupling between abduction, and axial rotation.[38].

1.2.3. Muscles and tendons of the human finger

The human finger itself contains no muscles and is entirely controlled by tendons of muscles that are positioned proximal to the MCP joint. There are six or even seven muscles per finger, but they form only five independent end tendons. According to their anatomical position, the muscles are differentiated into extrinsic muscles (positioned in the forearm) and intrinsic (positioned in the hand between the wrist and the MCP joint) muscles.
The extrinsic muscles are the Extensor Digitorum (ED), the Flexor Digitorum Superficialis (FDS) and the Flexor Digitorum Profundus (FDP). The ED arises from the lateral epicondyle of the humerus at the elbow and is the only extensor of the MCP joint. The FDS arises from the medial epicondyle of the elbow and the FDP arises from the proximal palmar surface of the ulna and the membrana interossea, between the ulna and radius.
The intrinsic muscles are the radial and ulnar interosseus (RIO and UIO respectively)[2], and the lumbrical muscle (LU). The interossei arise palmar and lateral at the metacarpals and insert with two end-tendons of variable relative size. One tendon inserts into the base of the PP. The other tendon fans out broadly over the dorsum of the PP. These flat, broad tendons of the RIO and UIO are called 'wings' of the extensor apparatus (EA). The LU is unusual in that it does not originate from bone. The LU originates at the level of the mid-hand from the tendons of the FDP, and its tendon joins the wing tendon of the RIO. At the level of the MCP joint, all muscles run with independent tendons. The flexors maintain independent tendons within the fingers. The FDS inserts at the palmar side in the middle phalanx. The FDP inserts at the palmar side into the distal phalanx.

Between the MCP joint and the PIP joint, the tendon of the ED, and the tendons of the UIO, RIO and LU, fan into fibres that interweave over the dorsum of the PP into a complex fibrous sheet, called the Extensor Apparatus or Extensor Assembly (EA)[3]. At the level of the PIP joint, the central fibres of this sheet, called the Medial Band, insert into the middle phalanx as the PIP joint extensor tendon. The lateral fibres, called the lateral bands, arise from the medial band, pass the PIP joint collaterally, fuse over the dorsum of the MP and insert into the DP as the extensor tendon of the DIP joint. The direct connection between the medial band, inserting into the MP, and the lateral bands, inserting into the DP, results in the coupling of motion of the PIP and DIP joints. Meaning that the proximal excursion of the extensor tendon results in extension of both the PIP and DIP joints.[20, 27, 23] The fibres of the lateral bands have precise origins of the ED and lengths to enable the smooth and continuous motion of these joints.[27]
The primary movers of the fingers, being irredundant in finger control, are the ED, FDS, FDP, RIO and UIO. The ED is the only extensor at the MCP joint. The FDS and FDP flex the PIP and DIP joint, respectively. The RIO and UIO are the only ab-adductors of the MCP joint. The LU tendon follows basically the same track as the RIO and therefore the LU does not fix an independent DOF, but is

[2]Anatomically, the interossei are classified into dorsal and palmar interossei
[3]In older anatomic literature, EA is also called the Dorsal Aponeurosis. In hand surgery literature, the proximal part of the EA is also called the Extensor Hood

redundant with the radial interosseous.[23] In basic control the finger can function without LU: The LU provides a secondary control level that may improve finger control at the level of the interphalangeal joints in, e.g., fast motions[23, 24]. Being redundant in primary finger control, the LU is not further considered in the present finger model.

1.2.4. Supporting ligaments of the flexors and extensors

The flexor tendons run over the palmar aspect of the finger through a set of tightly fitting ring-shaped fibrous tunnels called flexor pulleys. They function as a guide to keep the flexor tendons close to the phalanges, and prevent bowstringing of the flexor tendons. There are a total of 8 flexor pulleys (5 annular, 3 cruciate): The annular pulleys A1-A5, overlay respectively, the volar plate of the MCP joint, the proximal aspect of the PP, the volar plate of the PIP joint, the mid-portion of the MP, and the volar plate of the DIP joint. Because the A1, A3, and A5 pulleys are fixed to the volar plates of their respective joints, the orientation of pulleys change in relation to the joint angles. The cruciate pulleys C1-C3 are situated respectively between the A2 and A3 pulley, the A3 and A4 pulley, and between the A4 and A5 pulley. For this project, the cruciate pulleys were not incorporated into the finger design.
The ED has three main supporting ligaments, constraining the position of the central tendon, and the lateral bands. Because the metacarpal head is spherical, the ED would dislocate from the midline of the MCP joint in a flexed position in the absence of a supporting structure. The sagittal bands, a thin, broad sheet of connective tissue on the dorsum of the MCP joint, help to maintain the EDC tendons over the midline of the joint. These bands are dynamic structures that move with the extensor tendons during MCP joint motion.[7] The sagittal bands arise from the volar plate, and extend dorsally to transversely envelop the MCP joints. The sagittal bands also aid in preventing bowstringing of the extensor tendon.[6]
The transverse retinacular ligament's (TRL) primary function is to limit the dorsal movement of the lateral bands.[31] With that, they prevent bowstringing of the lateral bands at the extended PIP joint.[28] They arise from the volar plate of the PIP joint, and attach to the lateral bands across the lateral face of the head op the PP.
The triangular ligament (TL) is a thin layer of transverse fibres between the lateral bands across the dorsum of the MP. [40] It limits the lateral bands from separating during finger flexion at the terminal tendon.

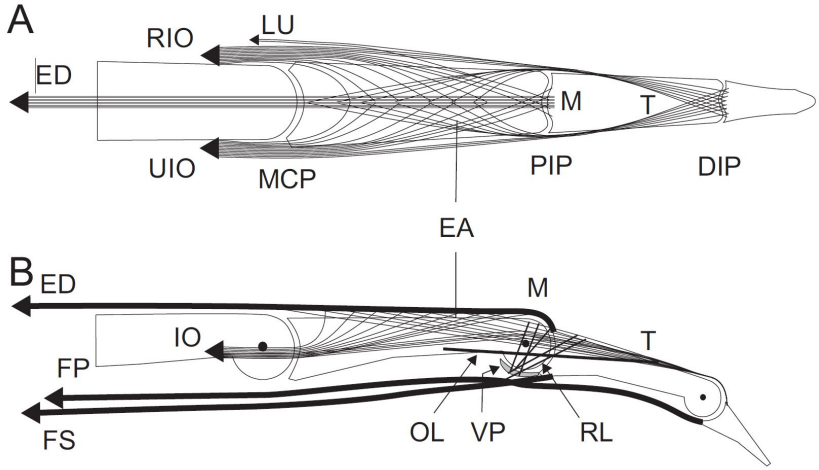

Figure 1.2: Schematic of the human finger with the extensor apparatus (EA), Interossei (IO), and the deep and superficial flexors (FDP, FDS).[28] A: Dorsal view. ED: Extensor Digitorum. M: Medial ED tendon, inserting into the middle phalanx. T: Lateral fibres of the ED, recombining at the middle phalanx and inserting into the distal phalanx. RIO and UIO: Radial and Ulnar Interosseus tendons which joint M and T. LU: Lumbrical tendon. MCP, PIP and DIP: Metacarpophalangeal joint, and respectively the Proximal and Distal Interphalangeal joints. B: Lateral view. OL: Oblique retinacular ligament, originating laterally and palmarly from the PP and inserting into T at the MP. VP: Volar plate, attaching firmly to the MP. RL: (Transverse) Retinacular ligament, originating from the volar plate and inserting into the lateral bands T. *Used with permission from Joris Leijnse*

1.2.5. Control analysis of human finger kinematics

The kinematics of this finger model was based on the finger control analysis in by Leijnse.[25] Summarized, to control a joint chain with N rotational Degrees of Freedom, N+1 independent muscles/tendons are minimally required. The explanation is that the lengths of N independent muscle/tendons can fix the N DOF of the chain when these tendons are taut, while at least one extra muscle/tendon is needed as a generalised antagonist to keep these N muscle/tendons taut. A schematic of a bi-acrticular chain with 2 DOF and 3 muscles is shown in Figure 1.3. The finger chain has 5 rotational DOF in the joints: the MCP joint, being a ball joint, has 3 DOF, while the two interphalangeal joints, being bicondylar, are hinge joints with 1 DOF each. However, the finger has only 5 independent muscles: one extensor, two flexors (superficial and deep flexor), and a radial and an ulnar interosseus. Since the control of 5 rotational DOFs in a joint chain requires 6 independent muscles, the finger lacks one muscle for full control. This control deficit is resolved by two passive tendon/ligament mechanisms. Each of these mechanisms couples two rotational DoFs into a 1 DoF joint control mechanism. (i) The IPJ coupling mechanism couples the rotations of the interphalangeal joints by the double insertion of the extensor tendon throug the medial band and the lateral bands, in the sense that flexion/extension of the DIPJ causes coordinated flexion of the PIPJ. (ii) The AA/AR mechanism couples in the MCPJ the rotations of abduction/adduction with axial rotation, i.e., rotation of the proximal phalanx around its longitudinal axis, through the constraining mechanisms of the MCP collateral ligaments.

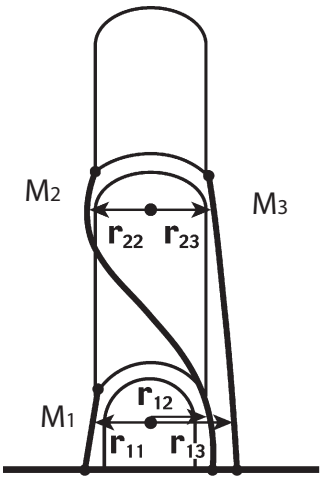

Figure 1.3: Planar bi-articular chain controlled by N + 1 muscles (N+ #DOF). [25] The two muscles M_2 and M_3, originating on the right side of the chain, control the top joint. The left muscle M_1 is required to retain the lower joint in its position when M_2 and/or M_3 are active. Functionally, M_1 is the antagonist of the combined forces of muscles M_2 and M_3.*Used with permission from Joris Leijnse.*

1.3. Review of anthropomorphic robotic hands and fingers

This section draws upon on a more detailed literature study on robotic hands and fingers, which can be found in Appendix B. Over the past decade, several anthropomorphic robot fingers have been developed with tendon-driven actuation. The connection of the segments was often realised with the use of pins and bearings, in contrast to ligament structures found in the human body such as the collateral ligaments. In these fingers, the relatively high friction over sliding surfaces as well as stability of the joint were a challenge that pins and bearings could solve. Particularly in 3D printed parts, since heat treated coatings are precarious with the materials commonly used in 3D printing. However, a number of researchers have been able to develop finger joints with bone connecting structures mimicking human ligaments. Xu and Todorov [47] used crocheted ligament strings made of a non-elastic material, complemented by a rubber sleeve. Tian et al[44], Faudzi et al[14] and Tasi et al[43] used silicon rubber bands at the approximate origins and insertions of the collateral ligaments. Folgherhaiter[16] used elastic bands to hold the joints together. Even though the methods used in these robot fingers have resulted in human-like joint connection, the majority of the ligaments were made of highly elastic materials such as rubber or silicone in contrast to the tough, fibrous ligament structures found in the human body. Due to

their elastic characteristics, these ligament structures could cause instability of the joints when subject to external forces outside the planes of rotation of the tendons.

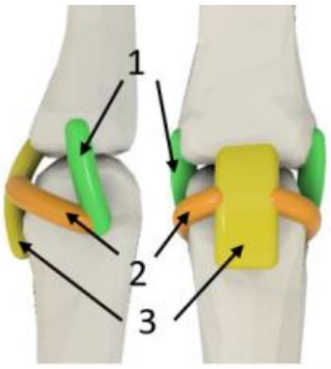

Figure 1.4: Ligament system of the finger designed by Tasi et al.[43] 1: Proper collateral ligaments connecting the phalanges directly. 2: Accessory collateral ligaments constraining the motion of the volar plate. 3: Volar plate limiting the extension of the phalanges

The implementation of the dorsal aponeurosis (DA) in robot fingers has been performed in previous robot fingers as a way to couple the PIP-DIP extension as well as to allow abduction of the MCP joint. This was either done by using strands of highly inelastic string such as Dyneema[14, 45, 11] or by using a laser-cut rubber sheet.[47, 43, 18]. Though the coupling of the extension of the PIP and DIP joints was found in state-of-the-art robot fingers, the means to do so were not equivalent to the real anatomy. The fibres of the DA were often simplified as single strands of tendon instead of a continuous fibrous sheet, or it was made from a single laser cut piece of isotropic material. Furthermore, the resulting IPJ coupling was not precisely documented, as well as the abduction-adduction range of motion.

Figure 1.5: Dorsal view of the extensor mechanism designed by Xu and Todorov (2016). [47]

While the anthropomorphic fingers discussed above were able to perform humanoid motion and poses, they lack anatomically accurate tendon-ligament structures, specifically for the collateral ligaments, volar plates, and the extensor apparatus. Parts of the finger's functional morphology are not yet fully understood, most specifically, the mechanisms coupling the IPJ rotations and the AA/AR coupling in the MCP joint. In order to further develop anthropomorphic fingers which can better mimic the human body, the ligament structures connecting the finger joints and the EA needed to be emulated as a combination of individual strands of fibres. The research regarding configuration of these fibres is detailed in the next section.

Table 1.1: List of existing anthropomorphic robot hands and the relevant characteristics of the fingers

Author, year	Joint Connection	Extensor configuration
Xu and Todorov, 2016	Crocheted ligaments with silicone rubber	Laser-cut rubber sheet
Tian et al. 2019	Silicone rubber ligaments	Extensor tendons at MCP, PIP and DIP joints
Folgheraiter & Gini, 2000	Elastic bands	Extensor tendons at MCP, PIP and DIP
Faudzi et al, 2017	Silicone rubber ligaments	Interconnected Dyneema strands
Tasi et al, 2019	Silicone rubber ligaments	Laser-cut rubber sheet
He et al, 2020	Connecting pins	Laser-cut rubber sheet
Deshpande et al, 2011	Connecting pins	Interconnected Spectra strands
Wilkinson et al, 2003	Connecting pins	Interconnected nylon strands.

1.4. Preexisting research framework of the present project

The present project is the next step in a series of projects at the hand research lab of Joris Leijnse, colleagues and students at current and previous institutes aimed at researching the biomechanics of the functional morphology of the tendon mechanisms and their supporting ligaments that control the kinematics of the human finger, such as the IPJ coupling and the AA/AR coupling, as well as the ligament systems of the joints. To understand the position of the present thesis in this fundamental research in the fingers' functional morphology, the previous results must be reviewed in some detail.

IPJ coupling mechanism research

A mathematical model of the IPJ coupling[28] was developed based on measurements in a large amount of fingers.[27] In this model, the extensor apparatus (EA) was modelled as a composite of multiple strings strings (representing the lateral bands) unconstrained aligned at the shortest paths between their origin on the central slip of the extensor tendon, and their insertion into the DP (see Figure 1.6). Summarised, in this model, each individual string would be taut at a specific PIP/DIP joint angle, and be slack at other angles, where the load transfers to the adjacent strings along the joint's range of motion. The model allowed approximating the variations in the real measured human IPJ coupled trajectories with a maximum error of about 1%. The model showed that the points where the strings originated from the central slip, as well as the lengths of these strings, needed to be accurately determined to obtain the specific IPJ coupled trajectory variations.

The mathematical model was then implemented into a physical planar 3D finger model in the thesis of Callewaert.[26] This mechanical model demonstrated realistic humanoid IPJ trajectories with a multi-string EA. To investigate the dynamical behaviour, this prototype was motorised in the thesis of Van Erum.[22] This project demonstrated the robust and low-friction functioning of the multi-string EA model as a mechanism for IPJ coupling. This was improved in the TUD Bachelor End Project by Van Bemmel et. al[39] by implementing anthropomorphic dorsal surfaces of the PP and MP, obtained from CT scans. This project aimed at creating a low friction mechanical model of the finger with anthropomorphic dorsal surfaces for further studies in robotic finger control. Both prototypes were designed as two parallel finger models in one. One side served to implement the multi-string model of the EA, the other implemented the other tendons (flexor tendons and interosseus tendon).

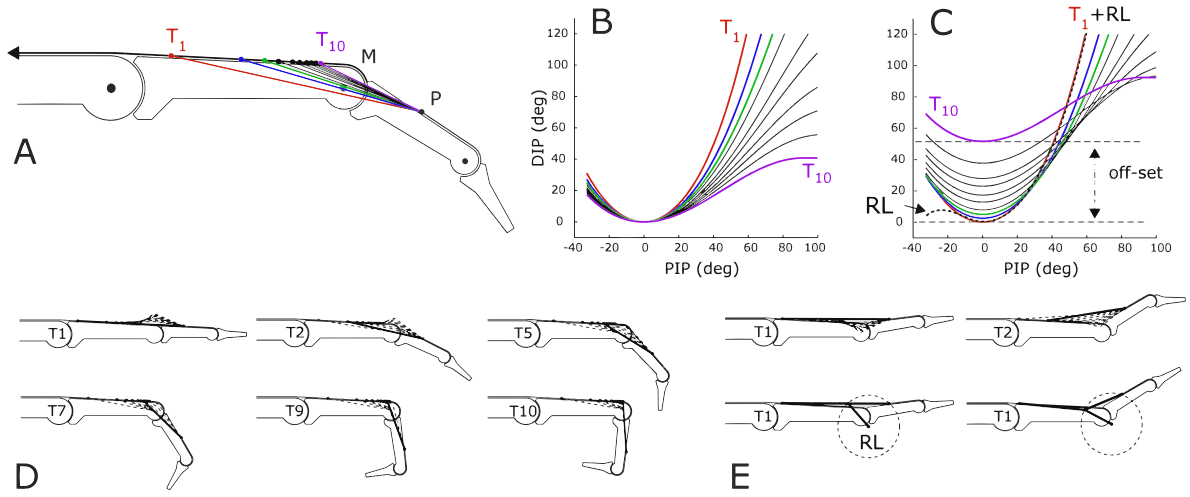

Figure 1.6: 2D morphological model of the mechanism coupling the PIP and DIP joint angles in the human finger developed by Leijnse and Spoor[28]. *A*: The model consists of an insertion of the extensor tendon (M) into the middle phalanx, and a number of strings (T_i) originating from this tendon at distinct points, which are model parameters. These strings merge at point P into a single extensor tendon of the DIP joint. *B*: The IPJ coupling of each individual string T_i. *C*: Adding specific extra lengths to the T_i strings off-sets their PIP-DIP coupled trajectory. A superposition of T_i strings with precisely determined lengths allows for each string T_i determining only a part of the coupled PIP-DIP trajectory at the moment that this strings is taut, and being slack in the remainder of the trajectory. *D*: Finger motion with the PIP-DIP as created by the strings in A and C. T_1, T_2...T_10: strings (in bold lines) that determine the PIP-DIP coupling in the drawn position, while all other strings (in dotted lines) are slack. *E*: With the PIPJ hyperextension, the Retinacular ligament (RL) functions to limit the bowstringing of the T strings. *Figures reproduced with permission from Leijnse and Spoor[28].*

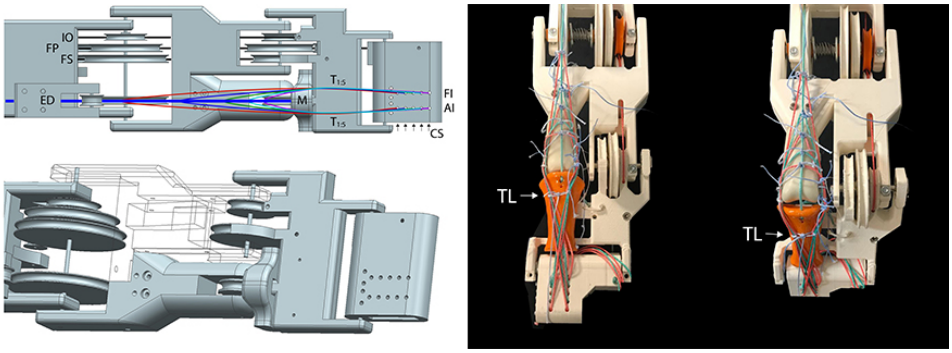

Figure 1.7: Planar mechanical finger prototypes with proximal phalanx, middle phalanx, and distal phalanx on fixed axes. *Left*: Finger developed in the thesis project of Callewaert[26] with parametric PP and MP. *Right*: The reiteration of the mechanical finger developed in the TUD BEP of Schuurman et. al[39] with anthropomorphic dorsal surfaces for the PP and MP. The extensor digitorum (ED) lies separate from the flexor tendons (FS, FP) and the interosseus tendon. The strings of the lateral bands ($T_1 : 5$) originate from the ED over the dorsum of the PP, travel lateral across the PIP joint, run dorsally over the MP, and insert into the fixation points (FI and AI) at the DP. The lengths of the T-strings were adjusted with compression screws (CS). Over the dorsum of the MP, the collateral palmar shift of the T-strings at PIPJ flexion needed to be limited with a triangular ligament (TL).

AA/AR coupling in the MCP joint

Leijnse's theoretical models of the AA/AR coupling in the MCP joint have not yet been published, but have been implemented in a physical model developed in the TUD Bachelor End Project of Vis, van der Luyt and Sorgedrager.[42] A spherical MCP joint was modelled with individual strings representing collateral ligaments, a volar plate with flexor pulley, flexor and extensor tendons, and an antagonistic pair of interossei. The collateral ligaments were implemented with three strings with precise attachment points to the bone segments and precise lengths. The extensor tendon could be stabilised with one pair of strings representing the sagittal bands. The model had no joint surface coating and had therefore significant friction, but nevertheless functioned sufficiently well to verify that AA/AR coupling occurred by the collateral ligaments according to the theoretical models. However, the degree of axial rotation with abduction in this spherical joint was greater than in the human finger. Therefore, further investigation

in the AA/AR coupling was necessary, taking into account the specific anthropomorphic bone and joint surface geometry. Also, for further research, the joint friction needed to be reduced.

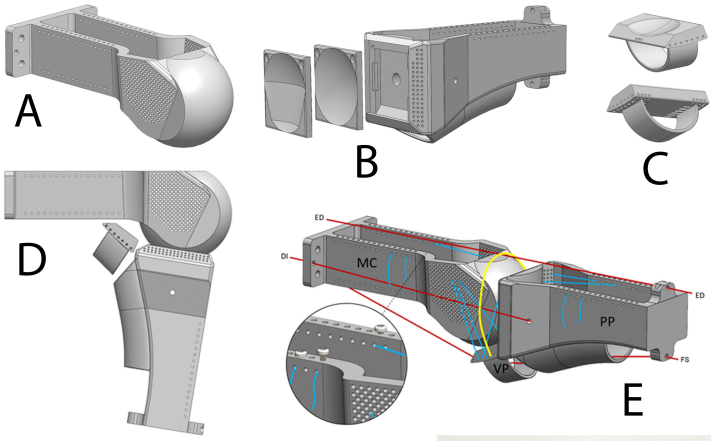

Figure 1.8: MCPJ model realised in the TUD BEP project of Vis, van der Luyt, and Sorgedrager[42]. *A-D*: CAD design of the hollow shelled metacarpal (A), proximal phalanx (B) with interchangable joint socket, volar plate (C), and the assembly of these componentens (D). *E*: Model of the ligament and tendon configuration. *Blue*: collateral ligaments attached to the Metacarpal, proximal phalanx, and volar plate. *Red*: The tendons used for actuating the joint. Dorsal and volar are the extensor and flexor tendon, lateral are the interosseus tendons. *Yellow*: Sagittal band stabilising the extensor tendon over the midline of the metacarpal head.

1.5. Problem statement

In the previous research, summarised above, the IPJ coupling mechanism and the MCP AA/AR coupling mechanism, were individually modelled in mechanical prototypes. However, a complete finger combining these mechanisms did not exist. The prototypes incorporating the IPJ coupling mechanism were designed as two parallel fingers with each finger having a different function. As such, the composition of the multi-string EA, together with the other tendons, needed to be implemented into a single set of finger segments. The MCP joint prototype had only a spherical head, while the palmar side of the MCPJ is a bicondylar joint, which increases the stability of the joint in full flexion. Furthermore, the joint had high amounts of friction, which would cause difficulty in actuating the joint, especially at higher loads.

1.6. Aims of the research project

In the previous research, summarised above, the IPJ coupling mechanism and the MCP AA/AR coupling mechanism, were individually modelled in mechanical prototypes. This master thesis project aims to combine all these design results into a complete manipulable anthropomorphic finger model. The finger prototype is to include the following:

- Anthropomorphic joint/ligament systems
- Flexion-extension of the Metacarpophalangeal, Proximal Interphalangeal and Distal Interphalangeal joints
- Abduction/adduction of the Metacarapophalangeal joint
- Joint action realised with anthropomorphic tendon structures
- Both the Interphalangeal joint and Ab-adduction/Axial rotation coupling mechanisms

2 Methods

2.1. Design requirements

To achieve the aims, the following design requirements were made.
Scale: The scale of the finger model needed to be high enough to aid in accurately locating the origins and insertion of the soft-tissue fibres, and to demonstrate the subtle mechanisms in the finger. In the previous BEP project by Vis, Sorgedrager and Vanderluyt[42], a scale of 5:1 resulted in a properly functioning joint. Without further research in size reduction of the joint, the scale of the new finger model was decided to 5:1 as well.
Tendon and ligament attachment: Because the exact locations of the origins and insertions of the tendons and ligaments were unknown, a wide area of possible locations on the finger bones needed to be researched. This required that the individual strings could be attached to the bones over a wide area, allowing for the precise and step-wise attachment of these strings. With this, the exact length of each string needed to be adjustable.
Weight: The weight of the finger components have a direct impact on the forces acting on them. Heavier components mean higher forces on the tendons during actuation. This leads to higher stresses on the components, higher normal forces on the joint surfaces with resulting higher friction, and a heavier frame in which the finger needed to be mounted. Given this, the components had to be lightweight while still strong enough to withstand the forces acting on the finger model during normal use.
Parametric design: Finger bones have subtle and complex geometry, with variations in external contours[8] and anatomy of the tendon-ligament systems[10]. To negate the effects of these variations, the finger components were parametrically designed.
Friction: High friction in the joints can cause malfunctioning of the finger due to high tendon tension, stress on the finger components, and rough motion. Thus, methods needed to be explored to minimise the friction in the joint areas using the materials available at TU Delft.

2.2. Development process

The development process of the anthropomorphic finger involved replicating the functional aspects of the geometry of the middle finger, finding a low-friction treatment of the joint surfaces. This was followed by the configuration of the load-bearing soft tissues of the human finger using string constructions.
Acquiring anthropomorphic finger bone geometries
The finger bone geometries were firstly acquired by dissection of a finger, and Computational Tomography (CT) images. This would not only provide accurate geometric properties of the bones and their structures, but also provide a 3D image to aid in the design in a computational aided design (CAD) system.
Design of the finger model in a CAD system
From the CT images, the geometric characteristics in the finger bones which are imperative for the finger dynamics were identified and implemented in a parametric finger model.
In the CAD design, the supporting frames for ligament string attachment and their length adjustments were implemented, as well as designing the components to be lightweight and robust. Furthermore, the

finger components were designed such to reduce the amount of material needed for manufacturing, while maintaining structural integrity.

Manufacturing the finger components

The parts were produced by additive manufacturing/3D printing because of the complex shapes in the design of the finger. The printing methods and materials were considered, as well as the printing parameters and printing orientation. The 3D printing was optimized for accurate and smooth surface shapes, together with low printing time and low weight.

Research low-friction treatments for the joint surfaces

The head and socket of the finger prototype were in direct contact with each other. This required low-friction joint surfaces. To minimize joint friction, different coatings and surface treatments were tested for their friction characteristics in a standardized joint setup. After comparison of the results, the superior surface treatment was applied to the finger components where low friction was needed.

Integrating the finger components with anthropomorphic tendon-ligament systems into a functioning prototype

With the finger components manufactured and treated for lower friction, the finger prototype was assembled. For this, a frame was built that could support the finger and the actuators of the tendons. The tendons and ligaments discussed in Section 1.2 were emulated with strings made of Dyneema®.

2.3. Verification

With the finger prototype assembled and in working order, a motion analysis was performed to verify the finger with the design requirements, as well as to verify the AA/AR and IPJ coupling mechanisms of the finger.

The finger prototype was filmed while performing IPJ flexion-extension, as well as ab-adduction. These motions require active and coordinated contribution from all tendons, i.e., all actuators and tendons function properly. The IPJ coupling mechanism, as well as the paths of the joints, were measured using motion tracking software to verify the kinematics of the finger prototype with respect to the aims of this project.

The human finger demonstrates different movements in the event of dysfunctional muscles or tendons. To further verify its anthropomorphism, the finger prototype should demonstrate the same movements if such pathologies are introduced. An example is when the intrinsic muscles are weakened. This can be caused by ulnar nerve palsy due to trauma or illness.[30]. This pathology was emulated in the finger prototype to compare its movement with that of a human finger with this pathology.

2.4. Report structure

The outline of this thesis is as follows:

- Chapter 3: The following chapter discusses the design of the components of the finger prototype.
- Chapter 4: This chapter focuses on the choices made for 3D printing the finger components.
- Chapter 5: This chapter describes the setup, and data analysis of the experiments conducted to find a suitable low-friction treatment for the joint surfaces of the finger components.
- Chapter 6: In this chapter, the manufactured and surface treated finger components are assembled with the tendons and ligaments emulated as individual strings. In here, strategies are discussed to configure the orientations and lengths of the strings of these structures.
- Chapter 7: In this chapter, the motion of the assembled finger prototype is analysed to verify the design with the aims of this thesis project.
- Chapter 8: Finally, in the last chapter, the conclusions of this project are discussed. Furthermore, final remarks and recommendations for future works are outlined.

3

Developing anthropomorphic CAD designs of finger bones

3.1. Introduction

This chapter outlines the development of the CAD designs of the finger bones, and the volar plates. As the basis of the CAD design, a cadaver specimen was dissected, and 3D images were made using CT scans. These CT images were further manipulated in CAD software. From the CT images, the available literature, the anatomical information in Section 1.2, and the design requirements discussed in Section 2.1, a parametric model was made.

3.2. Methods

3.2.1. CT image acquisition

At the Department of Anatomy at Amsterdam Medical Centre (AMC), an anatomic finger specimen was obtained and dissected. The functional morphology of the finger was reviewed, after which the finger bones were separated and cleaned of soft tissue, except for the joint ligament attachments and flexor pulleys. At the AMC department of Radiology, individual CT scans of the bones were obtained by G. Streekstra, PhD. The scan parameters were tweaked to either maximize the bone surface contrast or to maximize the soft tissue contrast. The latter was needed to identify areas of attachment of pulleys and joint ligaments. The scan data was segmented into high resolution STL data format by I.G.G. Dobbe, PhD, using software developed at AMC allowing to include or exclude the soft tissue.
The CT images with and without soft tissue are shown in Figure 3.1 and Figure 3.2. In here, the individual finger bones are assembled together in extension.

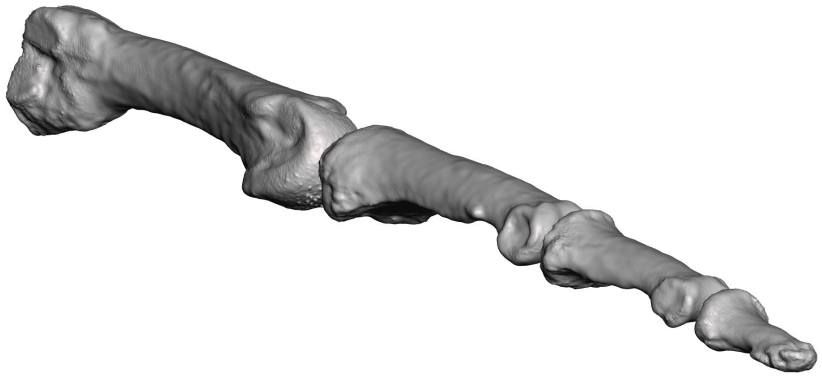

Figure 3.1: 3D image of the CT scanned finger without soft tissue.

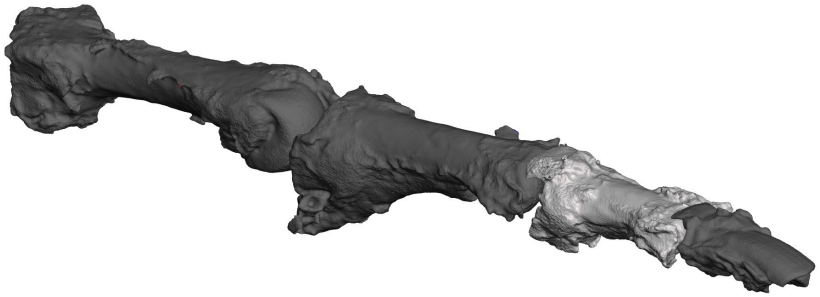

Figure 3.2: 3D image of the CT scanned finger with soft tissue

Manipulating these high resolution STL files in the CAD software SolidWorks (Dassault Systems SolidWorks Corp., Waltham, Massachusetts, USA) at the TU Delft required a high computational power due to the high density of the mesh. To reduce the computational capital, the mesh density of the bone shafts was reduces using the software Meshmixer (Autodesk, Inc., San Rafael, California). The details around the head and socket of the phalanges were the most important. So the mesh density around the shafts was reduced to 3000 triangles and the mesh density of the joint areas was reduced to 13000 triangles. This method reduced the mesh density with over 98 % while still maintaining a high enough level of detail in the joint areas. The resulting CT images could be viewed and sectioned properly in SolidWorks.
Figure 3.3 shows the scanned image of the Metacarpal bone, and the model with a reduced mesh without soft tissue. Figure 3.4 shows the Proximal Phalanx with a reduced mesh. In here, the PP is sectioned across the sagittal plane for the inspection of the A2 pulley.

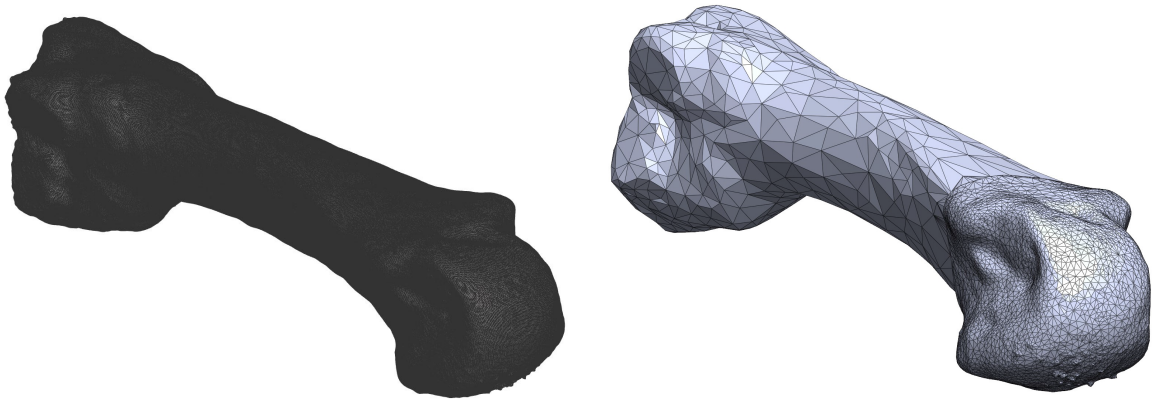

Figure 3.3: Metacarpal bone scanned using a CT scanner from Amsterdam Medical Center (AMC). *Left*: High detail mesh prior to mesh reduction. *Right*: Reduced mesh used for further developing the designed finger in SolidWorks

The CT files with reduced mesh could be imported into SolidWorks, where the dimensions, and functional geometry of the joint surfaces could be incorporated into the parametric CAD design of the finger prototype.

3.2.2. Developing a 3D CAD design

In SolidWorks, the 3D models from the CT images were sectioned to find the geometry of the joint surfaces. This was also done to find the difference between the surface with soft tissue and only bone. Because the designed finger was made of fully rigid materials, an integration between the hard and soft tissue needed to be found. This included the shape of the joint surfaces, origins, and insertions of the joint ligaments and the geometry of the finger pulleys.
To minimize the weight of the finger prototype, the phalanges were designed as a shell structure, being hollow on the inside. This is because most of the stresses from bending, occur on the outer edge of the part.

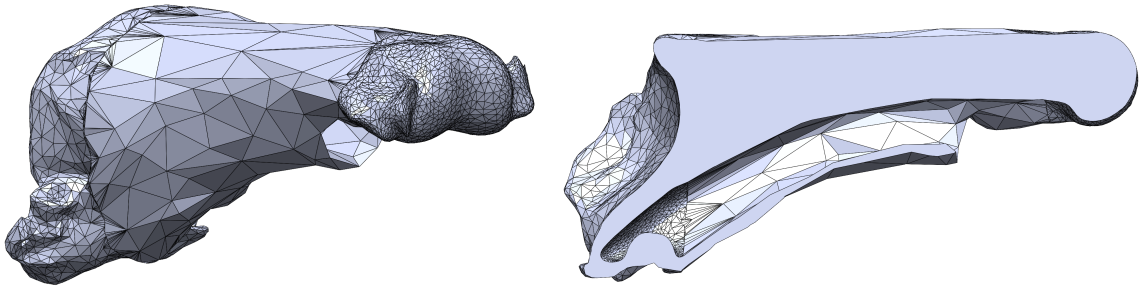

Figure 3.4: Image of the proximal phalanx with the head and socket having a greater mesh density than the shaft, including soft tissue.

In contrast, the least amount of stress is found on the inside. Thus, a shell structure can reduce the weight of the phalanges, while still being strong enough to withstand the forces acting on the finger.
To allow for the precise and step-wise attachment of the ligament strings, perforations were designed along the faces of the finger bones. Ligament strings could be inserted into the perforations and would end up in the hollow interior of the phalanges. The larger area permitted the incorporation of multiple strings for the collateral ligaments, as well as the checkrein ligaments and the accessory collateral ligaments. Because the exact location of the attachments of the ligaments was unknown, this also ensured that the origins and insertions of the strings could be adjusted. To fixate the strings onto the phalanges, guides with fixating screws were designed. These fixation points were incorporated in the different finger components.
The head and socket joint areas of the PIP, and DIP joints were designed to fit tightly, with a tolerance of 2%. This was to compensate for the thickening of the surface when a coating was applied.

Metacarpal design
The metacarpal was the base of the assembly and thus needed to be strong enough to withstand the forces acting on the robot finger, as well as the weight of the individual parts. The fixation to the base onto the frame was designed as a solid plate with appropriate holes to guide the tendons. Each tendon had a separate guide hole to prevent the tendons from rubbing over each other. The metacarpal head was developed by combining the two aspects of the metacarpal joint area: (i) a semi-spherical head with (ii) two palmar condyles which come in contact with the proximal phalanx at full flexion. The transverse curvature of the head was constant across the flexion-extension midline, but along the sagittal plane, the curvature was not constant, having a smaller radius at the distal end of the head, and increased radius at the palmar and dorsal aspect. These two aspects were designed separately and combined to match their location on the CT image of the metacarpal.
Along the lateral faces of the metacarpal head, insertion holes were put for the insertion of ligament fibres. The shaft was designed as a curved, U-shaped bar. The dorsum of the shaft was made open to access the fibres inserted from outside the metacarpal head. Proximal to the base of the metacarpal, fixation points were added for the adjustment of the length of the inserted ligament fibres. The 3D model of the metacarpal is shown in Figure 3.5.

Proximal phalanx design
The proximal socket of the PP had a spherical shape with a constant curvature in the transverse plane, but along the sagittal plate, the socket had a more slated, varying curvature. This corresponded with the CT images, as well as the study by Schultz and Storace (1987)[38]. Cut-outs were made lateral to the socket, which were congruent with the palmar condyles of the metacarpal head. This allowed for flexion and abduction of the MCP joint when the joint was extended slightly, and constrained the abduction of the PP in full flexion.
The shaft of the PP had a curvature similar to the human finger. This curvature was needed for the smooth guiding of the flexor tendons as a continuous spline. Along the palmar face of the shaft, the A2 pulley was implemented as a tunnel from the middle of the PP until the proximal base. The start and end point of the A2 pulley was identified such, that it would not interfere with the PIP volar plate in

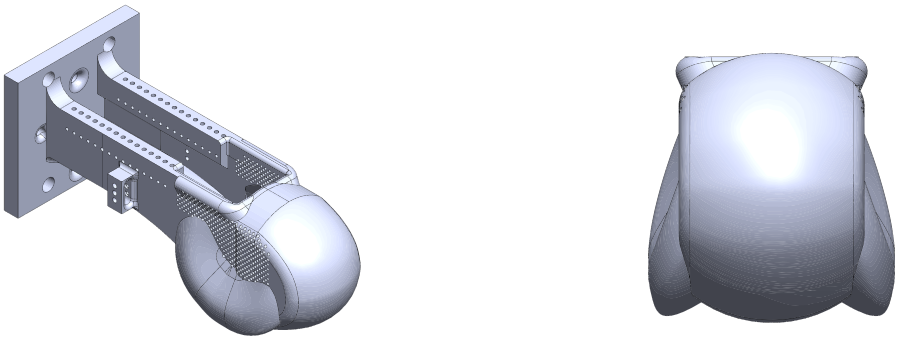

Figure 3.5: 3D model of the metacarpal. *Left*: isometric view. *Right*: Frontal view. The two palmar condyles protrude slightly below the spherical head. The dorsal area is open in order to feed the strings through the lateral insertion holes. On the shaft, screw holes are placed to fixate the strings such that the length can be adjusted. Guide holes at the are made for the tendons. On the lateral part of the base, a guide pulley for the interossei is added with adjustable height using screws.

flexion.
The distal head of the PP, at the PIP joint, had a bicondylar, revolute shape, which protruded volarly to the palmar aspect of the shaft.
Along the lateral faces of the proximal and distal joint area's, perforations were added for the insertion of ligament strings, as well as on the palmar aspect near the proximal joint surface for the attachment of the volar plate. Along the dorsum of the PP, two openings were made to access the inserted ligament strings. Internally, 4 rows of fixation points were incorporated for the ligament strings. Distal to the ligament insertions at the base of the PP, bigger perforations were added for the attachment of the interosseus tendons.

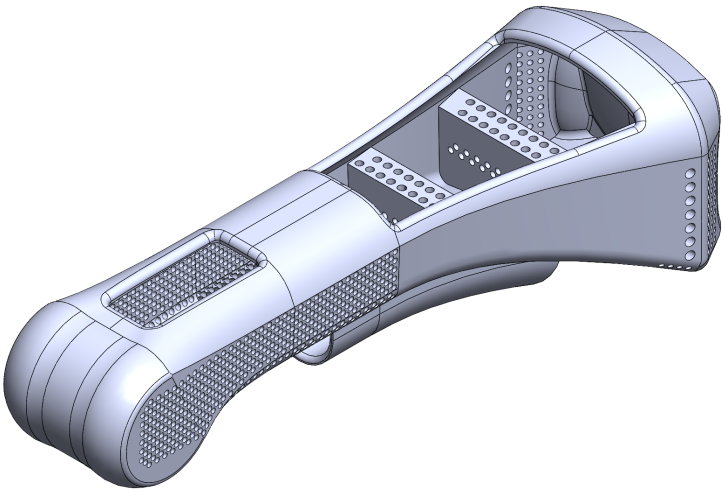

Figure 3.6: CAD design of the proximal phalanx

Middle Phalanx

The proximal socket of the MP was congruent with the distal head of the PP. As discussed in Section 1.2, this aided the PIP joint in lateral stability in conjunction with the collateral ligaments. Dorsally to the proximal socket, a notch was incorporated, which was also found in the CT scans. This notch aided in

collateral passing of the lateral bands along the lateral face of the PIP joint.
Similar to the PP, the shaft of the MP was curved to smoothly guide the FDP tendon. Along the palmar face, the A3 pulley was implemented, with its proximal and distal end chosen such that the flexor pulleys did not interfere with the motion of the volar plate during PIP or DIP joint flexion. The distal head of the MP, at the DIP joint, had a bicondylar, revolute shape, which protruded volarly to the palmar aspect of the shaft.
Perforations for the insertion of ligament strings were made along the lateral faces, the lateral palmar face, and at the proximal socket lateral to the joint surface. On the palmar face proximally, perforation were made for the attachment of the volar plate. Proximally on the dorsum, an opening was made for the access of the ligament strings, as well as on the palmar face distally. In the MP, no fixation points were incorporated. This was because the fixation on the MP could be done with a stopper knot, and the string length adjustment could be done with the fixation points on the adjacent phalanges.
Above the proximal socket, a perforation was made for the middle band of the Extensor Apparatus, while on the palmar aspect, a perforation was made for the FDS tendon.
Similar to the proximal phalanx, a matrix of perforations is implemented for the insertions of the ligaments. The proximal end has a notch. This notch pushes the fibres of the extensor apparatus laterally to slide of the lateral ends of the Proximal Interphalangeal joint. Along the lateral edge of the proximal joint socket, holes are added for the insertion of the collateral ligaments. As with the Proximal phalanx, ports are made for ease of access to the inside of the phalanx. An overview of the middle phalanx can be seen in Figure 3.7.

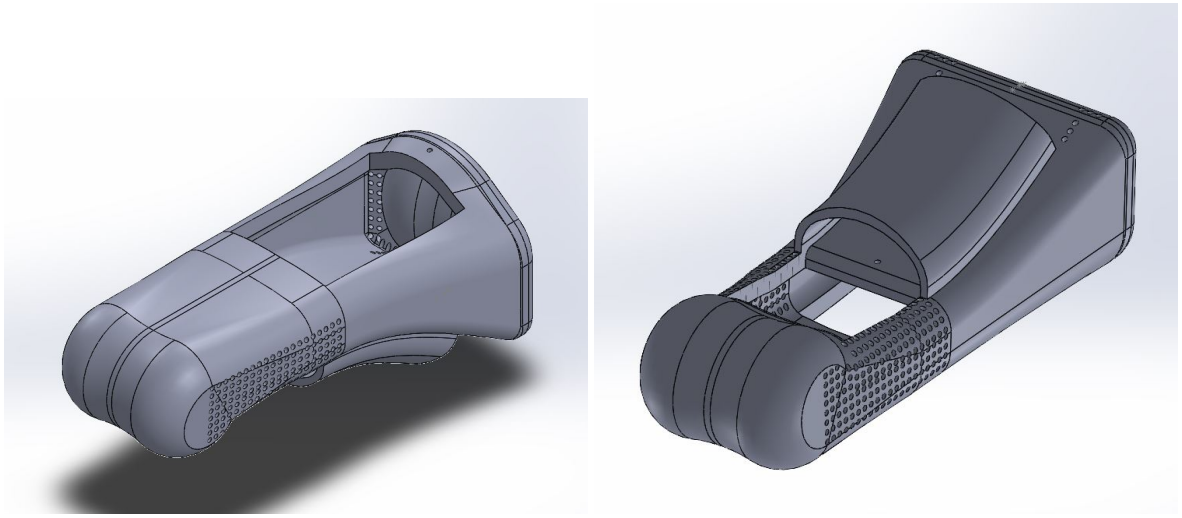

(a) Middle phalanx dorsal view **(b)** Middle phalanx palmar view

Figure 3.7: CAD model of the Middle phalanx

Distal Phalanx

The distal phalanx is the most distal part of the finger. As such, the DP has only a proximal joint socket, which is congruent with the distal bicondylar head of the MP. The shaft of the DP was designed as a cube with rounded edges. Curvature in this finger component was not necessary because no flexor tendons travel along the palmar and dorsal faces of the DP. In this model, the geometry of the fingertip was not regarded, because it is not necessary for the functional movement of the finger.
Lateral to the joint's socket, perforations were made for the ligament strings, as well as the ORL. Proximally on the dorsum, perforations were made for the insertion of the lateral bands of the EA. The dorsum was also made open for the access of the tendon-ligament strings with fixation points at the distal end of the DP. The model of the distal phalanx is seen in Figure 3.8.

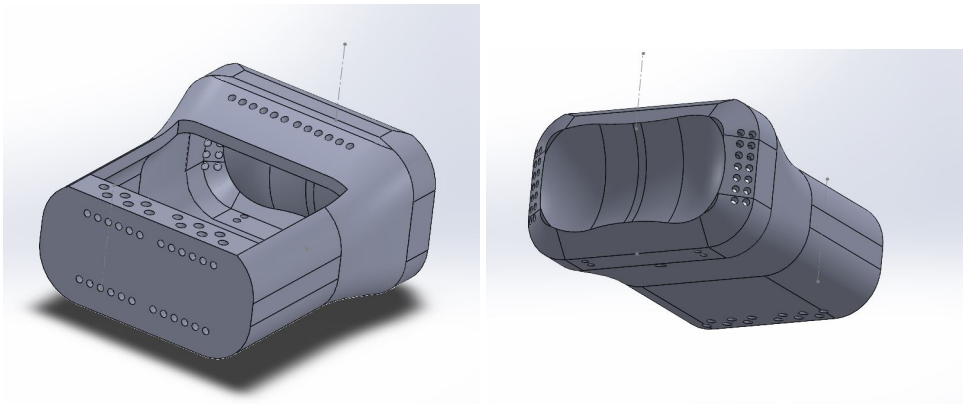

(a) Distal phalanx dorsal view **(b)** Distal phalanx palmar view

Figure 3.8: CAD model of the Distal phalanx

Volar plates design

The contact surface of the volar plates were designed to be congruent with the shape of the head of the joints. This meant that the volar plates of the PIP and DIP joints followed the bicondylar shape of the respective joints. The volar plate of the MCP joint, however, was made to be congruent with not only the spherical shape of the more dorsal head, but also with the bicondylar palmar head. The A1, A3 and A5 pulleys are incorporated in the volar plates, so the pulley moves along with the volar plate during flexion-extension. In the PIP and DIP volar plates, 12 insertion holes were incorporated for the attachment of the checkrein ligaments on the phalanges to prevent hyperextension, as well as for the accessory collateral ligaments. In the MCP volar plate, 16 insertion holes were incorporated for attachment to not only the metacarpal and proximal phalanx, but also the sagittal bands and fibres for the interosseus muscles. The lateral wall of the volar plates was risen to create more surface area for the fixation bolts to screw into. The volar plates are shown in Figure 3.9.

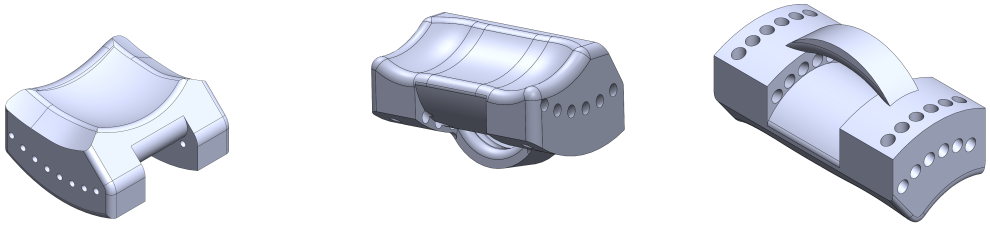

Figure 3.9: CAD model of the volar plates. Top left is the volar plate used at the MCP joint, top right volar plate is used at the PIP joint and the bottom one is used at the distal phalanx. The volar plates are shown in different orientations to show the different aspects of the parts

3.3. Results

The resulting components were assembled in SolidWorks. A lateral view of this assembly in flexion is shown in Figure 3.10. Along the contact points of the flexor pulleys, lines were drawn which showed the path of a tendon in tension. At the MCP joint, the distal socket at the PP matched correctly with the bicondylar shape of the palmar metacarpal head. The MCP joint could move freely into extension without interference of the PP.

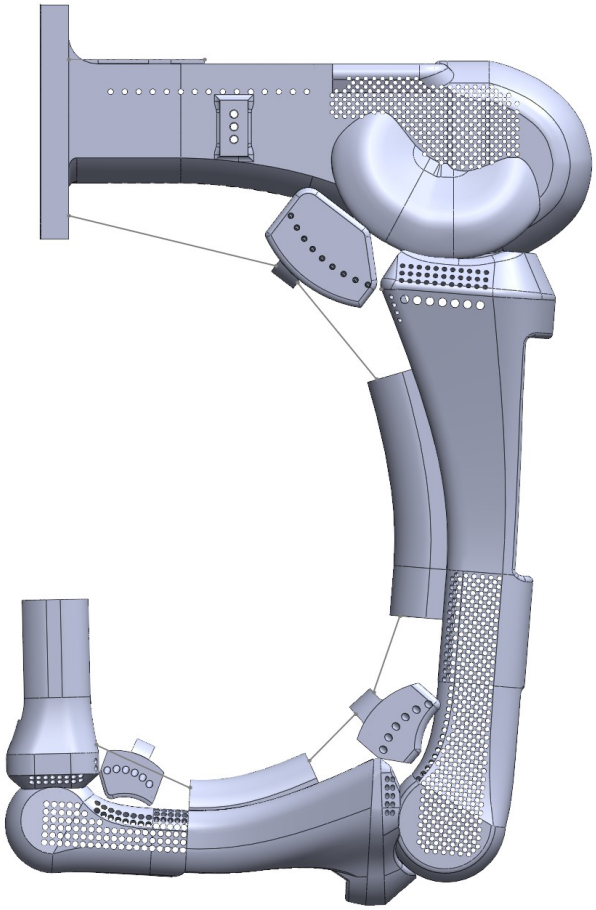

Figure 3.10: Assembly of the finger model in flexed position. Lateral view. The path of the flexor tendons through the pulleys is visible

3.4. Conclusion

The work described in this chapter resulted in a parametric model of the human finger bones, with soft and hard tissue integrated into individual finger bone segments. The resulting CAD models for the prototype were manufactured further, which is described in Chapter 4.

4

Optimizing the 3D printing of the CAD designs

4.1. Introduction

Because of the complex, multiplanar shapes and features of the finger model, the CAD model described in Chapter 3 was manufactured using Additive Manufacturing (AM)/ 3D printing. This chapter discussed the considered 3D printing methods and possible materials for each method. Following the choice of a printing method and material, the printing parameters were considered to optimize the manufacturing time, product accuracy, and strength.

4.2. Choosing the 3D Printing Method and material

Additive manufacturing (3D printing) consists of the physical realization of a 3D CAD design by the computer steered addition of sequential layers of material. Different 3D printing methods and many additive materials currently exist. To select an appropriate additive method to create the finger segments and other parts, three widely used additive methods and their materials were compared: stereolithography (SLA), selective laser sintering (SLS) and fused deposition melting (FDM). An overview of the compared characteristic of these printing methods is shown in Table 4.1.
SLA printing works by selectively hardening layers of UV-sensitive resin at the surface of a liquid resin solution to create a solid structure. The resin can be infused with additives, such as ceramic or metal powder, to create different mechanical properties. Such as high impact resistance or low friction. While the printing resolution of SLA is high, both the printing costs and printing durations are high as well compared to other methods. Furthermore, SLA printing requires support material on large overhanging structures. SLA printing is therefore less suitable as a rapid prototyping method.
SLS printing, a Power Bed Fusion technique, works by selectively sintering powdered particles on a printing bed by a laser, fusing the particles together to create a layer. In SLS printing, the powder particles function as support material. It is therefore a feasible option for printing large overhangs or shell structures. SLS printing also has a higher printing resolution than FDM printing. However, both costs and printing times are higher than other printing methods.
FDM printing is a rapid way of producing models in which a thermoplastic material is extruded by a fine nozzle from a large spool using heat and deposited in a layer-by-layer fashion. Both production costs and times are low. However, support structures are required for large overhangs and the resolution is lower than alternative printing methods.
In conclusion, for the finger segments, FDM printing was selected for its low cost and printing time. And a suitable solution was found for the support structures.

4.3. FDM printing materials

For FDM printing, different materials can be used, so a selection needed to be made. Considered were Acrylonitrile Butadiene Styrene (ABS) and Polylactic Acid (PLA). An overview of the general characteristics is shown in Table 4.2.

Table 4.1: Comparison of printing methods

Method	**Stereolithography (SLA)**	**Selective laser sintering (SLS)**	**Fused deposition melting (FDM)**
	Laser fusing surface layers in resin bath	Laser fusing powder surface layers	Nozzle extrudes heated thermoplastic material from spool
Printing time	Medium	Slow	Fast
Needs support structures	Yes	No	Yes
Resolution	High	High	Low
Cost	High	High	Low
Materials	Thermoset polymers (acrylic, ceramic suspension resin,	Powder particles (Polyamide, weldable metals/alloys, ceramics)	Thermoplastics (PLA, ABS, PETG)

Acrylonitrile Butadiene Styrene (ABS): ABS has a low cost and good mechanical properties, allowing to print though durable parts resistant to impact and wear (e.g., LEGO building blocks). Its high glass transition temperature allows withstanding relatively high temperatures before deforming, but printing requires a heated bed or chamber and releases odorous (toxic) fumes. ABS produces a surface finish with little oozing and stringing, but contracts when cooling, possibly resulting in dimensional inaccuracies or warping.
Polylactic Acid (PLA) is relatively strong and during the printing process, no toxic fumes are released as compared to ABS. PLA is however less resistant to UV light and not as tough as ABS. For an initial production with possible reiterations, PLA is a sufficient choice.

Table 4.2: Comparison of FDM printing materials

Material	**Polylactic Acid (PLA)**	**Acrylonitrile Butadiene Styrene (ABS)**
Strength	Medium	High
Surface resistance	Medium	High impact, wear resistance
UV resistance	No	Yes
Heat resistance	Medium	High
Printing bed temperature	Room temperature	Heated bed or chamber
Build plate adhesion, dimensional accuracy	Good	Dimensional inaccuracies: Warping, contracting
Printing finish	Medium	Less oozing and stringing
Toxicity of fumes	Non-toxic	Toxic
Cost	Low	Low

Support material Because of the need of a support material in FDM printing in order to create part with large overhangs or hollow parts, Polyvinyl alcohol (PVA) was used as support material. PVA is a water-soluble material used in the medical industry because of its biocompatibility and low toxicity. Often used for cartilage replacement or eye drops [2]. Furthermore, because PVA is water-soluble, the support material can be removed by submerging the parts in water and letting the PVA dissolve. By printing with PLA as main material and PVA as support material increases the flexibility of orientation to choose the layer direction best suited for the forces of the parts and smoothness. This also allows for FDM printers to make complex hollow parts.

4.3.1. FDM printers

In order to print with PLA as main material and PVA as support material, a dual-extrusion FDM printer is required. At TU Delft, Ultimaker (Ultimaker B.V., Utrecht, Netherlands) 3E and 5S dual extrusion FDM printers were available. At the time, no other alternatives were available.

4.4. Printing parameter selection

4.4.1. Printing plane orientation

Due to the layer-by-layer character of 3D printing, parts were not completely smooth after completion and ridges were visible. Printing in higher resolutions by reducing layer height could have reduced the surface roughness, but the discontinuous building would always result in some kind of surface roughness. And inaccuracies occur along the axis perpendicular to the printing bed. The segments were printed in the sagittal plane. The resulting longitudinal layers provided the greatest strength with respect to the segment compression loads. Moreover, at the proximal and distal interphalangeal joints, these print layers formed concentric layers lines in the head and socket. This reduced the roughness along the radius of the joint and prevented mechanical keying, which reduced friction even without coatings or polishing.

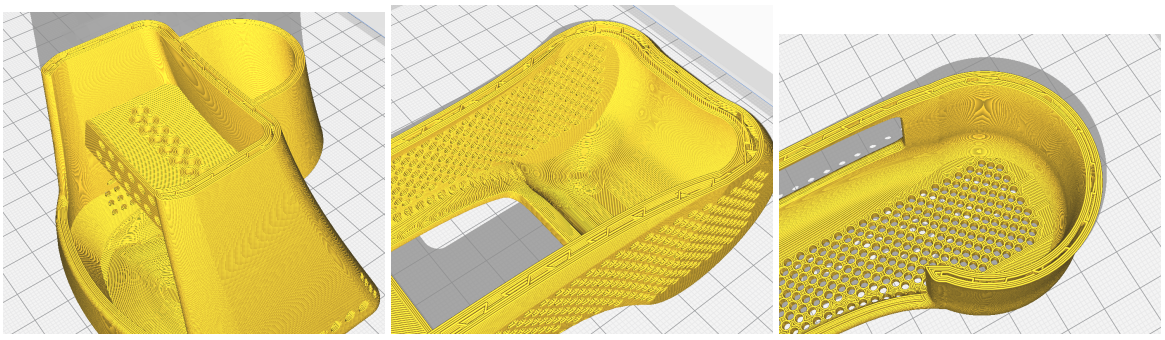

Figure 4.1: Layer orientation of the proximal phalanx at different printing orientation. From left: Frontal plane, proximal to distal. Middle: transverse plane, volar to dorsal. Right: sagittal plane, ulnar to radial.

4.4.2. Printing time

Due to time restrictions, and the relatively large scale of 5:1, it was critical to minimize the printing time without compromising functional printing quality. Default settings on the Ultimaker S5 for the printing of the proximal phalanx resulted in a printing time of 4 days. The following changes were made to reduce the printing time.

- *Layer height*: The layer height was set to 0.2 mm. A lower layer height increased the accuracy of the print along the vertical axis and reduced the size of the layer lines. However, this also increased the printing time because more layers needed to be printed. Because the bone segments were printed in the sagittal plane, the inaccuracy occurred in the transverse plane. This did not affect the accuracy of the geometry of the joint surfaces.
- *Infill density*: The segments had a shell structure, consisting of an inner and outer wall connected by infill material. Without noticeably compromising the structural integrity, the infill density could be reduced from 20% to 2% while the wall thickness was increased from 1 to 1.2 mm, without noticeably compromising the structural integrity. This reduced the printing time by 22 hours.
- *Number of printed top and bottom layers*: Contributing to printing time was the number of top and bottom layers. Reducing this number significantly reduced the printing time, but also strength and surface resolution. The shafts of the phalanges were therefore printed with 3 layers, while the joint surfaces had 6.
- *Printing speed*: Increasing the printing speed from 40 mm/s to 80 mm/s quickened the printing process, but reduced the accuracy of the geometry. At the shafts, a high accuracy was not necessary, in contrast to the joint surfaces which needed to be of acceptable smoothness. Therefore, at the joint surfaces, the printing speed was reduced from 80 to 60 mm/s, which still resulted in a relatively good finish.

An overview of the printing parameters is shown in Table 4.3

Table 4.3: 3D printing parameters

Layer height	Infill density	Wall thickness	Number of top and bottom layers	Printing speed
0.2mm	2%	1.2 mm	Shaft: 3 layers Joint surfaces: 6 layers	Shaft: 80 mm/s Joint surfaces: 60 mm/s

The resulting printing time for all the parts after adjusting the parameters was 2 days, and 3 hours: A time reduction of 47% compared to the default settings. Two resulting finger components can be seen in Figure 4.2.

Figure 4.2: Preliminary 3D printed DP and MP. The final components were metallic silver coloured.

5

Minimizing friction of joint contact surfaces: comparing surface treatment methods and coatings

5.1. Introduction

Friction in human joints is exceptionally low with friction coefficients as low as 0.001 up to pressure of more than 100 bar.[19] In a physical model allowing humanoid control, joint friction must be minimized, ideally to levels approaching humanoid friction. In this chapter, surface treatments were explored to reduce the friction around the joints. For this, an experimental setup was created for quantitative comparison of the friction of different surface treatments. This included the design of a standardized test joint and defining a standardized motion similar to a human joint with tendon actuation. The forces on the tendons were measured during motion and with the resulting forces, the required work and friction coefficients were calculated for each treatment

5.2. Methods

5.2.1. Design of the standardized test joint

To standardize the tests, a symmetrical convolute bicondylar joint was designed, actuated by a symmetric antagonistic tendon pair, further called extensor and flexor. The joint consisted of three parts: a shaft, a joint head and a socket segment. The shaft was printed with a baseplate that was bolted to the rigid support frame. This shaft had a U-shaped open profile, with at the inner surface set screws for fixation of the joint ligament strings. At this shaft, joint heads with different coatings could be fixed and interchanged for experiments. The joint head had a shell structure. At the cross-section of the shell and the geometric joint axis, holes were imprinted in the shell to guide the strings that, as joint ligaments, kept the joint head and socket together. These strings were inserted from the outside through these holes, and fixed at appropriate lengths by the set screws within the shaft. The socket segment of the joint was designed as a shell-like structure with holes laterally along the proximal edge. The ligament strings were inserted through these holes and fixed within the shell by knots of greater diameter than the hole. In the palmar and dorsal edge of the socket segments, holes were imprinted for fixation of the flexor and extensor tendons.

5.2.2. Tested materials

In the designed robot finger, wet and dry lubrication needed to be considered. Wet lubrication of the open joints would likely compromise the hygiene of the testing site, capturing dirt in the tendon and ligament strings crossing the joints. Therefore, only dry coatings were investigated. The following methods materials were investigated:
Concentric layer lines (CLL): By orienting the printed parts in such a way that the layers in the head and socket of the joint are concentric, mechanical keying is prevented, which could reduce friction. This

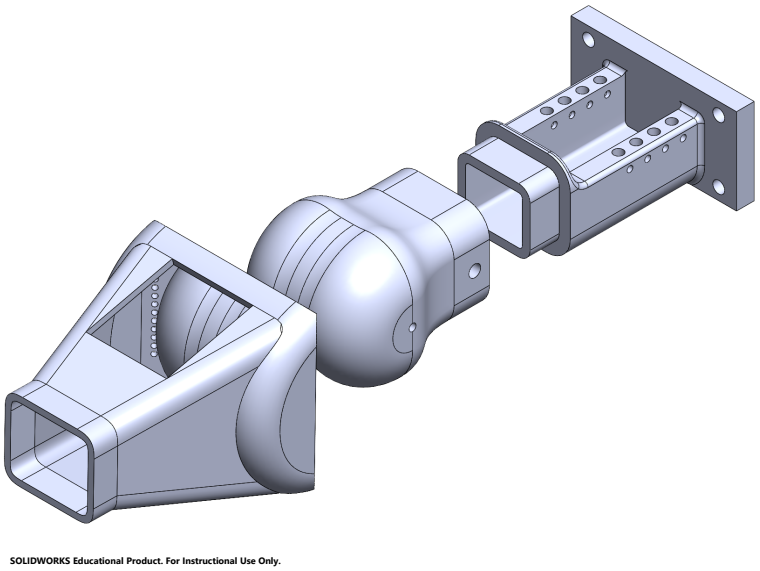

Figure 5.1: Exploded view of the assembly of the test joint. The bicondylar head in the middle is fixated to the base on the right with bolts. The socket on the left is connected to the head through strings between the lateral edge of the socket and the midpoint of the spherical head.

method requires no extra post-processing time or effort as discussed in Section 4.4.1.
Tungsten disulphide in wax solution:
Tungsten disulphide (WS2) is an inorganic chemical compound composed of tungsten and sulphur. WS2 is often used as a solid lubricant in bushings, shafts and other satellite components.[37] It's low friction is caused by its molecular structure, which consists of stacked triple layers formed by a Tungsten (W) Atom sandwiched between two Sulphide (S) atoms. In the three-layer stack, W and S atoms are bonded by strong ionic-covalent bonds, while the structure formed by these three layers is held together by weak van der Waals forces.[12] As the WS2 layers are connected by weak van der Waals forces, interlayer sliding occurs easily causing a low friction coefficient.[46] Usually, a thin film coating is applied using sputtering, this method was not available at the time. An alternative to sputtering in this situation was to apply the WS2 in a liquid wax medium. This was purchased from `www.Silca.cc`
WS2 in wax solution with added graphite powder:
Graphite powder is often used as a dry lubrication and as additive in lubricating oils which improve friction and wear performance.[48] In this experiment, graphite powder was added to the WS2 in the liquid wax medium to investigate the interaction of these two lubricants and to examine the friction properties of such a composite.
Epoxy: Epoxy resins are a class of reactive thermosetting polymers. They are characterized by the presence of a three-membered cyclic ether group commonly referred to as an epoxy group, 1,2-epoxide, or Oxirane.[35] Initially, an epoxy resin is commonly in liquid state and mixing with a curing agent causes a chemical chain reaction where the epoxy resin polymerizes to create large polymer chains and becomes a hard and tough material. Epoxy resins are commonly used as protective coatings because of their good adhesion to many materials and tough finish. For this experiment, XTC-3D (Smooth-on Inc. Macungie, PA, USA) epoxy was used. This epoxy was readily available and specifically designed to create smooth surfaces for 3D printed parts.
Graphite powder in epoxy: Adding graphite as a composite with epoxy has shown to reduce the friction coefficient by almost 50 percent [29]. This makes it a good candidate for a coating. A problem with graphite is that particles are conductive and could cause short circuits of nearby electronics.

5.2.3. Coating procedures

For each test, a test joint was 3D printed and sanded down with 400 grit sandpaper to remove the layer lines and other surface variabilities (excluding CLL). The convex head of the joint was then polished on a bench polisher. The concave socket of the joint was polished with a smaller polishing pad on a multitool because the bench polisher was too big to effectively polish these surfaces.

WS2 application

The WS2 wax was dripped on the surfaces and spread using a brush. Two preparation methods were used and tested. (i) At one test joint, a single coating was applied and left to dry for 1 hour followed by the removal of the wax residue, using a microfiber towel at room temperature (18°C). (ii) At a second test joint, two layers of WS2 wax were applied, with intermediate 1 hour drying time, without removing the wax residue to examine the effect that the wax has on the friction properties.

WS2 with graphite powder application

The WS2 wax was manually mixed with a 10% weight fraction of graphite powder, which is sufficient to reduce friction in another study.[41] After mixing, the mixture was applied to the joint surfaces with a clean brush and left to cure at room temperature for 1 hour.

Pure epoxy

The epoxy resin was mixed with the hardener in accordance to the manufacturer's instructions in a 2:1 volume ratio for one minute. After mixing, the coating was applied to the joint surfaces with a brush. The coating was left to dry for 24 hours to ensure complete hardening.

Epoxy with graphite: Earlier tribological studies on graphite powder with epoxy resins[33] show that a weight fraction (total mass) of 50% graphite powder to epoxy resin would yield the best friction results. Two preparation methods were used and tested. (i)The entire volume of graphite powder was added to the fluid at once. Fine mixing required about two minutes. Thereafter, the hardener was added, at a volume ratio of 2:1 of resin (without powder) to hardener. After mixing thoroughly for one minute, the obtained coating was applied to the joint surfaces with a brush and left to cure for 24 hours. (ii) After application of the coating described above, a second layer of pure graphite powder was applied to the surface of the joint to examine the effect of additional loose graphite powder on the friction properties. After application of the epoxy coatings, the coated surfaces were lightly sanded with 400 grit sandpaper and polished to remove any brush lines.

5.2.4. Experimental set-up for quantifying joint friction

To quantify friction, appropriately coated standard test joints were mounted in the test bed in which they could be actuated, while sensors measured the tendon forces and displacements. A motor actuated the extensor tendon, while the flexor tendon was passively pulled by a vertically suspended mass. The difference between the work done by the motor and by the gravitational force of the mass was taken to quantify energy losses by friction and used to compare the different coatings. Although the tendon pulleys also caused energy losses, these did not likely differ significantly between experiments conducted at the same speeds with the same loads. Given the fact that the test joints were of identical material, geometry, mass and fixation, the only significant variable between experiments was the joint's coating.

The experimental setup

The joint was mounted horizontally on a rigid aluminium frame, within which the tendons were horizontally actuated. The extensor tendon was actuated by a controllable motor. The flexor tendon was guided over a pulley wheel, allowing to change the tendon direction angle vertically and the attachment of a vertically free hanging mass. Ball bearings in the pulley wheel minimized friction. In both tendons, the tendon forces were measured by intercalated load cells, suspended within the work line of the tendon. The tendon displacements were measured by looping the tendon strings around pulley wheels of known diameter, of which the rotations were measured by potentiometers Figure 5.2.

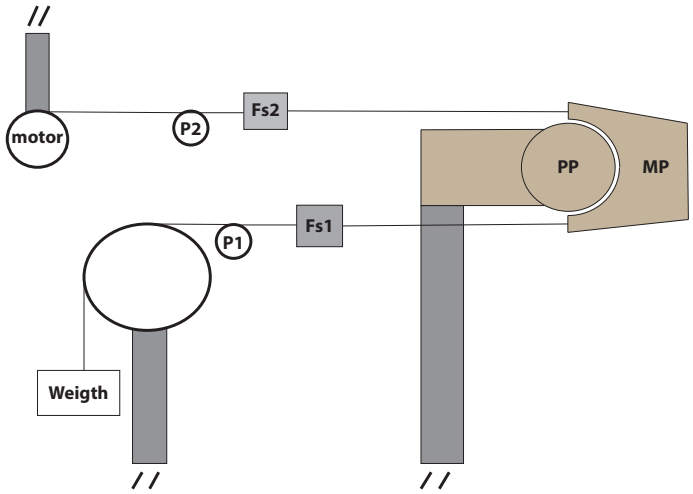

Figure 5.2: Schematic of the friction test setup. The middle phalanx (MP) rotates over the surface of the proximal phalanx (PP) with the upper tendon attached to a stepper motor. Force sensor Fs2 and potentiometer P2 are connected in series to the tendon. The lower tendon is attached to a weight through a pulley. Force sensor Fs1 and potentiometer P1 are connected in series to the tendon. The servo motor, PP and the pulley wheel are attached through a pillar to the environment.

Kinematic evaluation of the joint moment arms

The resultant moment arm of the tendons on the test joint changed slightly due to the rotation of the insertion point of the tendon. In Figure 5.3, the forces and moment arms are shown.

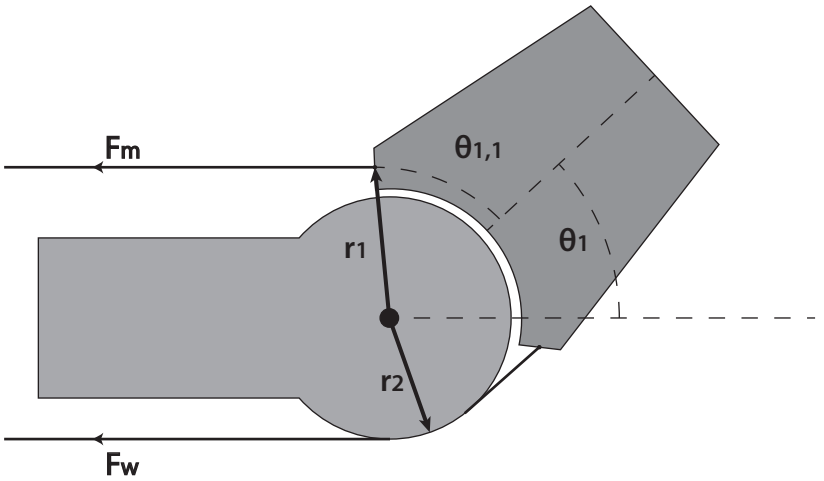

Figure 5.3: Schematic of the test joint with the tendon forces F_m (motor force) and F_w (force from the weight) and their moment arms r_1 and r_2. The moment arms are dependent on the joint angle $theta_1$, and the angle $\theta_{1,1}$ between the midline and the insertion point of the tendon.

The moment arm for the extensor tendon can be derived with:

$$y_{insertion1} = r_1 = r_{i1} * \sin \theta_{i1} \tag{5.1}$$

With r_1 the moment arm and vertical distance between the rotation point of the joint and the insertion point of the tendon, r_{i1} the radius of the path of the insertion and θ_{i1} the angle between the x-axis and

the line between the insertion and rotation point. This angle is the sum of the joint angle and a constant angle $\theta_{1,1}$: $\theta_{i1} = \theta_1 + \theta_{1,1}$

$$r_1 = r_{i1} * \sin(\theta_1 + \theta_{i1}), \text{for } r_1 \geq r \tag{5.2}$$

With r being the radius of the ball of the joint. The same procedure can be done with the opposite tendon and insertion. The difference is that the constant angle $\theta_{1,2}$ is negative.

$$r_2 = r_{i2} * \sin \theta_{1,2} \tag{5.3}$$

$$\theta_{1,2} = \theta_1 - \theta_{1,2}$$

$$r_2 = r_{i2} * \sin(\theta_1 - \theta_{1,2}), \text{for } r_2 \leq -r \tag{5.4}$$

When $r_i \leq r$, the tendon touches the joint surface and the moment arm remains r.
The constants r_{i1}, r_{i2}, $\theta_{1,1}$ and $\theta_{1,2}$ can be measured from the geometry of the joint components. Because the rotating phalanx is symmetrical, the radii and constant angles are equal, resulting in $r_{i1} = r_{i2}$ and $\theta_{1,1} = \theta_{1,2}$. From the geometry, $\theta_{1,2}$ is found to be 68°, r_1 is 5.08 mm and r_{i1} is 6.5 mm. With these parameters, the moment arm as a function of the joint angle are shown in Figure 5.4.

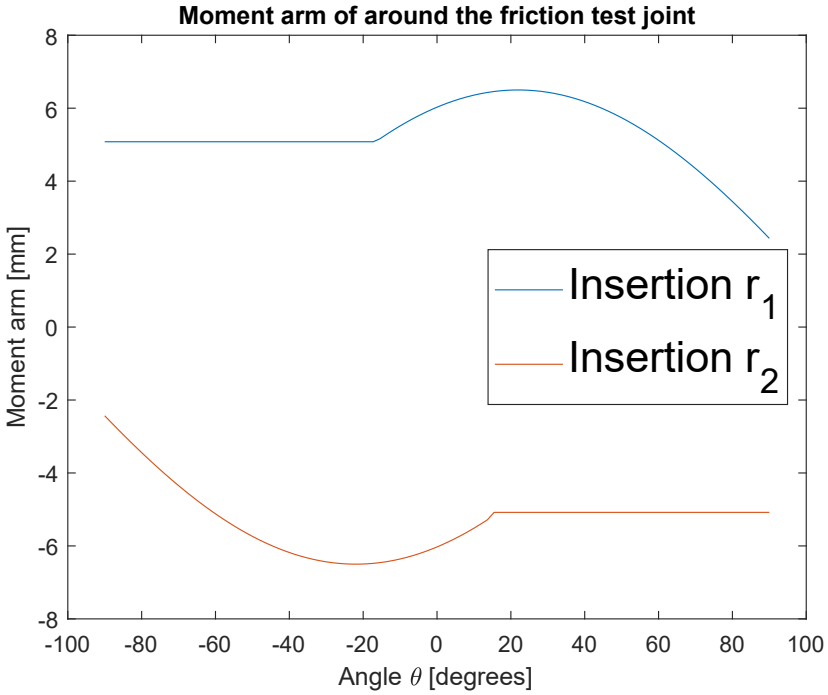

Figure 5.4: Moment arm of the phalanx as a function of the joint angle.

Motor choice

For the actuation of the test joint, a choice had to be made between using a servo motor or a stepper motor. To come to a decision, the experimental procedures needed to be analysed. Because of the mass attached to the flexor tendon, high accelerations would result in high inertial forces, complicating measurements and data interpretation. Therefore, the experiments needed to be limited to low accelerations. Since the distance over which the tendons travelled was only 30 mm, low accelerations implied overall low tendon displacement speeds.
The motor only needed to realise a repetitive 1DOF motion with high accuracy. Pulling the extensor tendon in direct line, the motor functioned in an environment without disturbances, so that the correcting properties of a feedback control system were not necessary. Thus, a feedforward controller was sufficient for the experiments.
Stepper motors: Stepper motors have a "teethed" magnetic rotor, with the magnetic poles at the ends of the rotor. This means the teeth on one end of the rotor are all either north or south. The stator consists of teethed electromagnets surrounding the rotor, with the winding organized in two poles.

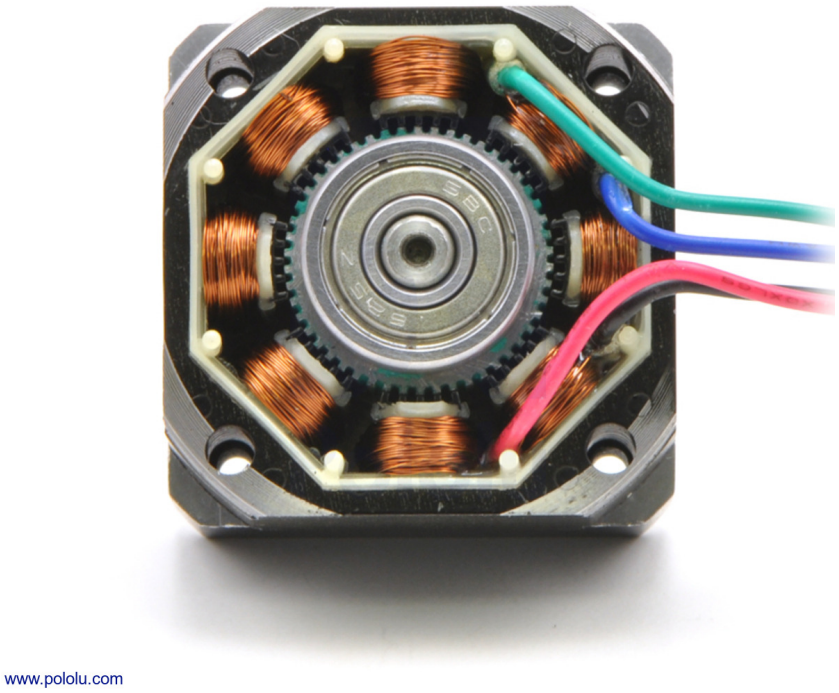

Figure 5.5: Stator and rotor combination of a bipolar stepper motor. When a set of coils are energized, the teeth of the rotor align with the teeth of said energized coils. Image retrieved from `www.pololu.com`

To make the motor shaft turn one step, a controller energizes a pair of stator windings, magnetizing the cores. This causes the magnetic teeth of the rotor to align with the teeth of opposite polarity of the stator. Once the teeth of the stator and rotor are aligned, the coils adjacent to the previously energized coils are energized for a next step, causing the rotor to move to where the energized stator teeth align again with the rotor teeth. Increasing the signal's frequency increases the speed of the rotor. The nature of actuation of a stepper motor means that a stepper motor does not require feedback to accurately position the rotor.
Servo motors: Pulse width modulation (PWM). By changing the duration of the pulse, the position of the rotor changes. Internal H-bridge circuit to control the direction of rotation. Connected to the rotor is a potentiometer that reads the position of the rotor as a voltage.
Servo motors have a built-in encoder to give position feedback.

Table 5.1: Comparison of the general characteristics of, and differences between stepper motors and servo motors

Stepper motor	Servo motor
Higher torque at low speeds	Higher torque at higher speeds
Feedforward control system	Feedback control
Low setup cost	Higher cost

A stepper motor was used for this experiment because of its higher torque at lower speeds and its open loop control system. The stepper motor was a Wantai Nema 17 stepper motor with a rated current of 1.7A and a holding torque of 45 N/cm.

5.2.5. Force and position sensors. Data acquisition and calibration

A Futek S-beam load cell(Futek, Irvine, California, USA) and a potentiometer were attached in series to both the flexor and extensor tendons to simultaneously measure the force and displacement of the tendon. A load cell is a device that converts a force (in this case pulling force on the tendon) into an electrical signal. This load cell consists of an S-shaped beam made of steel with a strain gauge, where the output voltage increases proportionally with the force exerted on the load cell. A potentiometer works as a variable resistor where the output voltage increases proportionally with the rotation of the internal shaft. The signals of the load cells and potentiometers are gathered in a USB-6009 Data Acquisition (DAQ) device (National Instruments, Austin, Texas, USA) and sent to the computer via a USB-cable. The signals from the DAQ device were read in Labview (National Instruments Corp., Austin, Texas, USA), where the voltage outputs from the sensors were scaled to a readable force/angle output.

Calibration of the load cells and potentiometers

The signal from the DAQ device was a voltage between -10V and 10V that needed to be scaled to a force output. The scaling from a voltage to a force output was done by implementing a linear scaling in Labview according to Equation (5.5).

$$F_{output} = SF \cdot (V_l - V_0)[N] \tag{5.5}$$

With SF being the multiplication factor, V_l the voltage output of the loadcell at a given weight and V_0 the voltage output of the loadcell at zero load. To calculate the multiplication factor, the relation between a known applied force and the voltage output needs to be found. This is done by hanging the load cells vertically and adding a known weight to the load cell and left to hang still. The voltage output was then measured for 10 seconds. The median voltage output was then used for V_l to account for fluctuations in the measuring system. First a measurement with zero load was performed to find V_0 followed by a measurement with the weight of the system holding the weights with a measured mass of 25 grams. From there, incremental weights were added. Because the stepper motor has a maximum torque of 45 N/cm, the voltage output was measured for different weights up to 5 kg.

With the measured data, a linear regression of the voltage as a function of the added mass was performed. Assuming a linear relation as $a \cdot x$ between the force applied on the load cell and the voltage output with a linear coefficient $a[kg^{-1}]$, the voltage output of the load cell can be written as:

$$V_l(m) - V_0 = a \cdot F_g(m) \tag{5.6}$$

With independent variable F_g the force of the added weight attached to the load cell which results in $F_g = m \cdot g$ with g the gravitational acceleration of 9.81 [m/s^2] and the linear coefficient a which was derived from the linear regression on the calibration data. The voltage outputs at a given weight together with their linear regression is shown in Figure 5.6.

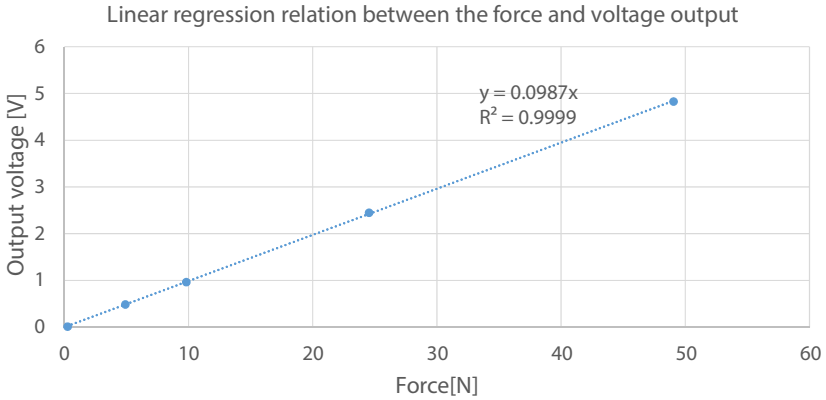

Figure 5.6: Voltage from one of the load cells with respect to the applied force from the added mass. The linear trendline is shown above with their slope and R^2 value

The scaling factor SF is the inverse of a in Equation (5.6). This results in the scaling factor to be $\frac{1}{a}$.
For the two used load cells, the multiplication factors were calculated to be 11.243 and 10.198. This resulted in the measured force from the load cells to be similar to the gravitational force of the weights.

5.2.6. Controlling the flexion and extension of the joint

The stepper motor is controlled by an Arduino Uno (Arduino SRL, Monza, Italy) microcontroller with a Pololu DRV8825 Stepper Motor Driver (Pololu Corp. Las Vegas, Nevada, USA). The system was powered by a 12V constant voltage supply. To ensure the safe functioning of the motor and the controller, the current was limited to 1.2A per phase by adjusting the variable resistor on the stepper motor driver. An open-loop control system was implemented that would rotate the stepper motor 54°clockwise and counterclockwise in 2 seconds for a cycle. This procedure would continue for 100 seconds for a single trial. To reduce the effect of inertial forces during the acceleration and deceleration between cycles, a gradual acceleration was used.

Microstepping

Because a stepper motor works in discreet steps to rotate the shaft, the motors rotation is not perfectly smooth. Stepper motors can show high vibrations and noise at low speeds. To reduce this, a method called microstepping is used. This method divides each step into smaller "microsteps": By applying a current to the coils in incremental steps similar to a sinusoidal wave, the magnetic force on the rotor increases smoother, which results in a gradual movement to the next step. An example is shown in Figure 5.7.

Applying currents to both phases of the motor creates a torque phasor proportional to the vector sum of both currents.[3] When the phasor completes one full “turn” (2π electrical degrees), the motor moves exactly four full steps. Likewise, when the phasor moves $\frac{1}{8}\pi$, the motor will move 25% of a full step. Thus, the position of the motor is determined by the angle of the torque phasor. The current in two phases are energized incrementally, similar to a sinuoidal wave with a phase shift of 0.5 π. The vector sum of the torque phasors of both phasors will be the direction of the magnetic field. This allows the stepper motor to perform intermediate steps between each step.

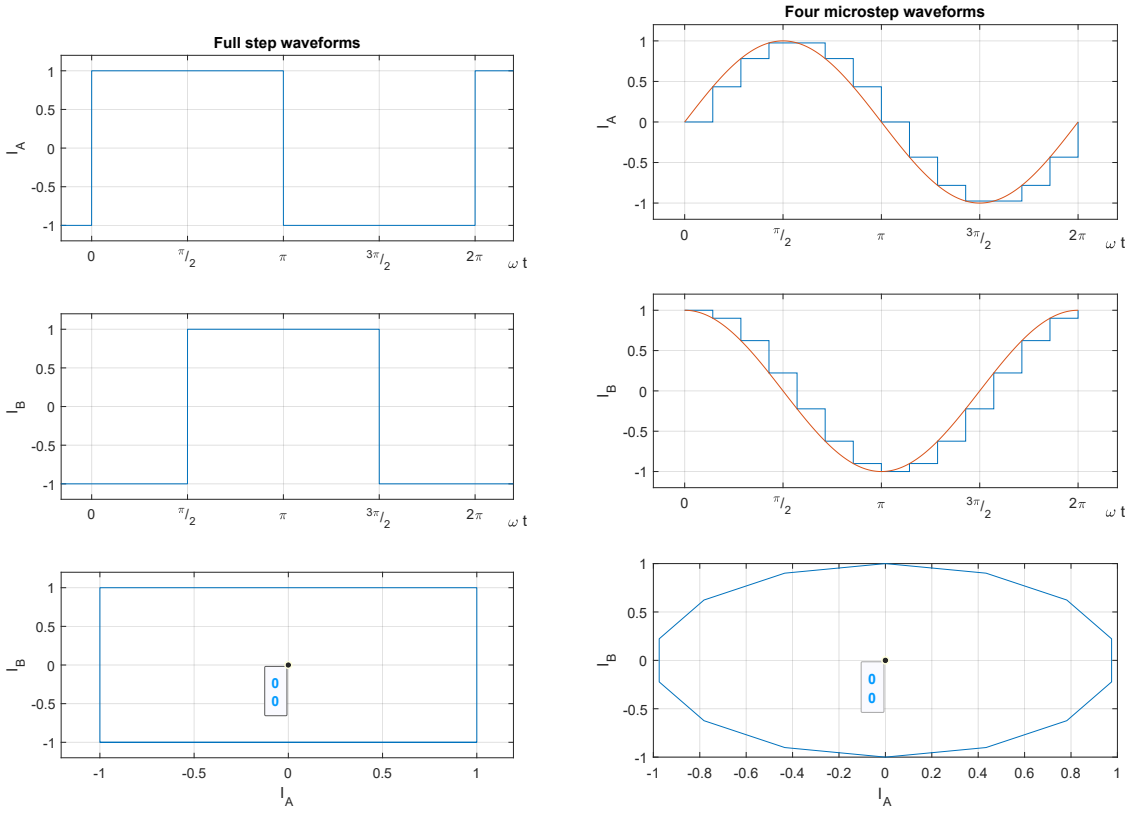

Figure 5.7: Waveforms for a bipolar stepper motor. *Left*: Full step drive wave. *Right*: Four microstep wave. The blue lines represent the wave signal. The red lines represent an ideal sinusoidal wave. Applying a four-step wave to a stepper motor results in a much softer jump between discreet current steps.

5.2.7. Data processing

The force and angle attained from the force sensors and potentiometers were extracted in Labview (National Instruments Corp., Austin, Texas, USA). Data was saved in .txt files and processed in MATLAB (MathWorks, Natick, Massachusetts, USA). The starting time and angle of every measurement could differ slightly due to variations caused by manually starting the measurement and the changing of the joint specimens during the experiments. A strategy needed to be made to extract the data such that it could be used to correctly compare the individual cycles and trials of all tested surface treatments. For this, a MATLAB script was written that automatically extracted the data from each file, identified every extension motion from a cycle and calculated the required work for each extension.

Work calculation

Identifying extension by finding the element number where the angular displacement of the upper tendon has a positive gradient. This results in an array of positive integers corresponding to the displacements associated with extension. This array has increments of 1 in a single extension motion. The start of the individual extension motions can now be found by identifying the jumps in increments of 1. Because they represented a later timestamp.
With the individual extensions separated, the work on the flexor and extensor tendons was calculated. The work was calculated by integrating the force on the tendon over the linear displacement of the tendon. For a single cycle i during a trial j, the work acting on a tendon was:

$$W_{i,j} = \int_{s_{i,j}1}^{s_{i,j}2} F_{i,j}(s)ds \tag{5.7}$$

With $W_{i,j}$ the work on the tendon, $F_{i,j}(s)$ the measured force on the tendon as a function of the displacement of the tendon, and ds the displacement of the tendon. The linear displacement was calculated by multiplying the angular displacement of the potentiometer with the radius of the attached pulley.

$$ds_i = rd\theta_i \tag{5.8}$$

The work on the tendons as described in Equation (5.7) was numerically calculated by trapezoidal numerical integration in Matlab for every single extension. The work on the lower tendon was subtracted from the work on the upper tendon to get the added work due to friction. And the increase of work relative to the work on the lower tendon was calculated by dividing the added work by the work on the lower tendon.

$$W_{relativeloss} = \frac{W_{up} - W_{low}}{W_{low}} \tag{5.9}$$

smoothness comparison

To determine the smoothness of the joint movement, the force data was smoothened with a gaussian-weighted moving average filter along a window of 10 elements to create a curve without any jerk. This method is useful for reducing periodic fluctuation from a trend in a dataset, such as stick-slip vibrations due to friction. This phenomenon is often found in dry coatings due to the difference between the static, and kinetic coefficients of friction.[15] Thus, if a curve is smooth from itself, i.e. smaller difference between static and kinetic friction, the difference between the unfiltered and filtered data is smaller. The smoothened data was then compared with the actual data by calculating the coefficient of determination of the data curve with the smoothened curve.
A measure for the goodness of fit for a non-linear curvature is the standard error of estimate (SEOE). The SEOE σ_{est} is calculated according to Equation (5.10).

$$\sigma_{est} = \sum_{i=1}^{n} \sqrt{\frac{(y_i - \hat{y}_i)^2}{n}} \tag{5.10}$$

With y_i the measured value from the load cell and $\hat{y}_i$ the value of the smoothened curve at integer i and n the total number of integers in the curves.
In the SEOE, a greater difference equates to a higher error. So a better fit equates to a smaller difference and thus a lower value of the SEOE.

Friction coefficients
The kinetic friction coefficients were calculated Furthermore, the normal force on the Because the moment arm of the tendon is sinusoidal, the point where the joint angle is zero is where the upper tendon force is equidistant to the lower and upper peak at a given cycle.
For a rotational body, the equation for the friction torque[9] is

$$T_f = \mu_k \cdot F_n \cdot r \tag{5.11}$$

Where T_f is the friction torque, μ_k the kinetic friction coefficient, F_n the axial force and r the radius of the sliding surface. T_f is the resultant torque around the joint which is a result of the forces on the upper and lower tendon and their moment arms dependent on the angle θ of the joint.

$$T_f = F_{upper}(\theta) \cdot r_{t_{up}}(\theta) - F_{lower}(\theta) \cdot r_{t_{low}}(\theta) \tag{5.12}$$

The kinetic friction coefficients were calculated at the moment that the angle of the joint is zero. In this position, the moment arms of both tendons are equal to each other, as shown in Figure 5.4. Furthermore, when the joint is in 0°flexion, F_n is the sum of the tendon forces on the joint:

$$F_n = F_{upper}(0) + F_{lower}(0) - F_{fr,t} \tag{5.13}$$

With $F_{fr,t}$ being the friction of the tendons running over the joint surface. Because of the low friction of the dyneema strings that are used as tendons, the friction of the tendons over the joint surface was approximated to 0. Rewriting Equation (5.11) with Equation (5.12) and Equation (5.13), the friction coefficient is then:

$$\mu_k = \frac{F_{upper}(0) - F_{lower}(0)}{F_{upper}(0) + F_{lower}(0)} \frac{r_t}{r} \tag{5.14}$$

The radius of the joint head was derived from the geometry of the joint, and the moment arm of the tendons was identified with Equation (5.2) and Equation (5.4).

5.3. Results

All treatments were tested until 0.5 kg. At higher weights, the polished and concentric lined joint required a force that was too high for the motor to pull. The motor failed at 0.8 kg for the WS_2 joint and the XTC epoxy joint. The other treatments were tested to 1.0 kg.
Force graphs for a polished joint at 0.5 kg are shown in Figure 5.8.

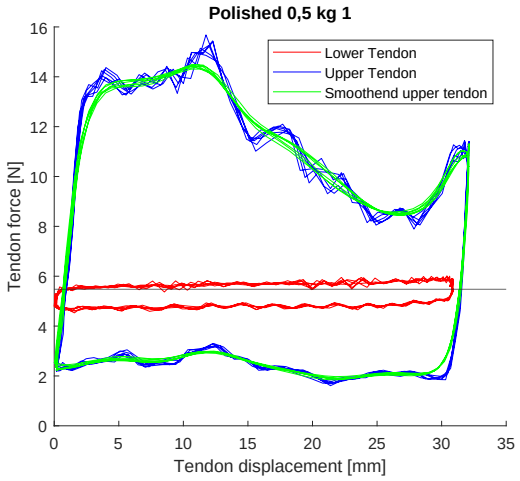

(a) Force on the tendons with respect to tendon displacement, showing the extension and flexion motions plotted over each other. The path starting point is left-under and goes clockwise.

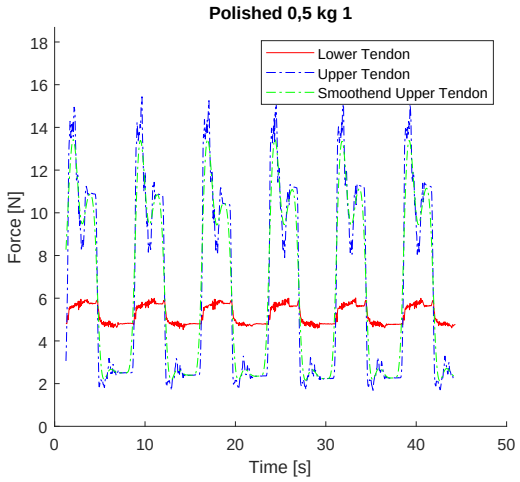

(b) Force on the tendons with respect to time.

Figure 5.8: Force on the tendons with respect to tendon displacement (a) and time (b). The upper part of each path represents the extension of the joint. The lower half represents flexion of the joint

The tendon forces with respect to tendon displacement were plotted over each other in Figure 5.8a. The similarity in forces showed a high level of repeatability and little sign of time-dependant variation in the motion. Because the joint motion started in a flexed position, the moment arm of the upper tendon on the joint was smaller than the moment arm of the lower tendon, as discussed in Section 5.2.4. This meant that the force on the upper tendon would increase due to the lower moment arm. This is seen in the higher force on the upper tendon at lower tendon displacements and reduced forces at higher tendon displacements, since the displacement is related to the joint angle.
The average difference in work between the upper and lower tendon during extension at a given weight are shown in Figure 5.9.

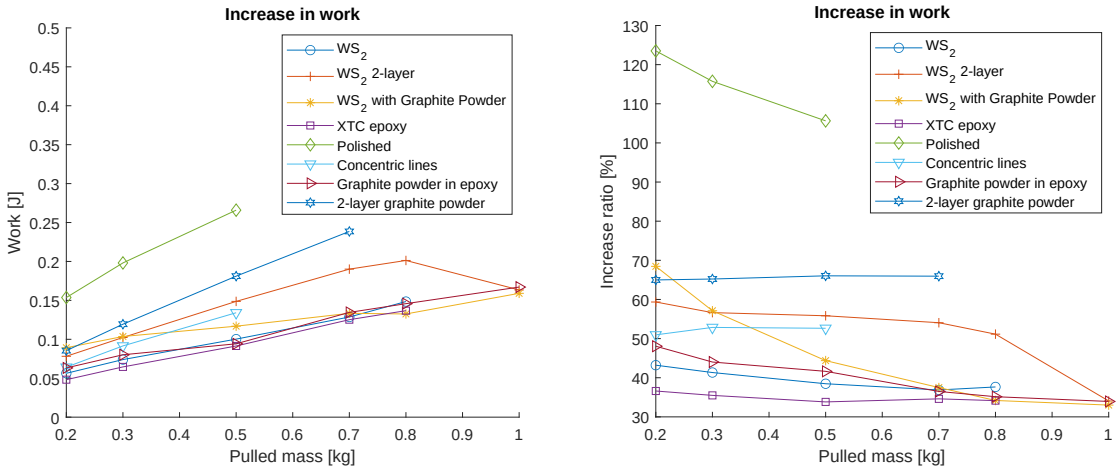

Figure 5.9: Averaged increase in work between the upper and lower tendon as a function of the mass of the weight on the lower tendon. Left: absolute increase in work. Right: relative increase as a percentage of the work calculated in the lower tendon.

A box plot of the required work for each repetition at 0.5 kg is shown in Figure 5.10. For this weight, the maximum interquartile range on the lower tendon is 1.7495% of the median for the polished joint and 2.5114% for the polished joint on the upper tendon. This indicated a low variability between the repeating extension motions.

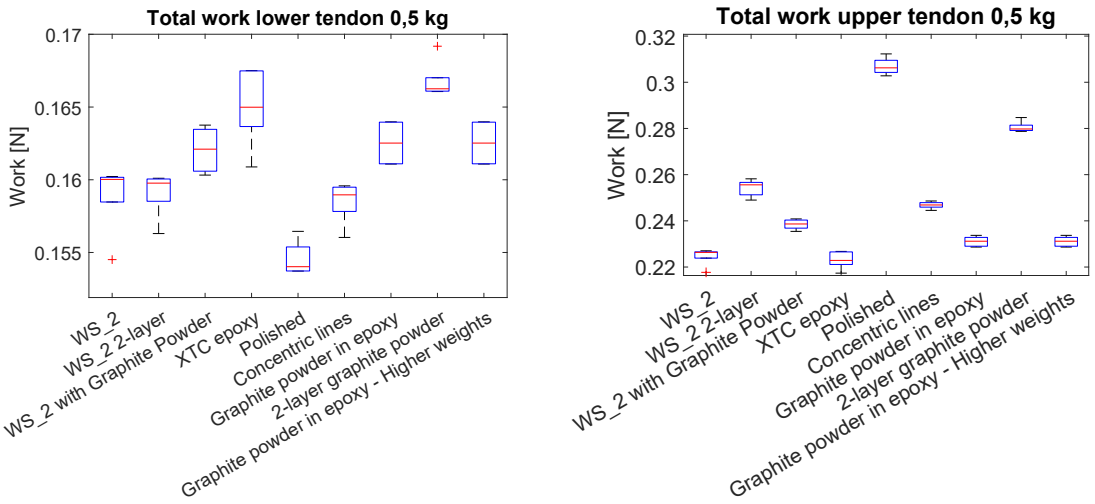

Figure 5.10: Box plots of required work for extension for each repetition at 0.5 kg. In this figure, the maximum interquartile range on the lower tendon (left) is 1.7495% of the median for the polished joint and 2.5114 % for the polished joint on the upper tendon (right).

The epoxy coating, 2-layer graphite powder coating and concentric lines printed joint showed a linear increase in work with respect to the added weight. The relative increase reduced with more weight in the joints treated with Graphite powder in epoxy, WS_2 with graphite powder and the polished joint. However, the relative work increase in the polished joint was more than double the increase of the other treatments. The relative increase of work with the 2-layer WS_2 coating was relatively linear until 0.7 kg, followed by a strong decrease at higher loads.
The kinetic friction coefficients are shown in Figure 5.11.

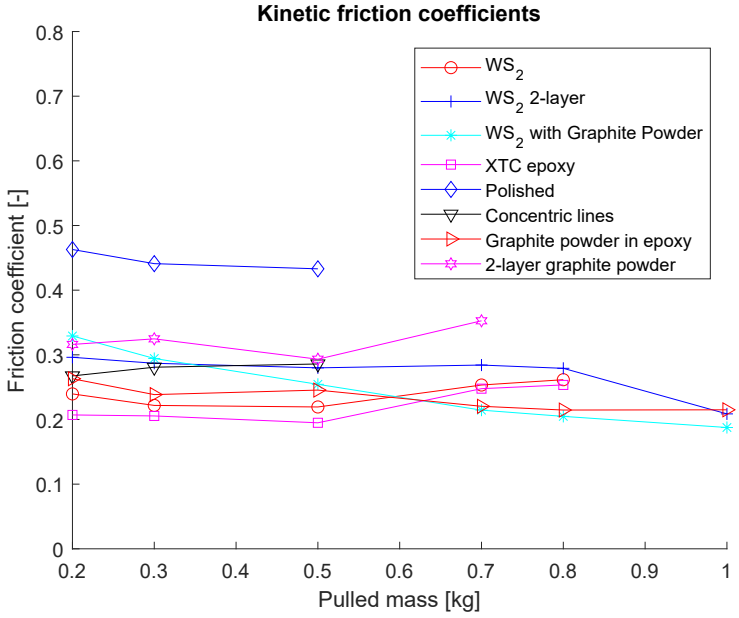

Figure 5.11: Friction coefficients of the different surface treatments at different

At weights up to 0.5 kg, the friction coefficients did not change significantly for most treatments. However, at higher weights, friction coefficients for XTC epoxy, single-layer WS_2, and 2-layer graphite powder increased. Whereas the friction coefficients of 2-layer WS_2, graphite powder in epoxy, and the combination of WS_2 and graphite powder decreased with more weight. In general, the friction coefficients followed a similar pattern as the relative work loss. Which is plausible, as work is the integral of force over the tendon displacement.
The SSEO for the treatments at different weights is shown in Figure 5.12.

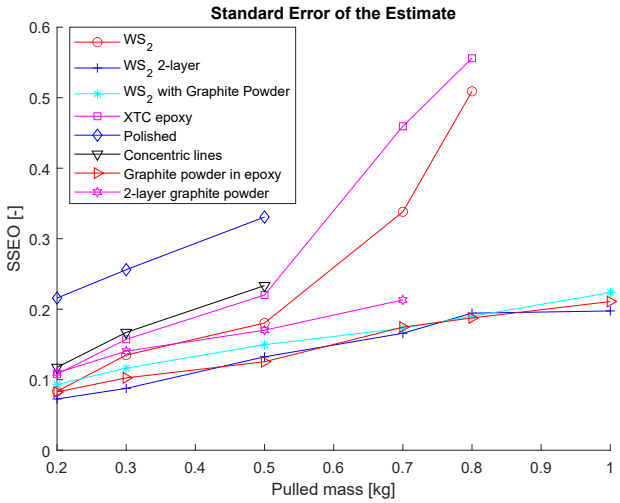

Figure 5.12: Standard Error of the Estimate for the tested treatments compared to their smoothened figures. A higher SEOE indicates a higher difference between the measured data, and a smoothened motion.

At lower weights, there was not a significant difference between SEOE for the different treatments. At higher weights, however, the SEOE for the XTC epoxy coating and the single-layer WS_2 increased significantly compared to other treatments. This can be explained by the higher vibrations, which occurred with these surface treatments, indicating a higher difference between static, and kinetic coefficients of friction compared to the graphite-epoxy composite, 2-layer WS_2, and WS_2 with graphite powder.

5.4. Discussion

The experiments, conducted to find a suitable treatment for the surfaces of the joints, focussed mainly on the extension motion. This was because this motion required the highest force on the tendons. The surface treatments which were tested were chosen based on their availability, and use with FDM printed materials. At the time of this research, WS_2 was only available in a waxy solution, meant for bicycle chains. Even so, the resulting friction coefficients and motion smoothness were promising. Applying this material by sputtering would result in a solid lubrication, which could also provide even lower friction characteristics.

5.5. Selection of the appropriate surface treatment

With the results from the friction experiments, the friction characteristics were identified. After which, a choice was made for the appropriate surface treatment.

Polished The polished joint had the highest amount of friction compared to the other treatments. The kinetic friction coefficient was about 30% higher than the second-worst surface treatment. Also, motion became rough at higher loads with increased vibrations, which was seen in a high SEOE. This suggested a high difference in static and dynamic friction characteristics.

Concentric lines The joint with concentric layer lines had a lower friction coefficient compared to the polished joint. The increase in work was linear with the added mass. However, the increase in work was higher than other treatments and higher loads resulted in a rough motion.

XTC epoxy coating At lighter loads, up till 0.7 kg, the XTC epoxy coating had the lowest increase in work, and one of the lowest friction coefficients. But the motion became rougher at higher loads. This suggested a high difference in static and dynamic friction characteristics, which is not ideal for a smooth motion.

Graphite in epoxy coating At lighter loads, up till 0.7 kg, the graphite-epoxy coating was higher than the XTC-epoxy coating. However, the relative increase with respect to the added weight was lower. At higher loads, the friction coefficient was one of the lowest, and the motion stayed smooth even at higher loads.

2-layer graphite powder Adding loose graphite powder to the joint appeared to increase the friction coefficient compared to the graphite-epoxy composite. Additionally, the increase in required work is linear with respect to the added weight. The motion did stay smooth at higher loads.

Tungsten disulphide - single layer At lighter loads, the single layer WS_2 coating had the second-lowest friction coefficient, and relative increase in work. But at loads higher than 0.5 kg, the motion became rougher, suggesting a greater difference in static and dynamic friction characteristics.

Tungsten disulphide - 2-layer Addition of a layer of WS_2 increased the required work compared to a single layer at lighter loads, as well as increase the friction coefficient. Remarkably, at a load higher than 0.8 kg, the increase in work reduced significantly to one of the lowest increases in required work of all joints. The motion stayed smooth even at higher loads.

WS_2 with added graphite powder The addition of graphite powder to a layer of WS_2 resulted in a higher relative increase in work at lower loads compared to the 2-layer WS_2 treatment, but this increase was reduced at higher loads to reach levels similar to graphite-epoxy coatings and the 2-layer WS_2 treatment. Similar to the graphite-epoxy coating, and the 2-layer WS_2 treatment, the joint motion stayed smooth even at higher loads.

An overview of the added work is shown in Table A.1. Three treatments rose above the rest: 2-layer Tungsten disulphide wax, Tungsten disulphide with graphite powder and the graphite-epoxy coating. At 1.0 kg, the absolute difference between the lowest additional work was 5.06%. Relative to the increase in load, the difference was 1.05%. The interquartile ranges for these coatings were higher than this difference, so the difference in added work was considered negligible. Additionally, the friction coefficients found in these treatments, as well as their SEOE compared to a smoothened motion, were similar. These three treatments were considered in the decision of the final coating.

Graphite-epoxy coating

Being the only coating bonded to the joint surface, graphite-epoxy was the most durable coating. It did not wash away or flow out of the joint after sustained repetition, and therefore did not require repeated addition of lubricant. Furthermore, because it was a solid coating, neighbouring components like tendons and ligaments would not get contaminated by this treatment. The graphite-epoxy coating also showed the lowest increase in work at lighter loads.

2-layer WS_2 coating

The 2-layer Tungsten disulphide wax coating showed a great reduction of added work at higher loads. Suggesting that the friction coefficient of WS_2 reduced under higher loads. Which is consistent with the findings of [37]. The higher friction at lighter loads could have been due to the wax being too viscous, causing viscous friction.

WS_2 with added graphite powder

The WS_2 with added graphite powder did reduce the friction at middle to higher loads compared to the

2-layer WS_2 coating, but the relative increase in work with respect to the load did not reduce as much as only the 2-layer WS_2 coating. The friction coefficient of this treatment, however, was the lowest of all three.

Weighing in the factors described above, the decision was made to make the graphite-epoxy coating the treatment used for the joint surfaces and other low-friction components in the construction of the robot finger. Because while the friction coefficient might be higher than some other considered surface treatments, the fact that the coating is bonded to the joint surface and is completely dry after hardening, made this a more ideal solution. Since a dry coating reduced the possibility of contaminating tendons and ligament, but also would not attract dust or dirt from the environment, ensuring an overall cleanliness of the finger prototype.

6

Assembly of the finger and configuring the ligaments

6.1. Introduction

With all the finger components manufactured, the finger bone segments were assembled into a full functioning prototype with humanoid tendon-ligament systems as outlined in this chapter. A strong base was needed to fixate the finger and the tendon actuators. Following the build of the frame, the finger bone segments were connected with ligament configurations that represented the mechanisms in human joints. After the assembly of the finger segments, the tendon systems were implemented.

6.2. Aim

The aim in this chapter was to assemble all the components of the finger prototype using anthropomorphic tendon-ligament systems that mimic the functional morphology of the human finger. In doing so, a fully functional finger prototype was made that could be manually controlled for demonstration, and testing purposes.

6.3. Methods

6.3.1. Creating the supporting frames for the manipulation of the finger

The supporting frame needed to be strong and stiff in order to carry the weight of not only the finger assembly, but also possible motors and sensors for future research conducted with the prototype. This required also that there was enough space for such future components. To achieve interchangeability of the actuation and sensory components, the supporting frame was assembled from modular aluminium ISB profiles of 40 mm x 40 mm in width. These profiles ensured that the frame could be adjusting in length and width, depending on the configuration, while also enabling the attachment of new components. The mounting area for the metacarpal protruded from the columns of the frame. This ensured that the finger prototype would not travel past the columns, blocking the view of the phalanges during tests at full flexion. The metacarpal was mounted on the frame with a laser-cut plate where the tendons could be strung through.

6.3.2. Configuration of the collateral ligaments and supporting structures

The ligaments were strung through the perforations designed in the head and base of the joints. The lengths of these ligaments could then be adjusted with fixating screws, implemented on the metacarpal, PP, and DP.

The collateral ligaments needed to be arranged such that they were taught enough to ensure lateral stability, but loose enough to enable smooth motion in the joint. In a perfect circular path of the insertion points of the moving socket of the joint, a single string can be strung from the geometric centre of the joint on the head, to the insertion point on the socket. Since the distance from the rotational centre of the joint to the insertion point stays the same, a taut adjusted string would keep the same tension over

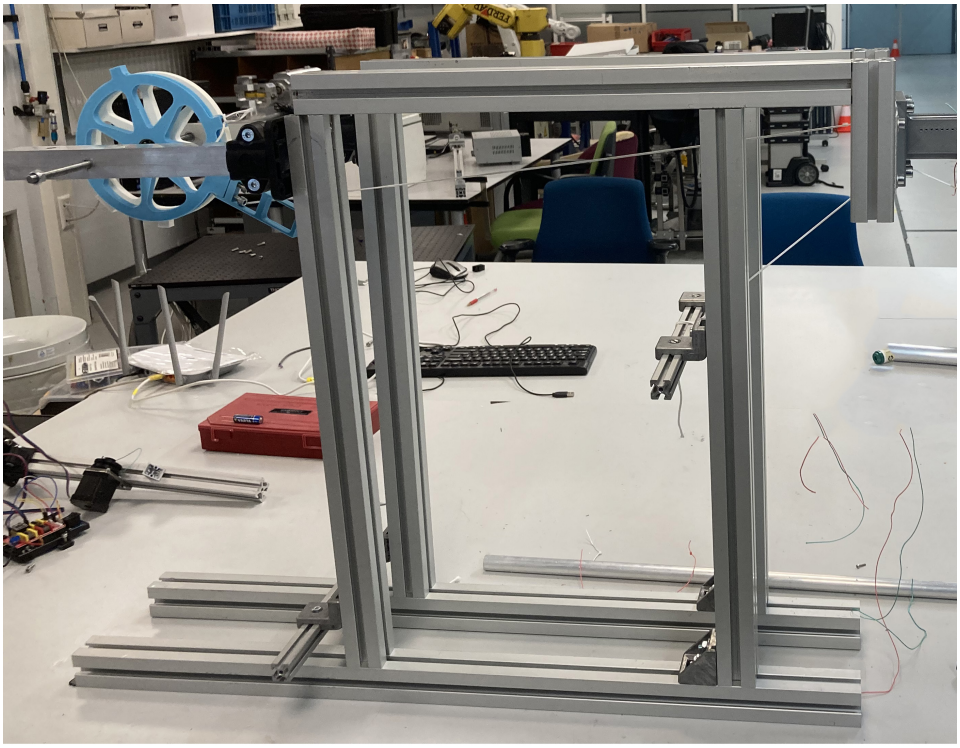

Figure 6.1: Assembly of the frame. Left: Levers for the tendons mounted on a separately attached system. Right: Mounting area for the Metacarpal.

the entire range of motion of the joint and thus ensures lateral stability. However, similar to the human finger joints, using a single strand of fibre might not be strong enough to prevent damage to adhere to the forces on the joint. Furthermore, if the path of the insertion point is not circular but slightly elliptical, the centre of rotation is variable. A single strand of fibre would not be able to keep the same tension throughout the range of motion. To counter these problems, multiple ligament strings made from dyneema needed to be used and arranged in such a way that at least one string was taught at any joint angle.
An insertion point i follows a path $\mathbf{r}_i(\theta)$ with coordinates x and y in a 2-dimensional plane and is dependent on the joint angle θ and location of the location of the insertion point on the moving part of the joint.

$$\mathbf{r}_i(\theta) = \begin{pmatrix} x_i(\theta) \\ y_i(\theta) \end{pmatrix}$$

From the stationary head of the joint, a fibre i is strung to an insertion point i with its origin $\mathbf{s}_i$. This ligament projects a circle $\mathbf{f}_i$ with a radius of the length of the fibre l_i. The coordinates of the projected circle with angle ϕ are:

$$\mathbf{f}_i(\phi) = \mathbf{s}_i + l_i \begin{pmatrix} cos(\phi) \\ sin(\phi) \end{pmatrix}$$

The length and origin of the fibre need to be determined such that the fibre meets the following requirements:

1. At a specific joint angle θ_s, the fibre is taut to ensure lateral stability at that joint angle.
2. The distance between the origin of the fibre and its insertion into the moving base can not be greater than the length of the fibre, which would prevent further joint motion.

This can be realized if the projected circle $\mathbf{f}_i$ lies on $\mathbf{r}_i$ at θ_s but does not intersect $\mathbf{r}_i$ over the rest of the range of motion of the joint.

$$\begin{cases} \mathbf{r}_i(\theta_{s,i}) = \mathbf{f}_i(\theta_{s,i}) \\ \mathbf{f}_i(\theta) - \mathbf{r}_i(\theta) > 0 \quad |\theta_{min} < \theta < \theta_{max} \end{cases} \tag{6.1}$$

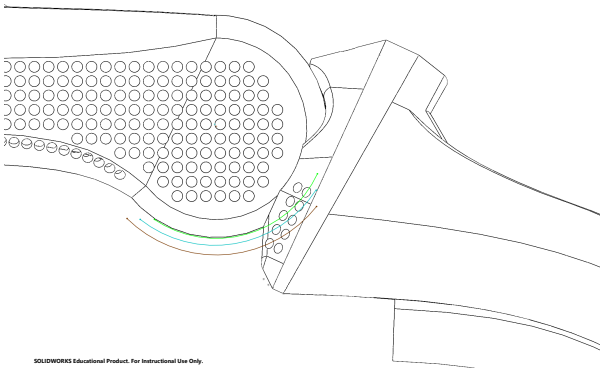

Figure 6.2: Image of the designed PIP joint with the paths of three insertion points.

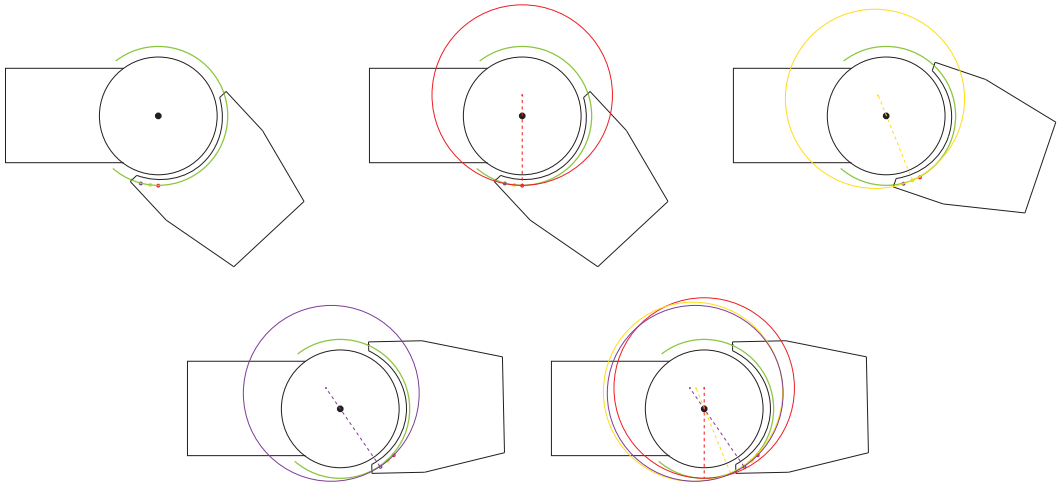

Figure 6.3: Schematic of a hinge joint such as the PIP and DIP joint, with the path of the insertion points on the base (green). extension motion with the ligament string being taught at a specific joint angle and the circle this ligament projects. Bottom right: layout of the ligament fibres together over the joint with their projected circles. Ligament fibres are taught where the projected circle is tangent to the path of the insertion point and slack where the projected circle lies outside the path of the insertion point

Multiple origins and insertion points for the ligament fibres were possible. Therefore, these points were found by systematically fixating individual strands of dyneema through the perforations on the distal joint socket. At different joint angles, the ligament strand was strung through a perforation on the proximal joint head past its centre point of the joint head. Such that the ligament strand was perpendicular to the path of the insertion point, and that the origin was past the joint's centre of rotation. This ensured that the ligament strand was taught in that particular position, but slack in other joint angles.
The described ligament fibre configuration resulted in a set of fibres where the load of the lateral stability was transferred over each ligament fibre over the range of motion of the joint. A schematic of the fibre configuration of the collateral ligaments over the joint's range of motion is shown in Figure 6.3.
For the MCP joint, the individual strings were fixated to the proximal phalanx using a stopper knot, while at the metacarpal, the strings were fixated with a screw to adjust the length. At the PIP joint, the strings were fixated to the middle phalanx with a stopper knot and to the proximal phalanx with a screw. At the DIP joint, the strings were fixated to the distal phalanx with a screw and to the middle phalanx with a stopper knot.

6.3.3. Constraining the range of motion of the finger joints

The main structures constraining the range of motion of the joints in the finger prototype were the volar plates, and the ORL. For all joints, the volar plates were connected firmly to the volar face of the distal part of the joint with dyneema strings. For the PIP and DIP joints, the insertions of the strings on the proximal part of the were placed more posterior to the joint head. The length of the proximal strings of the volar plates was set by extending the joint to its extension limit and tightening the set screws. Once fixated, the strings connecting the volar plates to the finger segments would become taut at the joint's extension limit, preventing hyperextension of the joint. For the MCP joint, the proximal part of the volar plate was connected to the IO tendons. This connection is discussed in Section 6.3.6. The ORL was inserted on one of the lateral faces of the PP. From there, it was strung obliquely across the PIP joint, volar to the joint's rotational axis, and dorsal to the DIP joint. At the DP, it was inserted into the perforations on the dorsum. The length of the ORL was adjusted such, that a slight flexion of the DIP joint was possible with extended PIP joint.

6.3.4. Implementing the extrinsic muscle tendons, extensor apparatus, and supporting ligaments

The flexor tendons were fixated to their respective insertion point in the MP and DP with a stopper knot. They were then strung through the flexor pulleys on the phalanges and the volar plates, keeping the tendons close to the palmar aspect of the finger.

The extensor tendon was first fixated at the middle phalanx. For the assembly of the extensor apparatus, the proximal phalanx was fixated in a straight position using "dummy" collateral ligaments which were tightened and arranged crosswise to prevent any movement. After assembly, these strings were removed. The arrangement and length of the lateral bands followed the mechanisms described by Leijnse and Spoor (2012).[28] The first set of lateral bands were set with the PIP and DIP joint fully flexed. The origin of the first set of fibres in the lateral bands was set dorsal to the axis of rotation of the PIP joint. The fibres were then strung crosswise over the dorsum of the MP and inserted in the dorsum of the DP. In the choses position, the length of the tendon fibres was adjusted to be taught in this position. The procedure for the next tendon fibres of the lateral bands was done similarly for different angles of the PIP and DIP joints. This set of tendon fibres of different lengths resulted in an extensor apparatus, with the load on the tendons fibres was transferred over the range of motion of the finger.

6.3.5. Implementing the supporting ligaments of the extensor tendon and extensor apparatus

The TRL was fixated to the central holes in the volar plate, and was strung in a loop to envelop the lateral bands. The length of the TRL was adjusted such, that the lateral bands were dorsally constrained to just volar to the dorsum of the PP. This ensured that the lateral bands did not snag behind the head of the PP when the PIP joint moved from extension to flexion.

In the finger prototype, the TL was emulated as a string, looped around the lateral bands across the dorsum of the MP. This loop was then attached to the insertion hole of the central tendon of the EA on the MP with another string, after which the longitudinal could be adjusted by lengthening/shortening the string attached to the MP. The width and longitudinal position was adjusted such, that the lateral bands could travel freely along the lateral sides of the PP head, but prevent the lateral bands from luxating palmarly across the lateral face of the MP.

The proximal end of the EA with the PIP in flexed, and half-flexed position is shown in Figure 6.11, showing the load transfer of the lateral bands across the range of motion of the PIP and DIP joints. The supporting function of the TRL, and TL are seen as well.

The ED travelling over the MCP joint is unstable without any supporting structures due to the spherical geometry of the metacarpal head and low friction of the coating. Any deviation of the ED from the sagittal plane would cause the tendon to fall to the lateral edge of the metacarpal. This is prevented by the sagittal bands in the human finger.[49] The sagittal bands originate from the MCP volar plate, and attach to the ED across the lateral face of the MCP joint. The tension from both lateral directions prevents the ED from moving from the midline. Similar to the configuration method described in Section 6.3.2, the sagittal bands needed to be taut at a specific joint angle, and slack at others angles. However, the sagittal bands have moving origins and insertions into the volar plate and the ED. This in contrast to the collateral ligaments, which have a fixed origin on the proximal heads of the joints.

The insertion of a sagittal band fibre onto the ED $\vec{p}_i(\theta_{MCP}, \theta_{PIP})$ travelled along the radial surface of the metacarpal head. Its coordinates were dependent on the ED displacement, caused by MCPJ and PIPJ angles θ_{MCP} and θ_{PIP}. The coordinates of the origin on the volar plate, $\vec{w}_i(\theta_{MCP})$ were dependent on the angle of the MCP joint, since the volar plate is firmly attached to the PP. For most of the range of motion of the MCP joint, the volar plate tightly followed the palmar surface of the metacarpal head.
The fibres of the sagittal band projected a circle, with its origin at the fixation point on the volar plate. With a non-elastic string, this string was taut if the insertion on the ED was on the radius of the circle, and slack if this insertion was within the borders of the circle. For a functionally working sagittal band, with strings being taut in a specific area, and slack in the rest, the projected circle of a string needed to be tangent to the path of the insertion point $\vec{p}_i$. This was synonymous with Section 6.3.2. Differencing from the collateral ligament was that the origin of this projected circle moved with MCP angle.
Because of the spherical shape of the metacarpal head, the direct connection of the volar plate to the PP, and the volar plate moving over the surface of the MC head, any motion of the MCP joint in conjunction with the ED displacement required for only that motion, i.e., extension of the MCP joint with fixed PIPJ angles, has a direct relation between the angular displacement $d\theta_{MCP}$ of the MCP joint, $d\theta_{vp}$ of the volar plate, and $d\theta_{ED}$ of the ED in a 1:1 ratio.

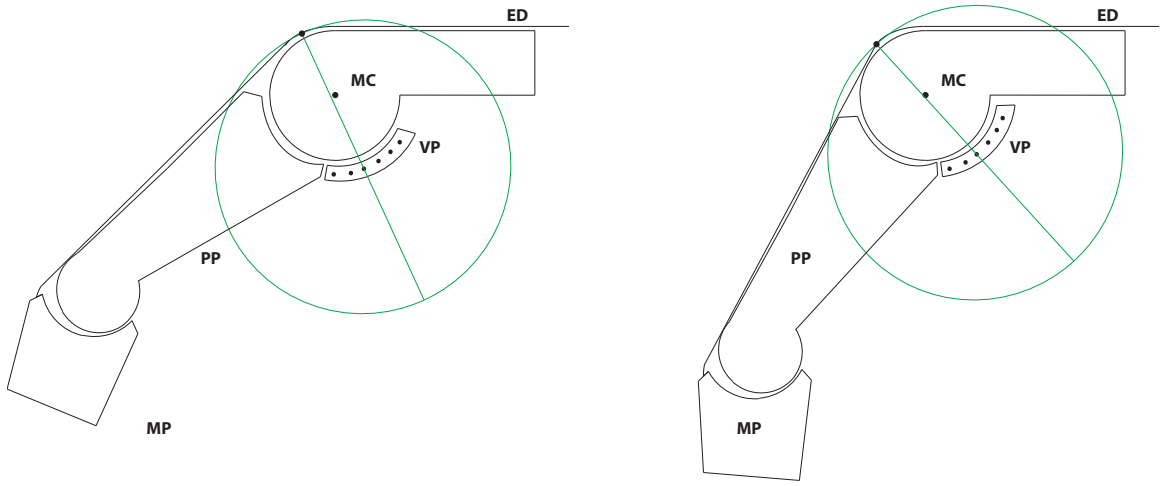

Figure 6.4: Schematic of a taut sagittal band (green) at different MCPJ angles and fixed PIPJ angles. The distance between the insertion on the ED, and the origin on the Volar plate (VP) does not change given a fixed PIPJ angle.

This means that the distance between the origin of a sagittal band string, and its insertion into the ED, does not change during MCP motion with static PIP and DIP angles. This meant that a string of the sagittal bands could be taut at multiple MCP joint angles, depending on the ED displacement.
The sagittal bands of the metacarpal were strung through the ED along the area around the MCP joint with a needle and fixated to the volar plate with screws. The location of the insertions on the ED was chosen with the MCPJ in full flexion and at three PIPJ angles: 90°, 45°, and 0°PIPJ flexion. The point where the ED just still on the MC head was chosen as an insertion point. This ensured the optimal support of the ED. The origins on the volar plate were chosen such, that the strings ran parallel to each other. The length of the sagittal band strings were adjusted to be taut over the MCPJ at 90°, 45°, and 0°PIPJ flexion.

6.3.6. Implementing the interosseus tendons

The interosseus tendons, being the main abductors/adductors and flexors of the MCP joint, were inserted ventral on the lateral face of the proximal phalanx. This resulted in the IO tendons crossing the MCP joint ventral to the flexion axis of rotation when the MCP joint is flexed and extended to 0°.
However, in hyperextension, the IO tendons travel dorsally, reducing the moment arm and thus, the effectivity of the IO for the flexion of the MCP joint such, that in hyperextension of the MCP joint and flexion of the PIP and DIP joints, the IO tendons were not able to straighten the finger. This effect is illustrated in Figure 6.5.

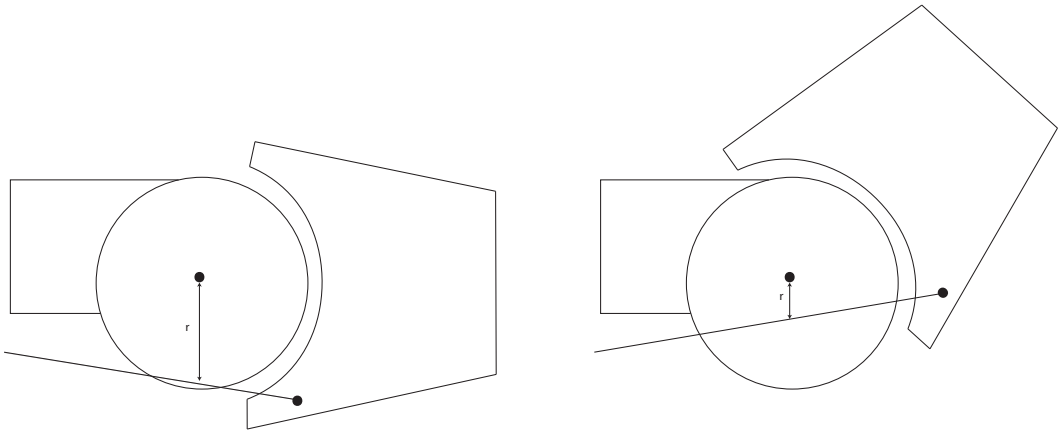

Figure 6.5: Reduction of the moment arm of the interosseus tendon when the MCP joint is in hyperextension.

The solution to this was to attach a second string to the IO tendon more proximal to its insertion at the PP, and attaching it to the volar plate of the MCP joint. This worked because the more volar tendon displacement differed from the displacement at the base of the PP. For a tendon in a joint without a pulley system, such as the IO tendons at the PP base of the MCP joint, the linear displacement of the tendon is not proportional to the angular displacement. Rather, the tendon displacement is related to the spacial displacement of the tendon insertion.

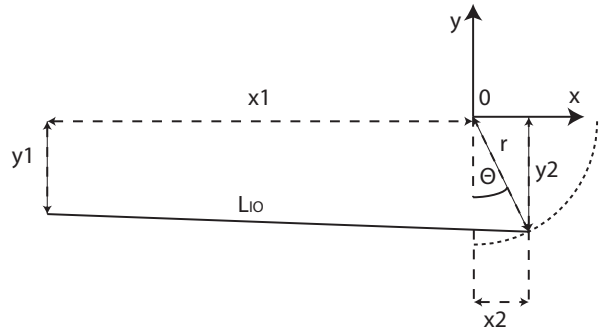

Figure 6.6: Graphical representation of the IO tendon displacement in the finger prototype. With x1 and y1 the coordinates of the IO guide hole at the base of the Metacarpal, x2, and y2 are the coordinates of the tendon insertion at the PP. θ is the angle of the insertion with respect to the negative y-axis, and r is the radius of the path travelled by the tendon insertion.

When the joint moves with angle θ, the tendon length has an x and y component, depending on the radius of the joint r, and angle θ.

$$\vec{L_{IO_1}} = d\vec{L_{IO_1}} + \begin{pmatrix} -x_1 \\ -y_1 \end{pmatrix} = \begin{pmatrix} r\sin\theta \\ -r\cos\theta \end{pmatrix} + \begin{pmatrix} -x_1 \\ -y_1 \end{pmatrix} \tag{6.2}$$

With $d\vec{L_{IO_1}}$ the change in tendon length as a result of the joint displacement θ.
For the IO insertion at the volar plate, the tendon displacement can be assumed linear with the angular displacement, because it travels mostly volar the to the surface of the MC head, with no significant

change in height.

$$dL_{IO_2} = rd\theta \tag{6.3}$$

The displacement of IO_1 is not constrained by the radius of the pulley, but follows the shortest distance, i.e., a straight line. This means that the displacement of IO_1 is less than the displacement of IO_2: $dL_{I_1} < dL_{I_2}$
The string from the IO tendon to the volar plate was set to a fixed length L_{max} using the fixation screws on the volar plate. This resulted in a maximum distance between the connection at the IO tendon, and the volar plate. The distance between the connection at the IO tendon, and the volar plate for the current prototype, can be expressed as a summation of its initial distance, and the difference in deflection between dL_{IO_2} and dL_{IO_1}.

$$L_{IO_2} = L_{IO_{2,initial}} + (dL_{IO_2} - dL_{IO_1}) \tag{6.4}$$

The distance $L_{IO_2}$is shown graphically in Figure 6.7.

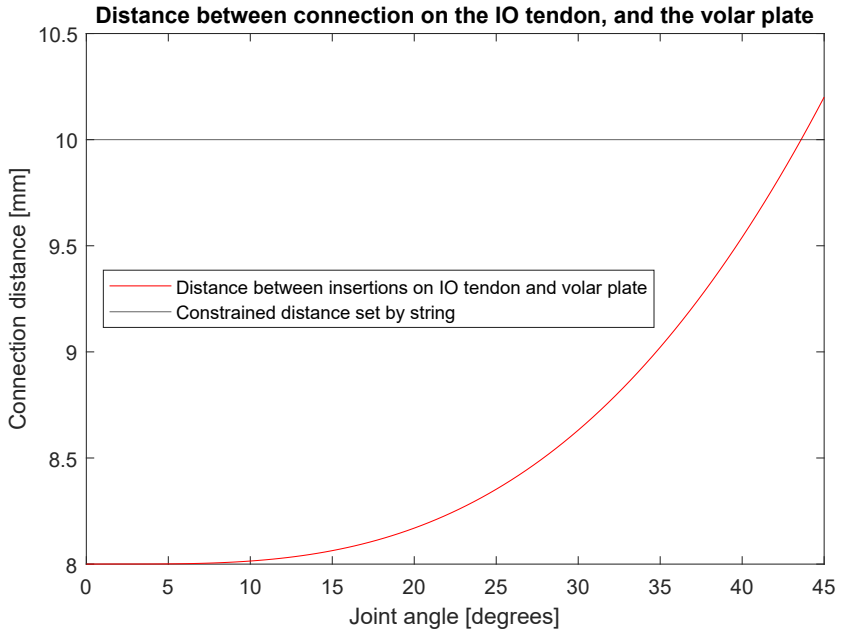

Figure 6.7: Distance between the second string connection at the IO tendon, and the insertion at the volar plate. As the joint moves further into hyperextension, this distance becomes greater, until the set maximum string length is achieved.

When the MCP joint was in flexion and in neutral extended position, this distance was less than L_{max}. But because $dL_{I_1} < dL_{I_2}$, that distance became greater up till L_{max}, at which point, the string from the IO attached to the volar plate became taut.
This displacement was lower than the displacement over a pulley system. When the MCP joint was not in hyperextension, the IO tendons were taut across the entire main tendon. When the MCP joint starts to hyperextend, the displacement of the volar plate increased in comparison to the IO insertion at the PP, because the volar plate followed the path across the surface of the metacarpal head. Because the volar plate is constrained with a maximum length between it and the insertion point on the IO tendon, the load was transferred from the insertion on the PP to the volar plate. Since the volar plate lied ventral to the axis of rotation of the MCP joint, the moment arm of the IO tendon increased. The insertion point in the IO tendon was chosen by hyperextending the MCP joint and fixating the string that would realize the highest moment arm at that position. This resulted in a properly functioning IO tendon system.
The IO tendon assembly is shown in Figure 6.10, showing the tendon attached to the volar plate to be taut at hyperextension, and slack in flexion and in neutral position. This resulted in an increased moment arm for the IO tendon in hyperextension to enable flexion of the MCP joint in this position.

6.3.7. Designing the actuation system of the tendons

For this project, a series of levers was used to move the tendons of the finger. First, the diameter of the flexor pulleys was identified, followed by the extensor pulley and then the pulley for the interossei. This was because the flexor tendons had the largest displacement and thus, the pulley levers had a minimum required diameter. The extensor and IO tendons had less tendon displacement, but mainly the IO tendons had a mechanical disadvantage compared to the flexor tendons due to smaller moment arms in flexion. Therefore, the pulley diameter was reduced for these tendons.
The displacement of the flexor tendons was measured manually over the range of motion of the finger. For the FDP, this was 235 mm. In order for proper manual control, a constraint was that the maximal angular displacement of the lever was π radians (180 degrees). This would result in the lever pointing upward in full extension and pointing downward in full flexion. In general, the equation for linear displacement dL as a function of the angular displacement is:

$$dL_i = r_i * d\theta_i \tag{6.5}$$

Where r_i is the radius of pulley i actuating tendon i and $d\theta_i$ the angular displacement of pulley i.
With the tendon displacement and maximum angular displacement known, Equation (6.5) could be rearranged to calculate the radius of the pulley lever:

$$r_i = \frac{dL_i}{d\theta_i} = \frac{235}{\pi} = 74.8mm \tag{6.6}$$

From the calculation described above, the levers of the flexor tendons were made to have a radius of 75 mm.
The diameter of the lever for the extensor tendons was the same as the diameter for the flexor tendons. This was because the moment arms of the extensor tendon at the MCP, PIP, and DIP joints did not differ critically from the moment arms of the flexor tendons. Additionally, with the same lever diameter, the difference in tendon displacement between the flexor, and extensor tendons could be clearly visualized.
The diameter of the IO pulleys was determined differently. When the MCP is in hyperextension, the moment arm of the extensor tendon around the MCP joint increased as described in Section 5.2.4. Likewise, the moment arm of the interosseous muscles decreased at hyperextension compared to a flexed MCP joint. This meant that in order to straighten a finger from a claw position, the forces on the IO tendons had to increase. With a lever pulley ratio of 1:1, the strain on the IO pulley levers was too great and too much force was required to actuate the IO tendons. Therefore, the force on the interosseus tendon needed to increase without increasing the force on the pulley levers. The force on the tendon is found by dividing the torque on the pulley with its radius.

$$F_{tendon} = \frac{T_{pulley}[Nm]}{r_{pulley}[m]}[N] \tag{6.7}$$

By reducing the radius of the pulley lever, the force on the tendon is increased. From measurements on the realized finger prototype, as well as from the CAD model, the moment arm of the IO tendons was reduced by $\frac{1}{3}$; from 60 mm at fully flexed MCP joint, to 40 mm at hyperextended MCP joint. To compensate for the reduced moment arm, the radius pulley levers of the IO tendons were reduced by $\frac{1}{3}$ to get a diameter of 100 mm. This increased the torque delivered to the MCP joint by the IO. While this also increased the travel of the IO levers, the travel was still small enough that abduction/adduction could be performed with one hand.
The thickness of the pulley levers was made to accommodate two roller bearings, which help in the smooth motion and lateral stability of the levers. The pulley levers were then 3D printed with PLA as material.
On the pulley wheel, a fixation point was made to attach the tendon onto the pulley. This way, the position of the levers could be adjusted. Another fixation point was made for the implementation of tension springs, which would keep the tendons under slight tension to remove any slack.

6.4. Results

The assembly of the collateral ligaments of the MCP joint is shown in Figure 6.8. The collateral ligaments transferred the load over the joint's flexion-extension range of motion, where each individual ligament string becomes taut at a specific joint angle, while remaining slack over the remaining range of motion. At 0°flexion of the MCPJ, none of the CL were taut, which ensured abduction of the joint.

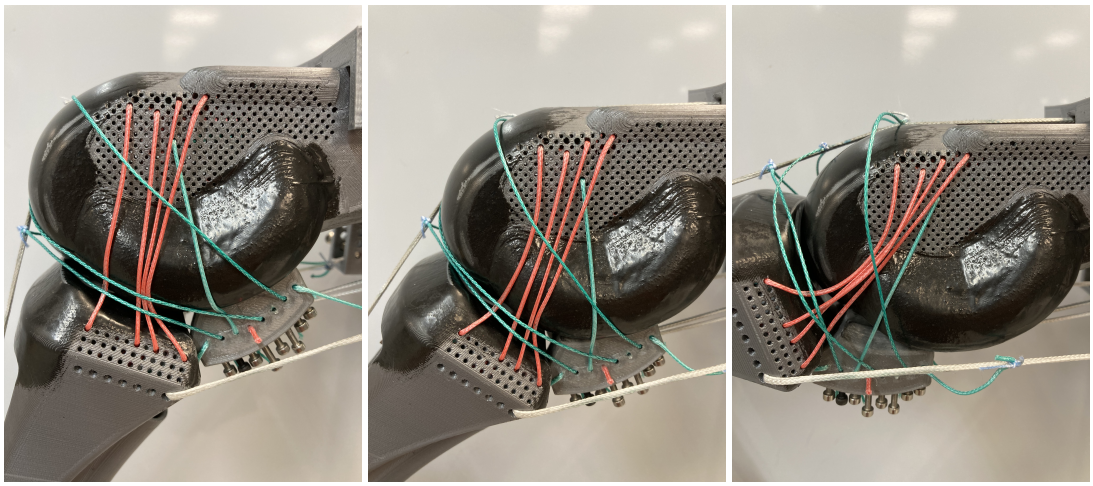

Figure 6.8: Collateral ligaments (red) transferring the load over the flexion-extension range of motion. *Left*: The string second from left is taut at a flexed MCPJ. *Middle*: The two middle strings are taut, showing the load being transferred to adjacent strings. *Right*: Only the most right collateral ligament is taut when PIPJ flexion approaches 0°. *Green*: Sagittal bands, which are discussed separately.

The connection of the volar plates to the phalanges is shown in Figure 6.9. Along with the A3, A4, and A5 pulleys. In extended position, the volar plate followed the volar aspect of the head of the PP. The checkrein ligaments constrained further extension of the PIP joint. In flexion, the accessory collateral ligaments held the volar plate close to the volar face of the PP.

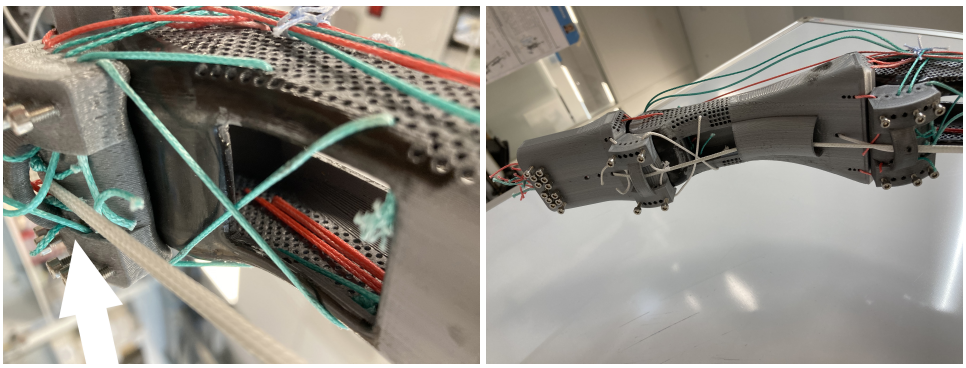

Figure 6.9: *Left*: Volar plate of the PIP joint (arrowed). *Right*: View of the PIPJ and DIPJ volar plates, with flexor tendons strung through the A3, A4, and A5 flexor pulleys.

With the collateral ligaments and volar plates assembled, the finger prototype moved freely in its range of motion, but was held firmly in place by the strings in off-plane motion.
The IO tendon assembly is shown in Figure 6.10, showing the tendon attached to the volar plate to be taut at hyperextension, and slack in flexion and in neutral position. This resulted in an increased moment arm for the IO tendon in hyperextension to enable flexion of the MCP joint in this position.
The configuration of the EA is shown in Figure 6.11, showing the load transfer of the lateral bands across the range of motion of the PIP and DIP joints.
The resulting set of strings representing the sagittal bands is shown in Figure 6.12. While the load on the sagittal bands transferred smoothly over the configured strings with changing PIPJ angles, there were positions with less support. This could be due to using only three strings for the sagittal bands,

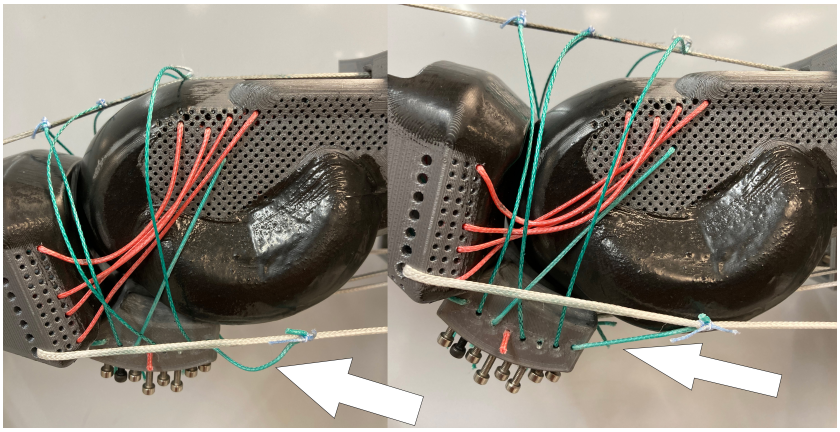

Figure 6.10: Implementation of the Interosseus tendons from a sagittal viewpoint. The thick bottom white string representing the main IO tendon and the green string attached to it, the second point of attachment to the volar plate. At a neutral and flexed MCP joint, the tendon string attached to the volar plate is slack, while in hyperextension, the tendon string becomes taut.

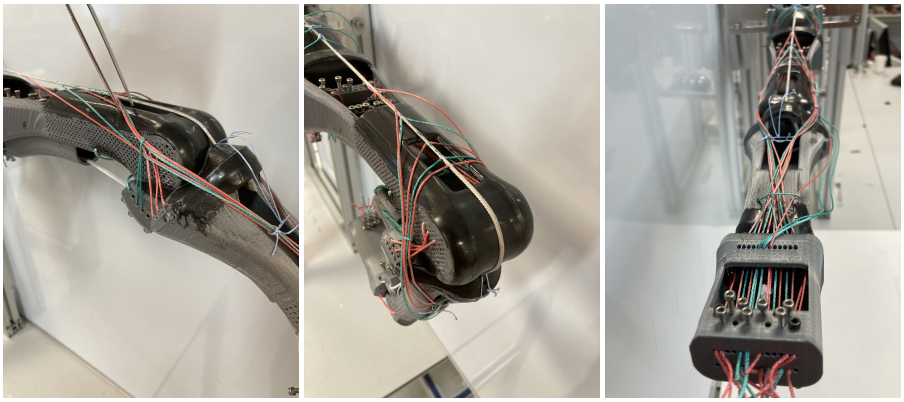

Figure 6.11: *Left and middle*: Proximal end of the Extensor Apparatus, where the lateral bands diverge from the central extensor band and cross the lateral faces of the PIP joint. In half-flexed position, the three most distal strings of the EA (ulnar and radial) are slack, and the extension load is carried by the two distal strings. At fully flexed position, the proximal (red) string is taut, and the proximal strings are slack. *Right*: Conjuction of the lateral bands at the distal phalanx. The lateral bands insert at the proximal insertions points of the DP, close to the joint. At the distal insertion holes of the distal phalanx, the ORL is seen. The string emulating the TL is seen (thin, blue string) constraining the outward movement of the lateral bands across the dorsum of the MP.

and the extensor tendon could momentarily have reduced support where the string is not fully taut. Still, the configuration ensured a ED tendon over the dorsal surface of the MC head.

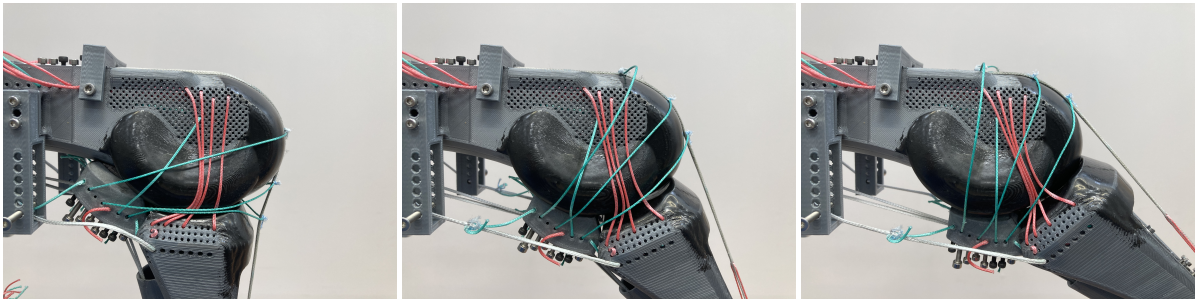

Figure 6.12: Load transfer of the sagittal bands (green strings running from the extensor tendon to the volar plate) over different joint angles

The combined configurations of the different finger bone segments, tendons, ligament structures is shown in Figure 6.13.

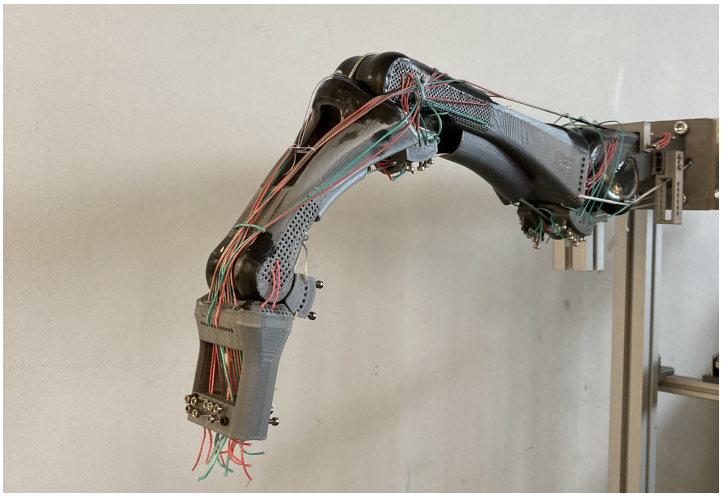

Figure 6.13: Complete assembly of the finger prototype with all the components, needed for the functional motions assembled.

6.5. Conclusion

This chapter outlined the processes involved in the assembly of the finger components designed in earlier chapters into a fully functioning prototype finger with humanoid tendon-ligament systems. It described the steps in connecting the finger bone segments, and identifying the insertions and lengths of the fibres of the extensor apparatus and its supporting ligament such as the sagittal bands, transverse retinacular ligament, and the triangular ligament. Furthermore, a tendon configuration was developed to conserve the moment arm of the interossei over the entire range of motion of the MCP joint. The levers actuating the tendons of the ED and the flexor tendons were designed with the maximal tendon travel in mind, while the levers actuating the IO tendons were designed for higher torque output. The following chapter evaluates the functionality of the model developed with regard to the dynamics of the human finger.

In the configuring of the EA, the insertions originating from the IO tendons were left out because of time constraints, and like the lumbrical, these structures were not necessary for the DOF of the finger. A main challenge for the flexion of the MCPJ in hyperextension with the IO tendons was the reduced moment arm of the IO in this position. The solution to this challenge, adding a second tendon string to the volar plate, did result in proper motions, but this attachment has not been described in the literature. In the human finger, the dorsal movement of the insertions of the IO in hyperextension should happen as well without a supporting structure. This, however, does not occur, and the tendon string attached to the volar plate in the finger prototype suggests that the volar plate of the MCPJ, or structures attached to it, function also as a pulley mechanism for the IO tendons. This confirms a model proposed by Leijnse (unpublished), based on personal dissections and biomechanical considerations, of the insertions of the interossei in the basis of the proximal phalanx and their palmar extensions into the fibrous complex of the volar plate and the accessory collateral ligaments lateral at the palmar base of the proximal phalanx. So that the effective moment arm of the IO tendons remain more palmar than when only the insertion into the base of the PP would be present.

7

Experimentation and evaluation

7.1. Introduction

In this chapter, the kinematics, and coupling mechanisms of the developed finger prototype were evaluated. The tests involved dynamic experiments to verify the mechanisms of the finger prototype, to compare them with the mechanisms of the human finger.
Using motion tracking software, the IPJ coupling mechanism was measured, as well as the AA/AR coupling mechanism. Following these tests, the intrinsic muscle tendons were disconnected to simulate a pathology in which the intrinsics are weakened. The results were compared with previous literature to verify the design of the anthropomorphic finger prototype.

7.2. Aims

The aims of these experiments were to verify that the finger prototype can emulate the IPJ coupling, and AA-AR coupling found in the human finger discussed in Section 1.2, as well as perform basic anthropomorphic finger joint motion. Based on the results, the main aims of this thesis could be evaluated.

7.3. Methods

7.3.1. Setting up motion tracking system

The IPJ and AA/AR coupling were measured with a motion tracking system with passive, reflective markers. The setup, calibration, and measuring was performed by Joris Leijnse with his personal equipment. The finger prototype was placed on a rigid, level table to reduce disturbances. The finger prototype was covered with a stocking to prevent any reflection of the components. Such that only the markers were visible by the tracking software. To measure the rotation angles of the finger segments, marker frames were used that were defines as rigid bodies. These frames were rigidly attached to the finger segments such, that these frames rotate together with the finger segments. In this way, the markers did not have to placed on specific points on the segments themselves, which might not be optimal because of the strings running along the finger surfaces. On top of the MC, PP, MP, and DP, marker frames were placed with three markers on each frame. The setup for measuring the IPJ coupling is seen in Figure 7.1.
The motion tracking was realised with the software Motive (NaturalPoint Inc., Corvalis, Oregon, USA) using 6 Motive Optitrack motion tracking camera's. These camera's were mounted on a frame which could position each individual camera in 5 DOF. The camera's measured at a framerate of 120 frames per second (fps). The measurement process is discussed in the following section.

7.3.2. Measuring the AA-AR and IPJ coupling

The AA-AR coupling was measured with the MCP joint at 0°flexion, and at 15°extension, together with fully extended IPJ's. This was done for radial, and ulnar abduction of the MCP joint. To keep the MCP joint at a specific flexion-extension angle, the extensor tendon was constrained in length by blocking the

Figure 7.1: Marker frame setup for the measurement of the IPJ coupling mechanism. The finger prototype is covered in a black stocking to prevent reflection of the components. The frames are placed above the finger segments with three markers on each frame.

actuation of the lever on the frame. The displacement of the extensor tendon was constrained such, that the finger was fully extended, with the IPJ volar plates preventing any further movement from the PIP and DIP joint. With the finger prototype in position, the MCPJ was repeatedly ab-adducted with the IO tendon pulleys for about 1 minute.
The IPJ coupling was measured with unrestricted tendons and joints. The measurement was performed by flexing and extending the PIP/DIP joints using the flexor and extensor tendon pulleys while maintaining a neutral joint angle of the MCP joint. The flexion-extension motion of the IPJ's was repeated for 2 minutes as well. The captured data in Motive was exported in an xlsx-file where the angles were was subsequently processed in MATLAB.

7.3.3. Implementing a claw deformity

A test to validate the actuation relations is for the prototype finger to perform a claw hand. Claw hand is a deformity in the hand in which one or more fingers are bent into a position that makes the hand look like a claw. It is defined as the hyperextension of the MCP joint and the flexion of the IP joints. The clawing appearance of the finger is caused by weakness of the intrinsics and unopposed pull of the extrinsic extensor and flexor tendons, because the function of the intrinsic musculature is to flex the MCP joint and extend the IP joints. In the finger prototype, the levers for the interossei were disconnected. This simulated weak intrinsic muscles of the finger. In the case of an anthropomorphic tendon configuration, the robot finger would have to result in a claw deformity if the extensor tendon were actuated.
The finger was in a relaxed starting position with the MCP joint flexed and the IP joints in neutral position. From this position, the extensor tendon was actuated.

7.4. Results

7.4.1. Abduction/Adduction−Axial rotation coupling

The measurement data from the AA/AR measurement is shown in Figure 7.2. With the MCPJ at 0°extension, 15°extension, a total of 40 abduction movements were performed. For ab-adduction at 0°MCP flexion, the trajectory of the different ab-adduction movements match closely to each other. However, when the finger is at 15°extension, some drift occurred. Specifically between different sets of abduction, which gives the impression of a more circular motion. In both cases, the axial rotation with respect to the abduction of the MCP joint is clearly visible. At 15°MCPJ extension, the amount

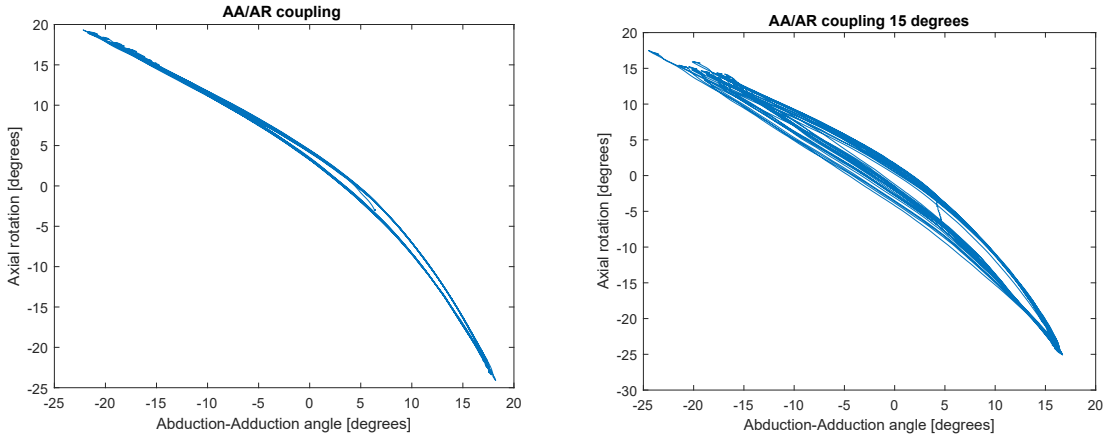

Figure 7.2: Coupling of the ab-adduction and axial rotation of the MCP joint.*Left*: MCP joint at 0°flexion. *Right*: MCP joint at 15°extension.

of abduction that is possible decreased when compared to the abduction at 0°MCPJ extension. This is in line with the theoretical description made by Brand and Hollister[36] and also in line with the measurements of the MCPJ model made by Vis et. al.[42]

7.4.2. IP joint coupling

The DIP joint angle with respect to the PIP joint angle is shown in Figure 7.3. A total of 10 flexion-extension motions were performed. The trajectory of the different flexion-extension movements match

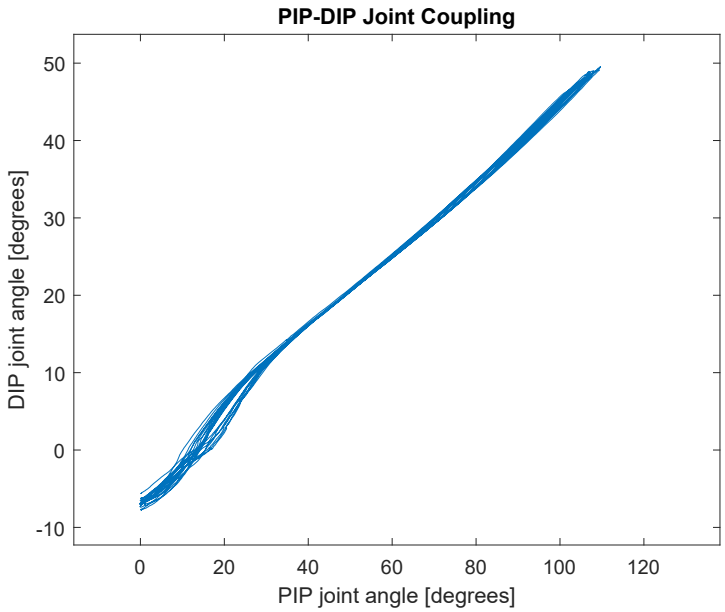

Figure 7.3: Coupled relation between the PIPJ and DIPJ angles. Flexion is positive. At lower IPJ angles, the extension curve (lower lines) dissociate from the flexor curve(upper lines).

closely to each other. This shows that the IPJ coupling mechanism with the designed EA is robust and can be reproduced multiple times. At lower IPJ angles, there is a slight dissociation between the curves for flexion and extension. This phenomenon has been discussed in the work by Leijnse and Spoor[27], where a dominant FDS could flex the PIPJ, but would not flex the DIP joint, which is performed by the FDP. The extension of the IPJ's is not performed by the FDS and FDP, but by the ED and IO tendons. And because the strings of the EA, attached to the ED tendon, are relatively inelastic, there is less variation in the angles of the IPJ's relative to each other. The results for the PIP-DIP coupling reflect the models

developed by Leijnse and Spoor[28], and the measurements by Leijnse and Spoor.[27].

7.4.3. Implementing a claw deformity

The resulting movement of the robot finger when the interossei were disconnected is shown in Figure 7.4.

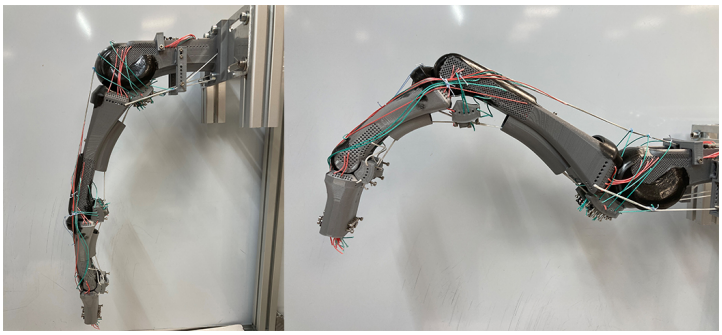

Figure 7.4: Claw deformity, demonstrated by extending the finger from a relaxed position without the contribution of the Interosseus

The claw deformity could be removed by either dorsal compression of the proximal phalanx, or by activation of the interossei. Resulting in extended MCP and IP joints as shown in Figure 7.5.

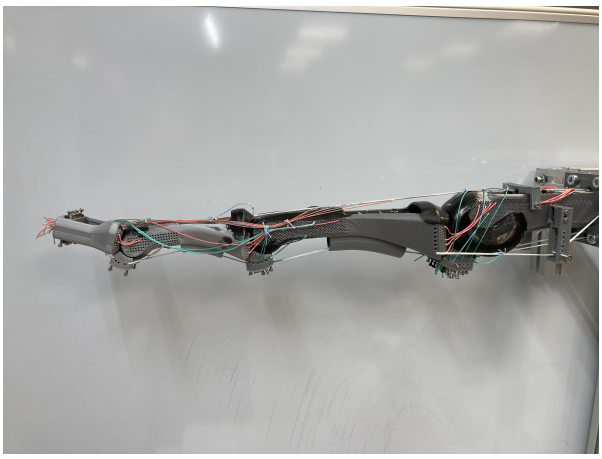

Figure 7.5: Finger extended with active interossei.

7.5. Conclusion

This chapter detailed the final steps in the development of the anthropomorphic finger prototype. The IPJ and AA/AR coupling mechanisms were evaluated with a 3D motion tracking system over multiple repetitions. And the functioning of the finger was evaluated when a paralysis of the IO muscles was simulated. The evaluation showed that the finger had similar movements and coupling mechanisms to the human finger. It also produced humanoid movements when implementing a claw deformity. Thus, the experiments and results described in this chapter verify that the finger prototype has a similar functionality to a human finger.

8

Discussion and Conclusion

8.1. Discussion

8.1.1. Reflection of the developed finger with the aims

The aims of the thesis project were to design a complete anthropomorphic finger model, with (i) anthropomorphic joints, and (ii) anthropomorphic tendon-ligament systems. As a result of these aims, the IPJ and AA/AR coupling mechanisms could be demonstrated. While the finger prototype could be functionally actuated as a human finger, and demonstrated realistic humanoid kinematics when actuated, some limitations were identified with regards to the aims.

At the joints, the finger segments were connected with inelastic strands of fibre, which mimic the function of the ligaments. The main joint ligaments required for the functional movement of the human finger, the CL, ORL, and the volar plates, were implemented in the finger. The volar plates in the this finger model were made of a rigid material in stead of a tough fibrous material, but functioned exactly as found in the human finger as a stopper ligament. With this, the aim of having anthropomorphic joints in the finger prototype is met.

The finger prototype included 5 of the 6 muscles used to move the human finger. Only the LU muscle was left out of the system of actuators because this muscles is redundant with IO muscles for the flexion of the MCP joint.[23] The EA in this finger prototype was constructed with the lateral bands originating from the extensor tendon proximal to the MP, and inserting into the DP. The supporting ligaments of the EA, the sagittal bands, TRL, and TL were functionally implemented to stabilise the extensor tendon over the MCPJ head, and limit the movement of the lateral bands. This tendon-ligament system resulted in a working EA with IPJ coupling, where the load on the fibres of the lateral bands is transferred across the bands with PIP and DIP joint motion. In reality, the EA comprises also of tendon fibres from the IO muscles fanning out to the extensor tendon. Due to time restrictions, this structure of the EA was not implemented. However, this system was redundant with the insertion of the IO muscles in the base of the PP for the IPJ and AA/AR coupling. The aim that the finger prototype contained anthropomorphic tendon structures is partially met, because while the distal part of the EA was implemented with the lateral bands, the insertions of the IO tendons into the EA, as well as the LU muscle, was left out.

8.1.2. Comparison with the state-of-the-art

The designed finger prototype has added to the existing range of anthropomorphic hands and fingers in developing a 3-dimensional system of humanoid joints and ligaments.

The main anthropomorphic aspect that has been left out in this finger prototype is the connection of the IO muscles to the EA as well as the lumbrical muscle. This has however been realised before by Faudzi et. al.[14]

Standing out in comparison to the current state-of-art robot fingers is the sole usage of strings in stead of sheets of material to emulate all the fibrous ligaments and tendon structures. The lateral stability of the extensor tendon of the finger prototype developed in this project was ensured by the fibres of the sagittal bands, which could move as individual strings over the MCP joint. For finger models with laser cut rubber/silicone EA, described by Xu and Todorov[47], and Tasi et. al[43], the EA was fixated to

finger segments with screws. Faudzi et. al [14], and Deshpande et. al[11], who developed an extensor mechanism with strands of dyneema, ensured that the extensor tendon would remain on the dorsal aspect of the MCP joint using guiding pulleys.
While both methods did laterally stabilise the extensor tendon, and the finger sweep motion and claw deformity in their experiments did show similarity with a the motion of a human finger, the stabilising mechanism of the sagittal bands was not shown in these fingers. Furthermore, these methods are not present in the human finger. And if we want to understand the mechanics of all the the tendons and ligaments in the human finger, and their interaction with each other, these structures need to be emulated into anthropomorphic fingers in the same way as found in the human finger. This is however dependant on the goals of the developers of novel anthropomorphic fingers and hands. The implementation of fibrous, inelastic structures such as the collateral ligaments and the sagittal bands, was a precise and tedious endeavour in this project. The main application of this finger prototype is to be a learning tool to study the biomechanical interactions of the different anatomical structures in the human finger. Hands and fingers which need to function as prosthesis or need to work in harsh environments have different requirements than this finger prototype.
Compared to the previous work performed in the hand biomechanics lab of Leijnse, this finger prototype featured, not only the anthropomorphic components of the previous finger models, but demonstrated also the complex collaboration of the different tendons, ligaments and other supporting structures to create a physical, finger model that can be manipulated in all its degrees of freedom, and including their constraints.

8.1.3. Future recommendations

The present thesis project developed a useful, physical model for understanding the biomechanics of the human finger, as well as the working mechanisms of their supporting ligaments. The results provide a basis for future generations of robot hands or further research in the biomechanics and anatomical restrictions of the hand.
The research performed in this thesis resulted in knowledge of the location of insertions for the tendon-ligament systems. Thus, future robot fingers would not need a high amount of unused perforations over a large surface of the phalanges for the construction of the supporting soft tissue structures. This could lead to a new, non-parametric design of the phalanges directly from 3D scanning methods. Future iterations could also work to reduce the scaling of the finger. A possible outcome would be a reduction of overall weight, material cost, and production time.
The developed finger in this thesis using a single hard material with FDM printing. But the development of future robot fingers do not need to be restricted to a single material or manufacturing method. A finger could be developed using multiple materials with different manufacturing techniques. While FDM printing is still a viable method for the production of shafts, the joint area's could be developed separately with higher resolution printing methods such as SLA. This could lead to smoother surfaces, but also possibilities of different materials, which could lower the friction in the joints even further.
The anthropomorphic finger developed in this thesis relied on levers to actuate the tendons. This demonstrated the movement possible in the finger by the combination of not only different muscles, but also external forces. Future work can explore the implementation of motors and anthropomorphic strategies to controller the robot finger. This research could lead to accurately and consistently determining the forces on the finger components during predetermined motion and pathologies

8.2. Conclusion

This study successfully developed an anthropomorphic finger with humanoid joint-ligament systems and tendon configurations. It has shown the possibility to design an anthropomorphic finger with individual strands of fibre emulating the tendon systems and ligament structures found in the human body.

The finger components consisted of a parametric finger geometry, with hard and soft tissue integrated into a single solid material. The components were 3D printed with FDM machines with PLA as material and water-soluble PVA as support material.

From experiments with different surface treatments to reduce friction in the joints, a composition of graphite powder with epoxy resin was found to reduce the increase of work due to friction by 64% and reduced the kinetic friction coefficient to 0.16. Which was a reduction of 44% compared to the non-coated control. This coating was added to the joint surface and the areas where tendons and ligaments contact the bone segments.

The joints of the finger were connected using dyneema strings strung through the perforations in the lateral faces of the finger segments, and configured such that the load on a string was transferred over the range of motion of the joint.

The ED, FDP, FDS and IO muscles were implemented for the actuation of the finger prototype with dyneema strings. For this finger, the DA was simplified to incorporate only the transverse fibres of the extensor apparatus and not the lateral bands originating from the interossei and lumbrical. Abduction/Adduction was performed by direct insertion of the IO muscles into the proximal phalanx. The finger prototype also demonstrated a stable and robust IPJ coupling, as well as demonstrating the AA/AR coupling of the MCP joint.

By disconnecting the IO tendons from their levers, the manifestation of intrinsic muscle weakness could be simulated, resulting in a claw deformity. Apart from demonstrating the importance of the intrinsic muscles to not only abduction/adduction, but also the extension of the finger, it demonstrated the functional anthropomorphism of the developed robot finger and its tendon-ligament structures. With the results from the verification experiments the aim of this thesis project can be concluded to be met.

The elements developed in this thesis form a basis for further research in the complex mechanics, relations, and dependencies of the human hand and in doing so, help to identify solutions to a wide range of pathologies in the hand.

Bibliography

[1] Anirudh Agarwal. *Hand Bones Anatomy*. Accessed: 2022-08-26. 2018. URL: https://www.knowyourbody.net/hand-bones.html.

[2] Maribel I Baker et al. "A review of polyvinyl alcohol and its uses in cartilage and orthopedic applications". In: *Journal of Biomedical Materials Research Part B: Applied Biomaterials* 100.5 (2012), pp. 1451–1457.

[3] Gh Baluta and M Coteata. "Precision microstepping system for bipolar stepper motor control". In: *International Aegean Conference on Electrical Machines and Power Electronics* (2007), pp. 291–296.

[4] Joseph T Belter and Aaron M Dollar. "Performance characteristics of anthropomorphic prosthetic hands". In: *2011 IEEE International Conference on Rehabilitation Robotics*. IEEE. 2011, pp. 1–7.

[5] Per Bendz. "The functional significance of the oblique retinacular ligament of Landsmeer. A review and new proposals". In: *Journal of Hand Surgery* 10.1 (1985), pp. 25–29.

[6] Shrikant J Chinchalkar, Chelsea A Barker, and Bobbi Owsley. "Relationship between juncturae tendinum and sagittal bands". In: *Journal of Hand and Microsurgery* 7.01 (2015), pp. 96–101.

[7] Shrikant J Chinchalkar and Shanley Pitts. "Dynamic assist splinting for attenuated sagittal bands in the rheumatoid hand". In: *Techniques in Hand & Upper Extremity Surgery* 10.4 (2006), pp. 206–211.

[8] Angi M. Christensen, Nicholas V. Passalacqua, and Eric J. Bartelink. "Chapter 12 - Individual Skeletal Variation". In: *Forensic Anthropology*. Ed. by Angi M. Christensen, Nicholas V. Passalacqua, and Eric J. Bartelink. San Diego: Academic Press, 2014, pp. 301–339. ISBN: 978-0-12-418671-2. DOI: 10.1016/B978-0-12-418671-2.00012-4.

[9] Jan C Cool. *Werktuigkundige systemen*. VSSD, Delft, 2006.

[10] Michel De Maeseneer et al. "Ultrasound anatomy of the fingers: flexor and extensor system with emphasis on variations and anatomical detail". In: *Journal of Ultrasonography* 20.81 (2020), pp. 122–128.

[11] Ashish D Deshpande et al. "Mechanisms of the anatomically correct testbed hand". In: *IEEE/ASME Transactions on mechatronics* 18.1 (2011), pp. 238–250.

[12] Jinzi Ding et al. "Properties, preparation, and application of tungsten disulfide: A review". In: *Journal of Physics D: Applied Physics* 54.17 (2021), p. 173002.

[13] Richard Drake et al. *Gray's anatomy for students*. Elsevier Health Sciences TW, 2005.

[14] Ahmad Athif Mohd Faudzi et al. "Index finger of a human-like robotic hand using thin soft muscles". In: *IEEE Robotics and Automation Letters* 3.1 (2017), pp. 92–99.

[15] Brian Feeny et al. "A historical review on dry friction and stick-slip phenomena". In: (1998).

[16] Michele Folgheraiter and Giuseppina Gini. "Blackfingers an artificial hand that copies human hand in structure, size, and function". In: *Proc. IEEE Humanoids* (2000), p. 4.

[17] Erika Nathalia Gama Melo, Oscar Fernando Aviles Sanchez, and Darlo Amaya Hurtado. "Anthropomorphic robotic hands: a review". In: *Ingeniera y desarrollo* 32.2 (2014), pp. 279–313.

[18] Zixun He et al. "A Design of Anthropomorphic Hand based on Human Finger Anatomy". In: *2020 International Symposium on Community-centric Systems (CcS)*. IEEE. 2020, pp. 1–5.

[19] Sabrina Jahn, Jasmine Seror, and Jacob Klein. "Lubrication of articular cartilage". In: *Annual review of biomedical engineering* 18 (2016), pp. 235–258.

[20] JM Landsmeer. "A report on the coordination of the interphalangeal joints of the human finger and its disturbances". In: *Acta morphologica neerlando-Scandinavica* 2.1 (1958), pp. 59–84.

[21] JMF Landsmeer. "The anatomy of the dorsal aponeurosis of the human finger and its functional significance". In: *The Anatomical Record* 104.1 (1949), pp. 31–44.

[22] Leijnse and Arne van Erum. “Bio-inspired control of anthropomorphic robotic fingers”. In: *Gent University* (2019).

[23] JNAL Leijnse. “Why the lumbrical muscle should not be bigger—a force model of the lumbrical in the unloaded human finger”. In: *Journal of Biomechanics* 30.11-12 (1997), pp. 1107–1114.

[24] JNAL Leijnse and JJ Kalker. “A two-dimensional kinematic model of the lumbrical in the human finger”. In: *Journal of biomechanics* 28.3 (1995), pp. 237–249.

[25] JNAL Leijnse, CW Spoor, and R Shatford. “The minimum number of muscles to control a chain of joints with and without tenodeses, arthrodeses, or braces—application to the human finger”. In: *Journal of biomechanics* 38.10 (2005), pp. 2028–2036.

[26] Joris Leijnse and Olivier Callewaert. “Ontwerp en bouw van een antropomorfe robotvinger0”. In: *Gent University* (2018).

[27] Leijnse, Quesada, and CW Spoor. “Kinematic evaluation of the finger’s interphalangeal joints coupling mechanism—variability, flexion–extension differences, triggers, locking swanneck deformities, anthropometric correlations”. In: *Journal of biomechanics* 43.12 (2010), pp. 2381–2393.

[28] Leijnse and CW Spoor. “Reverse engineering finger extensor apparatus morphology from measured coupled interphalangeal joint angle trajectories—a generic 2D kinematic model”. In: *Journal of biomechanics* 45.3 (2012), pp. 569–578.

[29] Xiubing Li et al. “Wear reduction mechanism of graphite and MoS2 in epoxy composites”. In: *Wear* 257.3-4 (2004), pp. 279–283. DOI: 10.1016/j.wear.2003.12.012.

[30] Rafael Neiman, Brian Maiocco, and Vincent F Deeney. “Ulnar nerve injury after closed forearm fractures in children”. In: *Journal of Pediatric Orthopaedics* 18.5 (1998), pp. 683–685.

[31] I Ohshio et al. “Reconstruction of the central slip by the transverse retinacular ligament for boutonniere deformity”. In: *Journal of Hand Surgery* 15.4 (1990), pp. 407–409.

[32] Jacob van Ooijen. “Anthropomorphism in tendon driven robotic fingers. Current mechanical limits and future steps: Literature study”. In: *TU Delft* (2022).

[33] Guoliang Pan et al. “Tribological behaviors of graphite/epoxy two-phase composite coatings”. In: *Tribology International* 43.8 (2010), pp. 1318–1325.

[34] Surbhi Panchal-Kildare and Kevin Malone. “Skeletal anatomy of the hand”. In: *Hand clinics* 29.4 (2013), pp. 459–471.

[35] Ha Q Pham and Maurice J Marks. “Epoxy resins”. In: *Ullmann’s Encyclopedia of Industrial Chemistry* (2000).

[36] Robert G Ross. *Paul W. Brand, Anne M. Hollister, Clinical Mechanics of the Hand, Mosby, St. Louis, Mo (1999)*. 2000.

[37] TW Scharf and SV Prasad. “Solid lubricants: a review”. In: *Journal of materials science* 48.2 (2013), pp. 511–531.

[38] RJ Schultz, A Storace, and S Krishnamurthy. “Metacarpophalangeal joint motion and the role of the collateral ligaments”. In: *International orthopaedics* 11.2 (1987), pp. 149–155.

[39] A. Schuurman et al. “The development and experimental validation of an anthropomorphic robot finger for future research in human finger control and functional pathology”. In: *BEP Technical University Delft* (2022).

[40] Timothy P Schweitzer and Ghazi M Rayan. “The terminal tendon of the digital extensor mechanism: Part I, anatomic study”. In: *The Journal of hand surgery* 29.5 (2004), pp. 898–902.

[41] Hao-Jie Song and Zhao-Zhu Zhang. “Investigation of the tribological properties of polyfluo wax/polyurethane composite coatings filled with several micro-particulates”. In: *Materials Science and Engineering: A* 424.1-2 (2006), pp. 340–346.

[42] Vis T., Luyt G. van der, and Sorgedrager S. “Anthropomorphic model of the MCP joint”. In: *BEP Technical University Delft* (2021).

[43] Benedek Jozsef Tasi, Miklós Koller, and Gyorgy Cserey. “Design of the anatomically correct, biomechatronic hand”. In: *arXiv preprint arXiv:1909.07966* (2019).

[44] Li Tian et al. “Design of a Highly Biomimetic and Fully-actuated Robotic Finger”. In: *2019 IEEE Symposium Series on Computational Intelligence (SSCI)*. IEEE. 2019, pp. 2382–2387.

[45] David D Wilkinson, Michael Vande Weghe, and Yoky Matsuoka. “An extensor mechanism for an anatomical robotic hand”. In: *2003 IEEE international conference on robotics and automation (Cat. No. 03CH37422)*. Vol. 1. IEEE. 2003, pp. 238–243.

[46] Na Wu et al. “Tribological properties of lubricating oil with micro/nano-scale WS2 particles”. In: *Journal of Experimental Nanoscience* 13.1 (2018), pp. 27–38.

[47] Zhe Xu and Emanuel Todorov. “Design of a highly biomimetic anthropomorphic robotic hand towards artificial limb regeneration”. In: *2016 IEEE International Conference on Robotics and Automation (ICRA)*. IEEE. 2016, pp. 3485–3492.

[48] Y Yamamoto, S Gondo, and N Tanaka. “Effect of graphite on friction and wear characteristics of molybdenum dithiocarbamate”. In: *Tribology Letters* 17.1 (2004), pp. 55–59.

[49] Christopher M Young and Ghazi M Rayan. “The sagittal band: anatomic and biomechanical study”. In: *The Journal of hand surgery* 25.6 (2000), pp. 1107–1113.

A

Friction test graphs and tables

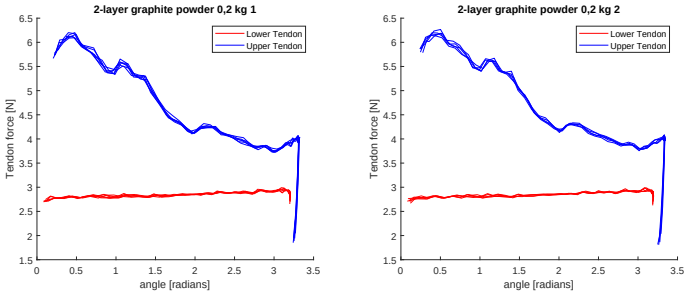

Figure A.1: Force on the tendons with respect to the angular displacement of the potentiometers

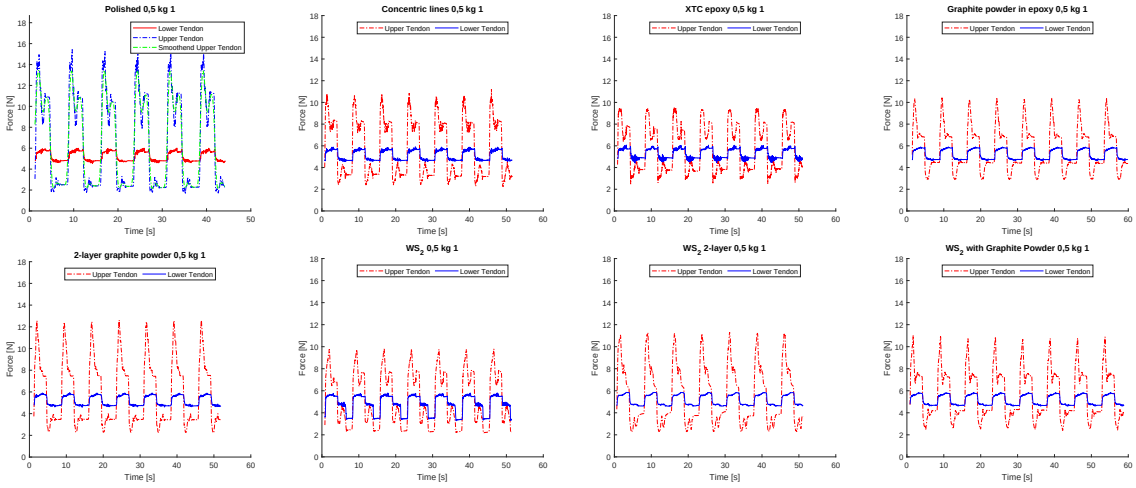

Figure A.2: Force on the tendons with respect to time on the first set of extension motions with a weight of 0.5 kg. The red lines indicate the upper tendon and the blue lines indicate the lower tendon

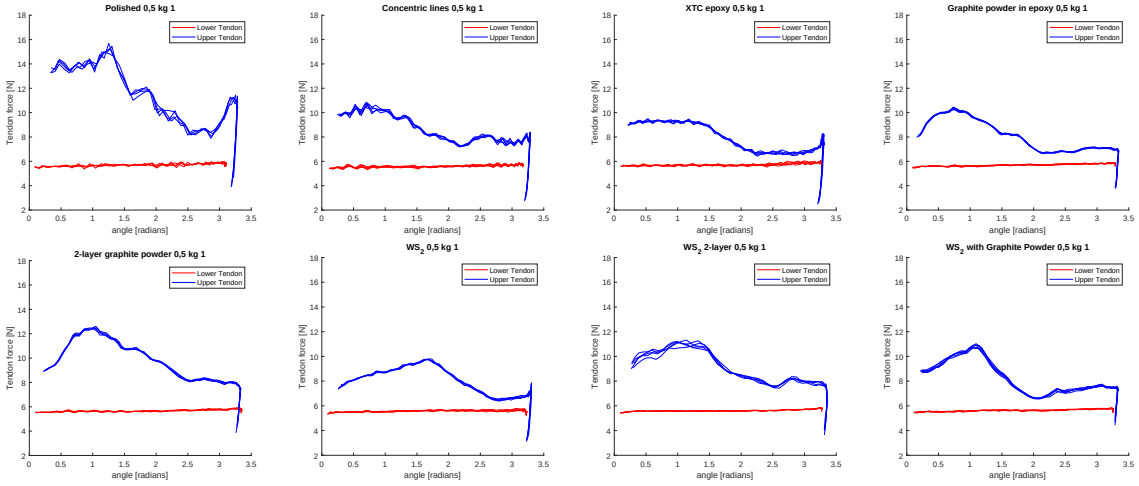

Figure A.3: Force to distance plot of the first set of extension motions with a weight of 0.5 kg attached to the flexor tendon. The red lines indicate the force on the lower tendon and the blue lines indicate the upper tendon.

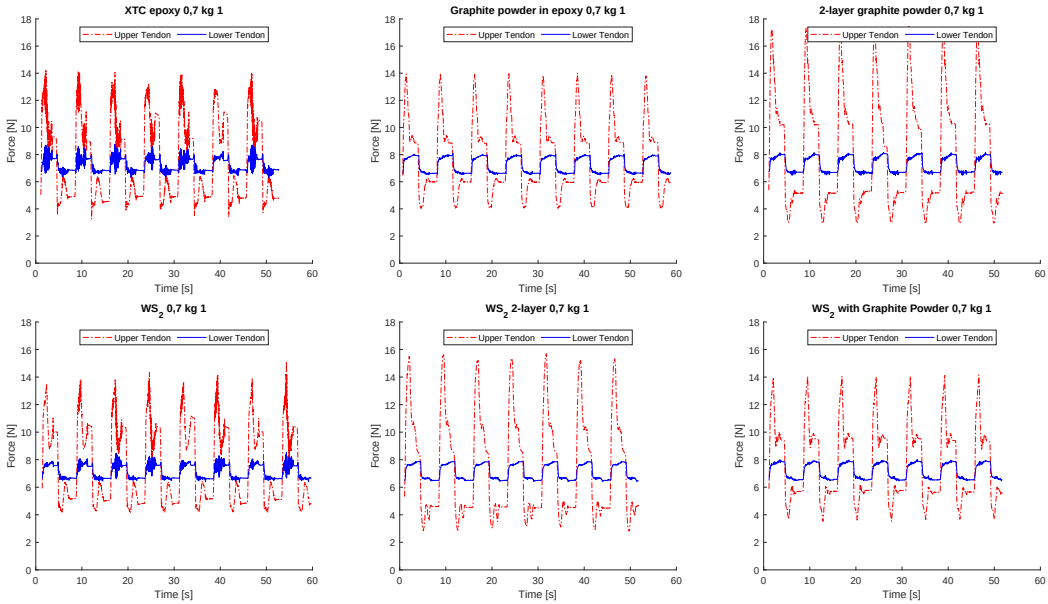

Figure A.4: Force on the tendons with respect to time on the first set of extension motions with a weight of 0.7 kg. The red lines indicate the upper tendon and the blue lines indicate the lower tendon

	Increase in work [J]					
Treatment	0.2 kg	0.3 kg	0.5 kg	0.7 kg	0.8 kg	1.0 kg
Tungsten disulphide wax	0.056338	0.073958	0.100237	0.128648	0.148501	
2-layer Tungsten disulphide	0.078165	0.102333	0.14869	0.190131	0.201263	0.163404
Tungsten disulphide wax with graphite powder	0.089213	0.103596	0.116841	0.133368	0.132558	0.159048
XTC-epoxy	0.048129	0.064533	0.091421	0.125201	0.136789	
Polished	0.153673	0.198094	0.265884			
Concentric lines	0.064249	0.091521	0.134126			
Graphite-epoxy	0.063243	0.08014	0.094228	0.134554	0.145774	0.167089
2-layer graphite powder	0.085431	0.119376	0.181104	0.238531		

Table A.1: Increase in work for each treatment at a given load. Left column shows the different treatments and the top row shows the load in kg. The added work for extension is given in Jouls [J]

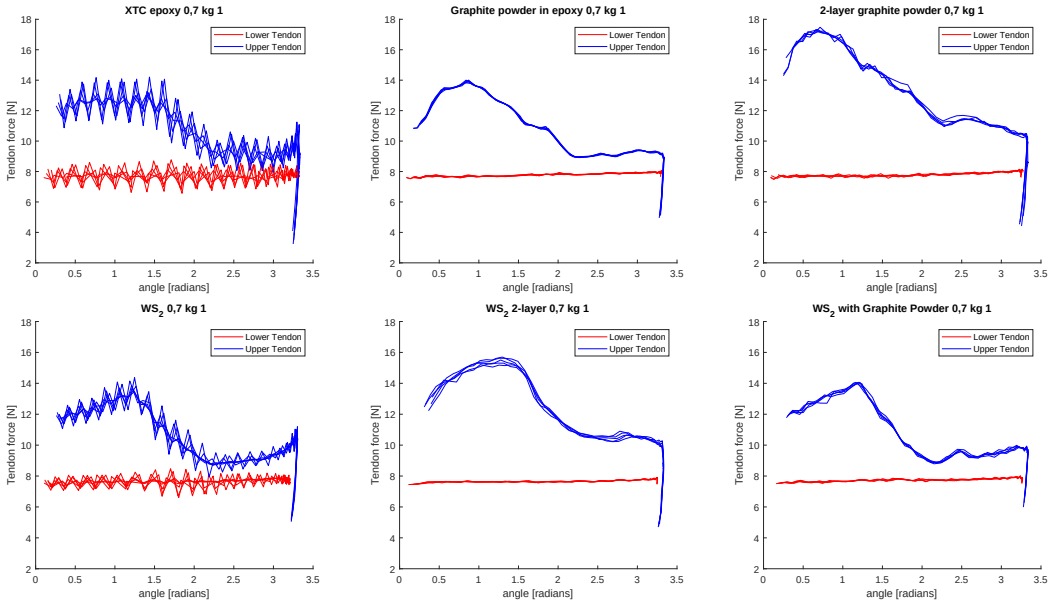

Figure A.5: Force on the tendons with respect to the angular displacement on the first set of extension motions with a weight of 0.7 kg. The red lines indicate the lower tendon and the blue lines indicate the upper tendon. The jagged lines with the XTC epoxy and WS_2 joint indicate a jolting motion due to a big difference in static and dynamic friction coefficients.

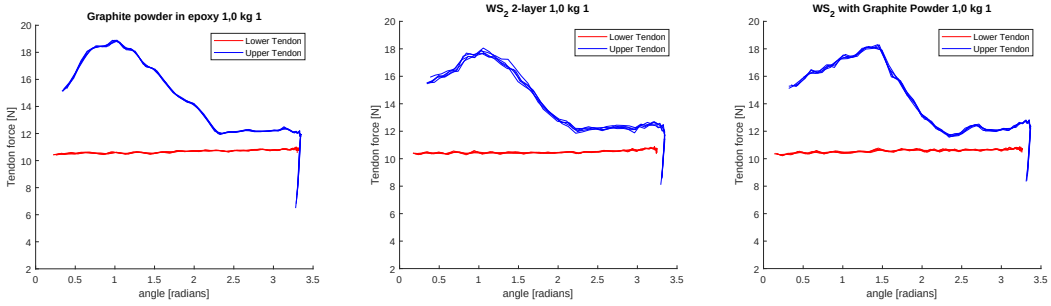

Figure A.6: Force on the tendons with respect to the angular displacement of the first set of extensions at 1.0 kg. The red lines indicate the lower tendon and the blue lines indicate the upper tendon.

Relative addition of work [%]

Treatment	0.2 kg	0.3 kg	0.5 kg	0.7 kg	0.8 kg	1.0 kg
Tungsten disulphide wax	43.20582	41.3284	38.46566	36.87605	37.64482	
2-layer Tungsten disulphide	59.34886	56.63658	55.83452	54.05925	51.1351	34.05896
Tungsten disulphide wax with graphite powder	68.45971	57.11659	44.37387	37.48802	34.18887	33.00846
XTC-epoxy	36.6085	35.49044	33.82243	34.60438	34.14868	
Polished	123.5088	115.7316	105.6349			
Concentric lines	50.95777	52.85683	52.63627			
Graphite-epoxy	48.05595	44.01162	41.63588	36.49533	35.15193	33.94232
2-layer graphite powder	64.98533	65.2236	66.04038	65.948		

Table A.2: Added work on the upper tendon relative to the work calculated at the lower tendon.

B

Literature study

Anthropomorphism in tendon driven robotic fingers. Current mechanical limits and future steps

Jacob van Ooijen
4229614

June 20, 2022

Abstract

Background: Current Anthropomorphic robot fingers are designed with the focus on the appearance and resulting kinematics, which should resemble that of a human finger. Despite advances made in robot hands and fingers, concessions and simplifications need to be made for the development of these fingers due to the complexity of the kinematic and dynamic mechanisms in the human finger.
Objective: Review the peer-reviewed literature on anthropomorphic robot fingers and hands to determine the simplifications of current state-of-the-art robots compared to the human finger.
Methods: Two electronic databases were searched using a Boolean combination of relevant keywords. Articles in the English language relevant to the objective were selected.
Results: In all, 27 papers were included in the review. The joint connection is mostly done with pins and rollers due to the friction of the joints. Fingers that that did use humanoid joints relied on elastic, isotropic ligaments. Publications which implemented a structure similar to the dorsal aponeurosis used either laser cut sheets of rubber, or single strands of fibrous material.
Conclusion: Current anthropomorphic robot fingers are mostly simplified in the structure and material of the joint connecting ligaments and the dorsal aponeurosis. This is due to the complex layout of the collateral ligaments and the dorsal aponeurosis, but also due to the high friction of robot fingers with humanoid joints. The development of full fibrous collateral ligaments and dorsal aponeuroses, together with developing methods of reducing friction in ligamentous joints, could result in a better representation of the human finger and would probably answer questions about the working mechanism of the dorsal aponeurosis.

List of Acronyms

Acronyms

DA Dorsal Aponeurosis.

DIP Distal Interphalangeal.

DOF Degrees of Freedom.

ED Extensor digitorum.

FDP Flexor digitorum Profundus.

FDS Flexor digitorum Sublimis.

IO Interosseus muscles.

LU Lumbrical muscles.

MCP Metacarpal-phalangeal.

PIP Proximal Interphalangeal.

1 Background

1.1 Introduction

The hand is one of the most functional limbs of the human body and is used in a wide variety of daily tasks, ranging from high load carrying such as rock climbing and boxing to delicate movement such as writing or playing an instrument. Over the last few decades, great steps have been made in the development of prosthetic and robotic hands, which move towards more dextrous and realistic devices. An important part of the hand is the finger, which allows for grasping and manipulation. In the past, several models of the human finger have been developed. Either to illustrate the biomechanics of the finger for education purposes, or as a means of developing prosthetics. Belter and Dollar[1] reviewed the performance characteristics of 5 commercial robotic hands and 11 research hands. Comparing their degrees of freedom, actuation method and joint coupling method. Gama et. al[2] tried to quantify the anthropomorphism in robotic hands based on their kinematics and size in comparison to a human hand. Kashef and Amini[3] investigated the grasp and physical characteristics of artificial fingers in linkage-driven hand prosthetics. Current reviews of fingers used in anthropomorphic robot hands focus on the appearance and the resulting kinematics in comparison to the human hand. But the functional mechanisms that facilitate anthropomorphic motion are rarely discussed.

1.2 Problem statement

The term Anthropomorphism refers to the capability of a device to mimic the human hand in general aspects, such as shape, size, consistency, colour, temperature and aesthetic factors.[2] But also in function, kinematics and workspace of the phalanges.[4]

Despite the wide research field that has been developed and exposed in the literature, as well as the advances made in design, control and sensory, there are still issues to be solved or need improvement on robotic hands. Because the human finger is a complex system of tendons, ligaments and kinematic couplings, concession in the design have to be made for the production of robotic fingers.

1.3 Objective

The objective of this literature research is to review the mechanical designs of current robotic fingers and compare them to the functional anatomy of the human finger to identify their limitations, to describe the inaccuracies of their functional mechanisms and the future steps towards a fully anthropomorphic finger.

1.4 Research question

Of current anthropomorphic/biomimetic fingers, what is the level of anthropomorphism of current state-of-the-art tendon-driven robot fingers, and which steps can be made towards a fully anthropomorphic finger? This study will focus on the following aspects:

- Geometry: *How do the shapes and dimensions of current robot fingers match with the properties of the human finger*
- Joint connection: *Which methods are used to connect the phalanges and how do they compare to human finger joint connections.*
- Actuation method: *How the tendons of current robot fingers are configured compared to human fingers. Specifically, the extension and abduction through the dorsal aponeurosis*
- Range of motion: *How the range of motion is governed in robot fingers in comparison to the human finger*

1.5 Functional anatomy of the human finger

1.5.1 Geometry and joint connection

The human finger has 3 joints, the metacarpal-phalangeal MCP joint, and the Proximal Interphalangeal (PIP) and Distal Interphalangeal (DIP) joints. The PIP and DIP joints have one degree of freedom (DOF), flexion-extension, while the MCP joint has two degrees of freedom (flexion-extension, abduction-adduction). This results in four kinematic degrees of freedom. The head of the MCP joint has a slightly oval shape along the sagittal plane and revolute along the transverse plane.

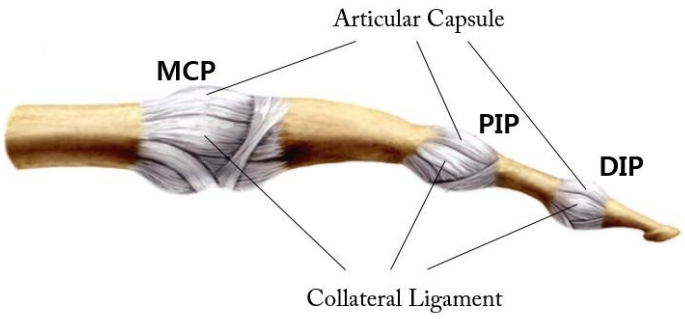

Figure 1: Schematic of the human finger with its ligamentous connections.[5]

The phalanges are connected with a tight band of passive ligaments called the collateral ligaments. These ligaments primarily provide the lateral sta-

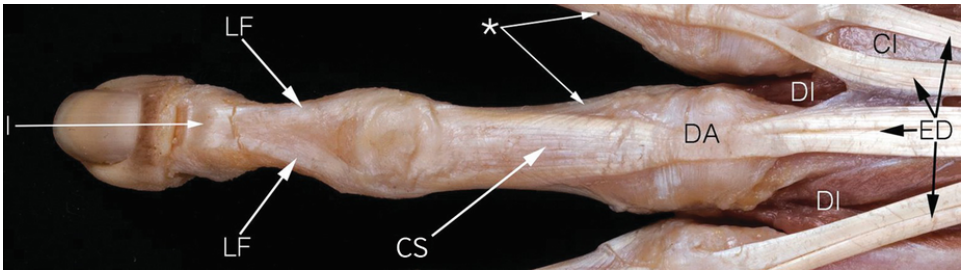

Figure 2: Dorsal aponeurosis of the middle finger. LF: The lateral fibres, CS: Central slip, ED: Extensor digitorum tendon, I: Insertion of the extensor hood in the distal phalanx, DI: Dorsal interosseous muscles, CI: Connexus intertendinei. [10]

bility of the joint in the finger.[6] These structures consist of small but stiff fibres loosely connected together with connective tissue. This results in an anisotropic structure with great tensile strength parallel to the fibres, but little strength perpendicular to the fibres.

1.5.2 Actuation and kinematics

The kinematics and dynamics of the human finger are tendon-driven. Meaning that the motion is enabled by a series of tendons which mostly function in tension by lengthening or shortening of the muscle which is attached to the corresponding tendon.[7] These muscles are the Flexor Digitorum Profundus (FDP), Flexor Digitorum Sublimis (FDS), Extensor Digitorum (ED), two Interosseus (IO) muscles and two Lumbrical (LU). However, the lumbrical does not add basic controllability to the finger (it may improve control in certain movements). The lumbrical is redundant with the radial interosseus [8] and the finger can function in basic control without the lumbricals.[9] The extensor tendon travels along the dorsum of the finger, inserting into the proximal phalanx and the distal phalanx through a fanning out into the Dorsal Aponeurosis (DA). The DA is a complex tendon sheet with fibres from the IO, LU and ED joining together from different angles. The layout of these fibres results in the flexion, abduction, and adduction of the MCP joint, and the coupled extension of the PIP and DIP joints.

2 Method

2.1 Search query

In December 2021 and January 2022, a literature search was performed through a search of Scopus, Web of Science using the following boolean combination of the keywords: (Anthropomorphic OR Biomimetic) AND (Finger) AND (Tendon OR Tendons). Search results were limited to the English language and the subject area was set to be in engineering and no time restrictions were imposed.

2.2 Selection criteria

Inclusion criteria
The articles focusing on the mechanical design of the finger mechanism in (1) robotic hands, (2) prosthetics and (3) research models were included in the review process.

Criteria application
The selection criteria were applied to the titles and abstracts of the articles. In some articles, the specific design of the finger was not clearly stated in the title or the abstract. In these cases, the main article was scanned to apply the selection criteria.

After the initial application of the selection criteria, the main text of the articles was studied for referenced articles which were not found in the search results. The selection criteria was then applied to their titles and abstracts.

3 Results

3.1 Search results

Execution of the search query resulted in 228 articles distributed over two databases. Removal of the overlap between databases resulted in 140 unique articles. Application of the selection criteria further decreased the number of relevant articles to 34. After scanning the articles, the number of relevant articles was further reduced to 24 articles. The scanning of the articles. The referenced articles of these 24 articles were examined similarly. This resulted in 3 more articles. In total, 27 articles were selected for inclusion in the review. Of these articles, 16 robotic fingers were made as part of an entire hand, while 11 were standalone fingers.

3.2 Geometry and kinematics

For most robotic fingers, the geometry of the robotic fingers could be described as either a 3D model of the human finger or a 3-bar linkage system. The geometries of the fingers based on a 3D model of the human finger were mostly acquired using a 3D scanner of human finger bones. The geometries of the 3-bar linkage fingers were based on the general length and width of a human finger. Kontoudis et al. [11] described their robot finger as a one-piece compliant mechanism with flexible hinges at the joints. Folgerhaiter and Gini [12] implemented a parametric design of the finger bones. Using straight bars and simple cup and socket joints to represent the phalanges.

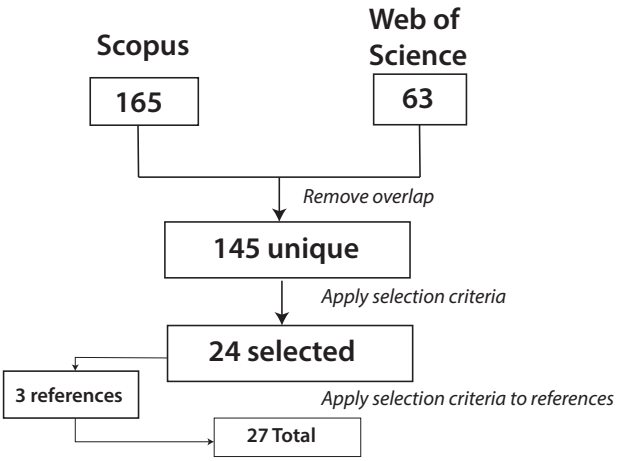

Figure 3: Search method flow chart

Joint connection

The most straightforward method of connecting the joints in a mechanism is the use of pins and roller bearings. This method of connection is used mostly due to the robustness and simplicity of such a system compared to a fibrous ligament system. From the researched articles, six robotic fingers [13][14][15][12][16][17] implemented some form of ligamentous connection of the finger joints. Either by silicon rubber ligaments, elastic bands or crocheted ligaments.

Although multiple articles describe a ligamentous joint connection, most fingers use an isotropic and highly elastic material such as (silicon) rubber with a Young's modulus ranging between 0.001 and 0.05 GPa. In the human finger, the ligaments that connect the phalanges are anisotropic fibrous bands with a much higher Young's modulus between 1.0 and 2.0 GPa.[18] Xu and Todorov[14] implement a fibrous connection with crocheted ligaments made of stiffer strings. However, in conjunction with these ligaments, laser cut rubber sheets were used to support the joint. Suggesting that the joint might not be stable with the ligamentous element only.

Finger kinematics

The finger kinematics were evaluated according to the following characteristics:

1. Degrees of freedom
   The sum of all motions that the finger can perform without considering

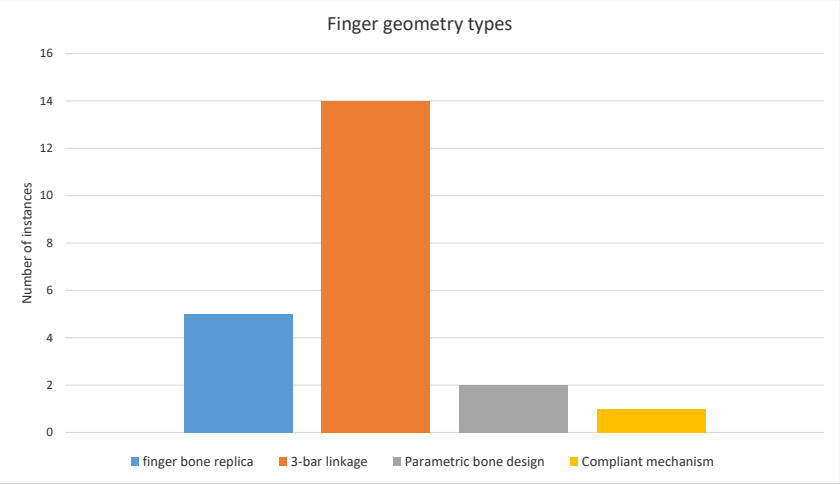

Figure 4: Types of finger bone geometries

actuation of tendons

2. Range of motion
   An evaluation of the constraining mechanisms for the motion of each finger joint. Specifically the extension

Out of the reviewed articles, 15 out of 27 fingers had 4 degrees of freedom, similar to the human finger. Where the MCP joint has two DOF flexion-extension and abduction-adduction and the PIP and DIP joints both have one DOF for flexion-extension. From these 15 fingers, only 7 described methods for limiting finger extension to humanoid ranges of motion. Mostly by a mechanical block at the dorsum of the phalanges preventing the joint from moving further. He et. al, 2020[19], Tasi et. al, 2019[17] and Faudzi et. all, 2017[16] used a rubber sheet attached volar to the PIP and DIP joints to prevent hyperextension. Xu and Todorov, 2016 [14] used crocheted ligament strings to simulate the volar plates.

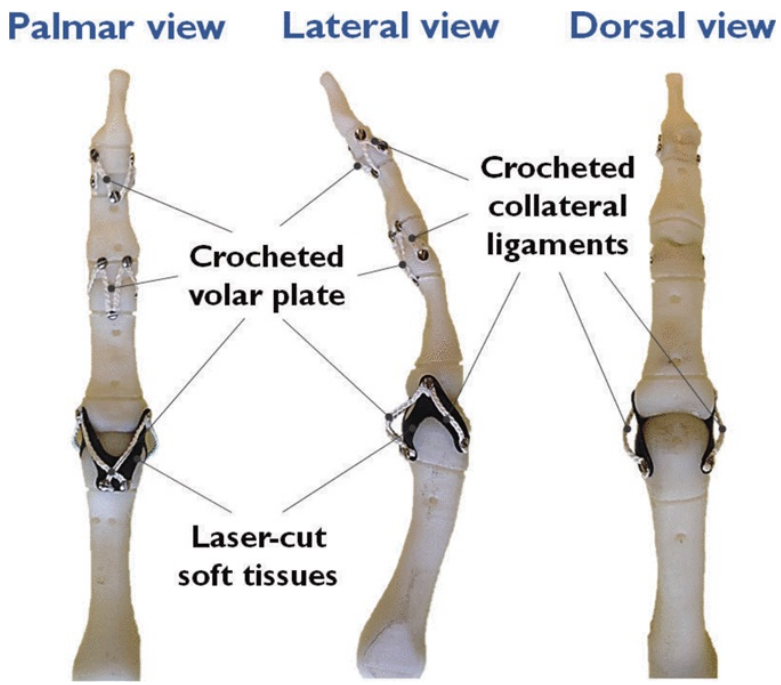

Figure 5: Connecting phalanges using crocheted collateral ligaments.[14]

3.3 Tendon configuration

Extensor mechanism

In the reviewed literature, 7 out of 27 had an extensor similar to the human finger.

Faudzi et. al. [16] developed their extensor mechanism using strands of dyneema which goes to a joint. Two strands of dyneema are fixed at the base of the DP. Wilkinson et. al [20] and Deshpande et. al.[21] applied the same method but used nylon threads instead of dyneema. He et. al.[19], Xu and Todorov[14], and Tasi et. al [17] developed a laser cut rubber sheet with two wider strands originating from the central fibre at the middle phalanx to the distal phalanx to couple PIP-DIP extension.

Abductor-Adductor configuration

From the reviewed literature, the abduction-adduction of the MCP joint was performed mostly by an antagonist tendon pair. Kontoudis et al. [11] used a torsional at the MCP joint to restore abduction to a neutral position. Mifsud and Grech[23] used a servo motor in the MCP joint to control lateral motion in the joint.

Finger designs that had some form of the extensor mechanism also incorporated the tendons for abduction into this mechanism.[17][21][16][20] This

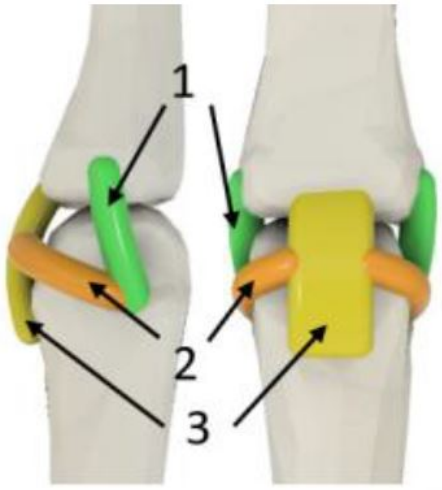

Figure 6: Ligament system of the finger designed by Tasi et. al.[17] 1: Proper collateral ligaments connecting the phalanges directly. 2: Accessory collateral ligaments constraining the motion of the volar plate. 3: Volar plate limiting the extension of the phalanges

is similar to the human finger and thus, the abduction of these fingers has a high level of anthropomorphism. However, insertions into the proximal phalanx of the dorsal interossei are missing in all designs.

4 Discussion

The term anthropomorphism is widely used in the literature to encompass different forms of similarity to humans. This broadens the definition of anthropomorphism. Most of the reviewed literature do not make a distinction between aesthetic and functional anthropomorphism. During the literature search, this resulted in articles describing fingers which had similar appearance of human fingers, but lacked humanoid functionality. In this the anthropomorphism of the fingers lied the general shape and size of the model. From a biomechanical viewpoint, anthropomorphism is better described by the mechanical aspects of a system such as their linkage, kinematics, and actuation.

In mechanically anthropomorphic fingers, big differences arose in which aspect is considered anthropomorphic. Fingers with linkage-driven geometry relied heavily on non-humanoid methods of joint connection and constraining mechanisms, such as pins and rollers or mechanical extension blocks. In this the anthropomorphism of the fingers lied the general shape and size of the model and often the tendon configuration. Articles using finger bone replicas often also incorporated other humanoid systems in the finger, such as a DA and ligamentous joint connections. While these fingers have a higher degree of similarity with human biomechanics, non-humanoid structures were

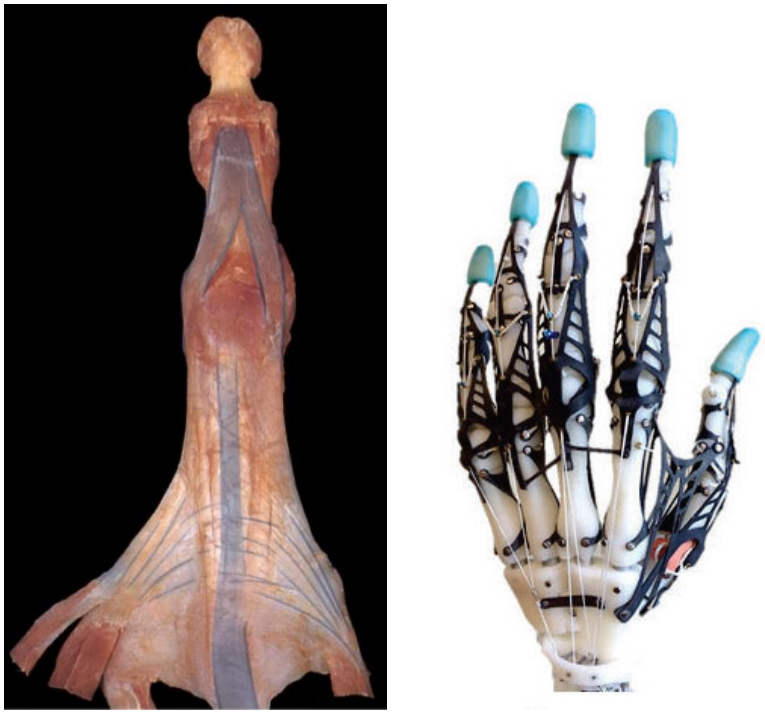

Figure 7: *Left*: Anatomic specimen of the extensor apparatus of the index finger[22]. The central extensor tendon, lateral bands and the conjunction of the intrinsic muscles and the extensor tendon are highlighted in blue. *Right*: Extensor mechanisms designed by Xu and Todorov [14].

necessary for the stability and motion. On the other hand, though a fully anthropomorphic robot finger has not yet been developed, current state-of-the-art robot fingers have been able to exhibit humanoid motion and dynamics similar to the human finger. It is therefore necessary to find out which components of the finger are the most needed in a robotic finger to perform the movements of the human hand.

5 Conclusions

Developers of anthropomorphic fingers have made great steps into realizing fingers with human-like anatomy and geometry by replicating the fingers bones with the use of 3D scanning. However, a number of anatomical structures and tendon configurations of the human finger are simplified or left out entirely for the sake of simplicity or robustness.

In the current literature, the joint connection is often performed by pins and rollers due to their robustness or low friction. One of the main bottlenecks for current state of the art anthropomorphic fingers lies in realizing a low-friction joint surface comparable to the friction characteristics of human cartilage and synovial fluid. Joint connections which did rely on ligamentous fibres relied

on elastic materials to ensure joint stability and had comparatively higher friction in the joints. In future research, this challenge needs to be faced to further the development of new anthropomorphic fingers.

Another simplification in comparison to the human finger is the design of the DA. Though the coupling of the extension of the PIP and DIP joints was found in state-of-the-art robot fingers, the fibres of the DA were often simplified as single strands of tendon instead of a continuous fibrous sheet, or it was made from a single laser cut piece of isotropic material. Increasing the number of fibres in the DA could result in a better representation of the human anatomy, and would probably answer questions about the working mechanism of the DA.

References

1. Belter JT and Dollar AM. Performance characteristics of anthropomorphic prosthetic hands. *2011 IEEE International Conference on Rehabilitation Robotics*. IEEE. 2011 :1–7
2. Gama Melo EN, Aviles Sanchez OF, and Amaya Hurtado D. Anthropomorphic robotic hands: a review. Ingeniera y desarrollo 2014; 32:279–313
3. Kashef SR, Amini S, and Akbarzadeh A. Robotic hand: A review on linkage-driven finger mechanisms of prosthetic hands and evaluation of the performance criteria. Mechanism and Machine Theory 2020; 145:103677
4. Liarokapis MV, Artemiadis PK, and Kyriakopoulos KJ. Quantifying anthropomorphism of robot hands. *2013 IEEE International Conference on Robotics and Automation*. IEEE. 2013 :2041–6
5. Lee G and Choi Y. Bio-inspired tendon-driven finger design with isomorphic ligamentous joint. IEEE Access 2020; 8:18240–51
6. Minamikawa Y, Horii E, Amadio P, Cooney W, Linscheid R, and An K. Stability and constraint of the proximal interphalangeal joint. The Journal of hand surgery 1993; 18:198–204
7. Sobotta J, Putz R, Pabst R, Putz R, and Bedoui S. Sobotta: atlas of human anatomy. Elsevier, Urban & Fischer, 2006
8. Leijnse J. Why the lumbrical muscle should not be bigger—a force model of the lumbrical in the unloaded human finger. Journal of Biomechanics 1997; 30:1107–14
9. Leijnse J, Spoor C, and Shatford R. The minimum number of muscles to control a chain of joints with and without tenodeses, arthrodeses, or braces—application to the human finger. Journal of biomechanics 2005; 38:2028–36
10. Baksa G, Mandl P, Benis S, Patonay L, Balint GP, and Balint PV. Gross Anatomy of the Human Hand. *Ultrasonography of the Hand in Rheumatology*. Springer, 2018 :15–41
11. Kontoudis GP, Liarokapis M, and Vamvoudakis KG. A compliant, underactuated finger for anthropomorphic hands. *2019 IEEE 16th International Conference on Rehabilitation Robotics (ICORR)*. IEEE. 2019 :682–8
12. Folgheraiter M and Gini G. Blackfingers an artificial hand that copies human hand in structure, size, and function. Proc. IEEE Humanoids 2000 :4
13. Xu Z, Kumar V, Matsuoka Y, and Todorov E. Design of an anthropomorphic robotic finger system with biomimetic artificial joints. *2012 4th IEEE RAS & EMBS International Conference on Biomedical Robotics and Biomechatronics (BioRob)*. IEEE. 2012 :568–74

14. Xu Z and Todorov E. Design of a highly biomimetic anthropomorphic robotic hand towards artificial limb regeneration. *2016 IEEE International Conference on Robotics and Automation (ICRA)*. IEEE. 2016 :3485–92
15. Tian L, Thalmann NM, Zheng J, and Thalmann D. Design of a Highly Biomimetic and Fully-actuated Robotic Finger. *2019 IEEE Symposium Series on Computational Intelligence (SSCI)*. IEEE. 2019 :2382–7
16. Faudzi AAM, Ooga J, Goto T, Takeichi M, and Suzumori K. Index finger of a human-like robotic hand using thin soft muscles. IEEE Robotics and Automation Letters 2017; 3:92–9
17. Tasi BJ, Koller M, and Cserey G. Design of the anatomically correct, biomechatronic hand. arXiv preprint arXiv:1909.07966 2019
18. Martin RB, Burr DB, Sharkey NA, and Fyhrie DP. Mechanical properties of ligament and tendon. *Skeletal tissue mechanics*. Springer, 2015 :175–225
19. He Z, Yurievich RR, Shimizu S, Fukuda M, Kang Y, and Shin D. A Design of Anthropomorphic Hand based on Human Finger Anatomy. *2020 International Symposium on Community-centric Systems (CcS)*. IEEE. 2020 :1–5
20. Wilkinson DD, Weghe MV, and Matsuoka Y. An extensor mechanism for an anatomical robotic hand. *2003 IEEE international conference on robotics and automation (Cat. No. 03CH37422)*. Vol. 1. IEEE. 2003 :238–43
21. Deshpande AD, Xu Z, Weghe MJV, Brown BH, Ko J, Chang LY, Wilkinson DD, Bidic SM, and Matsuoka Y. Mechanisms of the anatomically correct testbed hand. IEEE/ASME Transactions on mechatronics 2011; 18:238–50
22. Srivastava S. Anatomy of the Upper Limb: Extensor Expansion. Stanford Center for Health Education. 2019. Available from: https://www.youtube.com/watch?v=G0v_wX8Ms4Y
23. Mifsud N, Grech A, Saliba MA, and Fabri SG. Development of an anthropomorphic robot finger: mechanical and kinematic aspects. 2006
24. Shirafuji S, Ikemoto S, and Hosoda K. Design of an anthropomorphic tendon-driven robotic finger. *2012 IEEE International conference on robotics and biomimetics (ROBIO)*. IEEE. 2012 :372–7
25. Jung SY, Kang SK, Bae JH, and Moon IH. Design of biomimetic hand prosthesis with tendon-driven five fingers. Journal of Biomedical Engineering Research 2009; 30:205–12
26. Bundhoo V and Park EJ. Design of an artificial muscle actuated finger towards biomimetic prosthetic hands. *ICAR'05. Proceedings., 12th International Conference on Advanced Robotics, 2005.* IEEE. 2005 :368–75

27. Shirafuji S, Ikemoto S, and Hosoda K. Development of a tendon-driven robotic finger for an anthropomorphic robotic hand. The International Journal of Robotics Research 2014; 33:677–93
28. Dong Y and Zhang W. A Novel Coupled and Self-adaptive Anthropomorphic Robot Finger with a Dual-oblique-Belt Mechanism. *2019 IEEE 4th International Conference on Advanced Robotics and Mechatronics (ICARM)*. IEEE. 2019 :732–7
29. Yanagisawa K, Shirafuji S, Ikemoto S, and Hosoda K. Anthropomorphic finger mechanism with a nonelastic branching tendon. *Intelligent Autonomous Systems 13*. Springer, 2016 :1159–71
30. Zhang Z, Han T, Pan J, and Wang Z. Design of anthropomorphic fingers with biomimetic actuation mechanism. IEEE Robotics and Automation Letters 2019; 4:3465–72
31. Rothling F, Haschke R, Steil JJ, and Ritter H. Platform portable anthropomorphic grasping with the bielefeld 20-DOF shadow and 9-DOF TUM hand. *2007 IEEE/RSJ International Conference on Intelligent Robots and Systems*. IEEE. 2007 :2951–6
32. Grebenstein M, Chalon M, Hirzinger G, and Siegwart R. Antagonistically driven finger design for the anthropomorphic DLR hand arm system. *2010 10th IEEE-RAS International Conference on Humanoid Robots*. IEEE. 2010 :609–16
33. Lotti F, Tiezzi P, Vassura G, Biagiotti L, Palli G, and Melchiorri C. Development of UB hand 3: Early results. *Proceedings of the 2005 IEEE International Conference on Robotics and Automation*. IEEE. 2005 :4488–93
34. Dalley SA, Wiste TE, Withrow TJ, and Goldfarb M. Design of a multifunctional anthropomorphic prosthetic hand with extrinsic actuation. IEEE/ASME transactions on mechatronics 2009; 14:699–706
35. Kurita Y, Ono Y, Ikeda A, and Ogasawara T. Human-sized anthropomorphic robot hand with detachable mechanism at the wrist. Mechanism and Machine Theory 2011; 46:53–66
36. Oung S, Pohl B, and Hofmann U. Preliminary design of a tendon-based anthropomorphic robotic hand. Biomedical Engineering/Biomedizinische Technik 2012; 57:934–7
37. Rodić A, Miloradović B, Popić S, Spasojević S, and Karan B. Development of modular compliant anthropomorphic robot hand. *New Trends in Medical and Service Robots*. Springer, 2014 :205–19
38. Gong D, Hao L, Yu J, and Zuo G. Bionic design of a dexterous anthropomorphic hand actuated by antagonistic PAMs. *2020 IEEE International Conference on Real-time Computing and Robotics (RCAR)*. IEEE. 2020 :493–8
39. Che D and Zhang W. A humanoid robot upper limb system with anthropomorphic robot hand: GCUA hand II. *International Conference on Social Robotics*. Springer. 2010 :182–91

A List of hands

Table 1: Geometric and kinematic properties of the fingers found in the literature

Article (authors, year)	Geometry	Degrees of freedom	Joint connection
Xu, Z; Kumar, et. al, 2012[13]	finger bone replica	4 degrees of freedom	crochetted ligaments with silicon rubber sleeve
Shirafuji, S et. al., 2012 [24]	3-bar linkage	3 degrees of freedom	Pins and rollers
Jung, SY et. al., 2008 [25]	3-bar linkage	2 degrees of freedom	Pins and rollers
Bundhoo, V and Park, EJ, 2005[26]	3-bar linkage	4 degrees of freedom	Pins and rollers
Tian, L et. al.,2019[15]	finger bone replica	4 degrees of freedom	Silicon rubber ligaments
Shirafuji S. et. al., 2014[27]	3-bar linkage	3 degrees of freedom	Pins and rollers
Dong Y. and Zhang W., 2019[28]	3-bar linkage	3 degrees of freedom	Pins and rollers
Kontoudis G.P. et. al.,, 2019[11]	Compliant mechanism	4 degrees of freedom	Compliant flexures
Yanagisawa K. et. al., 2016[29]	3-bar linkage	2 degrees of freedom	Pins and rollers
He Z. et. al., 2020[19]	finger bone replica	3 degrees of freedom	Pins and rollers
Zhang Z. et. al., 2019[30]	3-bar linkage	4 degrees of freedom	Pins and rollers
Mifsud N. et. al., 2006[23]	3-bar linkage	4 degrees of freedom	Pins and rollers
Rothling, F. et. al. 2007[31]	3-bar linkage	4 degrees of freedom	Pins and rollers
Grebenstein, M. et. al., 2010[32]	3-bar linkage	4 degrees of freedom	Pins and rollers
Wilkinson, D. et. al., 2003[20]	3-bar linkage	4 degrees of freedom	Pins and rollers
Deshpande, A. et. al., 2011[21]	finger bone replica	4 degrees of freedom	Pins and rollers
Lotti, F. et. al., 2005[33]	3-bar linkage	3 degrees of freedom	Pins and rollers
Dalley, S. et. al., 2009[34]	3-bar linkage	3 degrees of freedom	Pins and rollers
Xu and Todorov, 2016[14]	finger bone replica	3 degrees of freedom	crochetted ligaments
Folgheraiter and Gini, 2000[12]	Parametric bone design	4 degrees of freedom	elastic bands
Kurita, Y. et. al., 2011[35]	3-bar linkage	4 degrees of freedom	Pins and rollers
Oung, S. et. al, 2012[36]	3-bar linkage	4 degrees of freedom	Pins and rollers
Rodic, A et. al., 2014[37]	4-bar linkage	4 degrees of freedom	Pins and rollers
Gong, D et. al., 2020[38]	3-bar linkage	3 degrees of freedom	Pins and rollers
Faudzi, A. A. M. et. al., 2017[16]	finger bone replica	4 degrees of freedom	Silicon rubber ligaments
Tasi, B.J. et. al., 2019[17]	finger bone replica	4 degrees of freedom	Silicon rubber ligaments
Che and Zhang, 2010[39]	3-bar linkage	3 degrees of freedom	Pins and rollers

Article (authors, year)	Extensor configuration	Extensor constraining mechanisms	Flexor configuration	Abductor configuration
Xu, Z; Kumar, et. al, 2012[13]	Extensor tendon at PP. PIP-DIP coupling with pulley system	Crocheted volar plate	FDP and FDS	Antagonist tendons
Shirafuji, S et. al., 2012[24]	Extensor tendon at DP. PIP-DIP coupling with pulley system	None	Flexor insertion at DP	None
Jung, SY et. al., 2008[25]	Restoration springs	Mechanical block in extension	Coupled Distal-middle phalanx and PP	None
Bundhoo, V and Park, EJ, 2005[26]	Extensor tendons at PP and MP. PIP-DIP coupling with pulley	None	Flexor insetion at PP and MCP	Antagonist tendons
Tian, L et. al.,2019[15]	Extensor tendons at PP,MP and DP	None	Flexor insertion at PP, MP and DP	Antagonist tendons
Shirafuji S. et. al., 2014[27]	Extensor tendon at DP. PIP-DIP coupling with pulley system	None	Flexor insertion at DP	None
Dong Y. and Zhang W., 2019[28]	Restoration spring	None	Insertion at PIP and DIP joints	None
Kontoudis G.P. et. al., 2019[11]	Restoration spring	None	Two insertions at DIP joint	Active abduction with passive restoration spring
Yanagisawa K. et. al., 2016[29]	Extensor tendons at MP and DP	None	Flexor insertion at DP	None
He Z. et. al., 2020[19]	Imitating EA structure	Rubber sheet as volar plate	FDP and FDS	None
Zhang Z. et. al., 2019[30]	Restoration spring	Mechanical block in extension	FDP and FDS	Antagonist tendons
Mifsud N. et. al., 2006[23]	Restoration spring	None	flexor insertion at DP over pulley system	DC motor
Rothling, F. et. al. 2007[31]	Extensor tendons at PP,MP and DP	Mechanical block in extension	flexor insertion at PP, MP and DP	Antagonist tendons
Grebenstein, M. et. al., 2010[32]	Extensor tendons at PP,MP and DP	Mechanical block in extension	Flexor insertion at PP,MP and DP	Antagonist tendons
Wilkinson, D. et. al., 2003[20]	Imitating EA structure	None	Passive spings at MP and DP	Antagonist tendons
Deshpande, A. et. al., 2011[21]	Imitating EA structure	None	Flexor insertion at MP and DP	Antagonist tendons
Lotti, F. et. al., 2005[33]	restoration spring	None	Flexor insertion at PP, MP and DP	None
Dalley, S. et. al., 2009[34]	restoration spring	Mechanical block in extension	Flexor insertion at PP, MP and DP	None
Xu and Todorov, 2016[14]	Imitating EA structure	Crocheted volar plate	Flexor insertion at MP and DP	None
Folgheraiter and Gini, 2000[12]	Extensor tendon at PP and DP	None	Flexor inserion at MCP and DIP	Antagonist tendons
Kurita, Y. et. al., 2011[35]	Extensor tendons at PP and MP. PIP-DIP coupling with pulley	None	flexor insertion at MCP and PIP	Antagonist tendons
Oung, S. et. al, 2012[36]	Extensor tendon at DIP	Mechanical block in extension	Flexor insertion at MCP, PIP and DIP	Antagonist tendons
Rodic, A et. al., 2014[37]	Extensor tendon at MCP and DIP	None	Flexor tendon at MCP and DIP	Antagonist tendons
Gong, D et. al., 2020[38]	Extensor at MCP, PIP and DIP	None	Flexor at MCP, PIP and DIP	None
Faudzi, A. A. M. et. al., 2017[16]	Imitating EA structure	Silicon rubber volar plate	Flexor at PIP and DIP	Antagonist tendons
Tasi, B.J. et. al., 2019[17]	Imitating EA structure	Silicon rubber volar plate	Flexor at PIP and DIP	Antagonist tendons
Che and Zhang, 2010[39]	Extensor tendon at PP. Restoration spring at MP and DP	Mechanical block in extension	Flexor at PIP and DIP	None

Table 2: Actuation properties of the fingers found in the literature